



Optimization of the Propeller-Driven Propulsion System for a Small UAV

Nuno de Sousa Mendes Moita

Thesis to obtain the Master of Science Degree in
Aerospace Engineering

Supervisor: Prof. André Calado Marta

Examination Committee

Chairperson: Prof. Fernando José Parracho Lau

Supervisor: Prof. André Calado Marta

Member of the Committee: Prof. Pedro da Graça Tavares Álvares Serrão

April 2018

Dedicated to my family for believing in me.

Acknowledgments

I would like to thank to my supervisor André Calado Marta for his patience and guidance along this Master Thesis. It was a privilege to be guided by someone with so much experience in this field.

To my hometown friends, João Gonçalves, João Tavares and Rui Ramos, for their support and being always available and present during the best and the worst moments of these last five years. Without you, I am sure that all of this would not be possible.

To my Técnico colleagues and friends, specially to Fábio Garcia, for all the support and motivation during the last five years. Also to my friends from the tennis table club, for their support and motivation.

To my friend Maria Monteiro, for her support, motivation, proud and being always available during the best and the worse moments during the last year. Without you, I am sure all of this would not be possible.

To my maternal grandparents, for their love, support and motivation since always. Without you, everything would have double the difficulty.

To my father, for all his continuous support, love and patience over all the years. For considering all my necessities as his priority, even in the hardest times. To my mother, for her love, concern and for always encouraging me to be better and to fight for my objectives. To my sister, for all the support, motivation and proud. Without you, I would never reach the place where I am today.

Resumo

Com o crescimento do desenvolvimento de UAVs desde o fim da 2^a Guerra Mundial, atualmente, existem UAVs com as mais diversas funcionalidades e missões.

Integrando no projeto do LEEUAV, um UAV desenvolvido pelo IDMEC, em conjunto com o AergoG e o INEGI, o objetivo desta dissertação é otimizar o hélice do sistema de propulsão já anteriormente construído. Após uma revisão da literatura e de pesquisa sobre os diferentes *softwares* existentes para análises de sistemas de propulsão, foi escolhido o *software* QPROP para realizar as análises. Após a escolha do *software*, foi realizada uma parametrização do hélice, incluindo parâmetros que caracterizam a geometria exterior do hélice, tais como o diâmetro e a distribuição da corda e do ângulo de torção em cada uma das pás do hélice e parâmetros que caracterizam o perfil usado em cada uma das pás do hélice, nomeadamente a variação do coeficiente de sustentação com o ângulo de ataque, os coeficientes de sustentação máximo, mínimo e para um ângulo de ataque nulo do perfil, o coeficiente de resistência aerodinâmica resultante da forma do perfil e o correspondente coeficiente de sustentação e o número de Reynolds usado como referência, assim como o expoente que é usado para ajustar a curva para diferentes valores do número de Reynolds. Após execução do *software* QPROP, foram considerados os parâmetros usados para avaliar o desempenho do hélice tais como a força propulsiva, os coeficientes de potência e de força propulsiva, e a eficiência do hélice.

Para realizar os ensaios experimentais, foram escolhidos três hélices diferentes, onde foi possível analisar como varia a sua performance para diferentes diâmetros, passos e motores e validar o *software*. Tendo em conta que não se sabia ao certo que perfil estava a ser usado em cada hélice, foram considerados dois possíveis perfis, cujos dados foram determinados com o *software* XFOIL. Os parâmetros geométricos do hélice foram determinados manualmente.

Após a realização dos ensaios experimentais e validação do *software* QPROP, foi realizada uma otimização progressiva usando o *software* MATLAB[®], tanto para a fase de vôo cruzeiro como para a fase de subida. Inicialmente apenas a rotação do motor foi considerada como parâmetro na otimização e apenas mais tarde foi otimizada a geometria. Com esta otimização foi obtido um sistema motor+hélice com uma eficiência superior ao inicial para as duas fases de vôo, tal como era desejado.

Palavras-chave: Hélice, Otimização , Eficiência, Força Propulsiva, Potência Elétrica

Abstract

Since the end of the 2nd World War, there has been a growth of the development of UAVs and, nowadays, there are UAVs aimed to a variety of functionalities and missions.

Integrated in the LEEUAV project, an UAV developed by IDMEC, together with AeroG and INEGI, the objective of this dissertation is to optimize the propeller-driven propulsion system designed and built previously. After some literature review and research about the different existing softwares for propulsion systems analysis, the chosen software was the QPROP. After software selection, a propeller parametrization was made, including the parameters that characterize the planform shape of the propeller, such as the diameter and the chord and the pitch angle distributions of each blade and the characteristics of the airfoil used in each blade, namely the derivative of the lift coefficient with the angle of attack, the lift coefficient at zero angle of attack, the maximum and the minimum lift coefficient, the profile drag coefficient and its corresponding lift coefficient, the Reynolds number used as a reference and the exponent used to adjust the polar curve to different Reynold numbers. After running QPROP, some functions were used to evaluate the performance of the propeller, such as the thrust, the power and thrust coefficient and the propeller efficiency.

To perform the experimental tests, three different propellers were chosen to study how the performance varies for different diameters, pitches and motors and to validate the software. Since it was not known accurately which airfoil was used in each propeller, two different airfoils, whose data was obtained using the software XFOIL, were considered. The geometric parameters of the propeller were measured manually.

Following the experimental tests and the validation of the software QPROP, a progressive optimization using the software MATLAB[®], for cruise and climb, was performed. Initially, only the motor rotation speed was considered in the optimization and only later the geometry optimization was performed. At the end of this optimization, a system motor+propeller with an higher efficiency for both flight conditions was obtained, as desired.

Keywords: Propeller, Optimization, Efficiency, Thrust, Electrical Power

Contents

Acknowledgments	v
Resumo	vii
Abstract	ix
List of Tables	xv
List of Figures	xvii
Nomenclature	xxi
Glossary	xxv
1 Introduction	1
1.1 Motivation	1
1.2 Larger Project Overview	1
1.3 Objectives	3
1.4 Thesis Outline	4
2 Analytical Propeller Analysis	7
2.1 Theoretical Models	7
2.1.1 Blade Element Theory	9
2.1.2 Blade Element Momentum Theory	11
2.2 Propeller Parametrization	13
3 Numerical Propeller Analysis	17
3.1 Software Description	17
3.1.1 AKPD/AKPA	17
3.1.2 Javaprop	18
3.1.3 QProp	21
3.2 Software Implementation	23
4 Experimental Facility	25
4.1 Electric Motors	25
4.2 Propellers	26
4.2.1 Description of Tested Propellers	26
4.2.2 Manual Geometry Measurement	27

4.2.3	3D Laser Scanning Geometry Measurement	28
4.2.4	Airfoil Drag Polar	30
4.3	Wind Tunnel	31
4.4	Force Balance	32
4.4.1	Structure	33
4.4.2	Sensors	35
4.4.3	Calibration	37
5	Initial Propeller Analysis	41
5.1	Wind-Tunnel Tests	41
5.2	LEEUAV Case Study	45
5.3	Verification and Validation	50
5.3.1	Analysis Framework	50
5.3.2	Validation Procedure	50
6	Propeller Optimization	57
6.1	Problem Definition	57
6.1.1	Objective function and Design Variables	57
6.1.2	Constraints and Bounds	58
6.1.3	Methods Overview and Selection	59
6.1.4	Multi-objective optimization	60
6.2	Process Description	61
6.3	Operating Conditions Optimization	62
6.4	Propeller Geometry Optimization	64
6.5	3D Optimal Design	68
7	Conclusions	71
7.1	Achievements	72
7.2	Future Work	73
Bibliography		75
A Input Files and Results		79
A.1	Propeller Files	79
A.2	Experimental Results	81
A.2.1	Thrust	81
A.2.2	Electrical Power	82
A.2.3	Thrust Coefficient	83
A.2.4	Power Coefficient	84
A.2.5	Efficiency	85
A.3	LEEUAV Case Study	86

A.3.1 Propeller Pitch	86
A.3.2 Electrical Motor	86
A.3.3 Input Voltage	87
A.4 Validation	88
A.5 Validated System Files	91
A.6 Optimization Files	92

List of Tables

1.1	First generation propulsive characteristics [2]	3
3.1	Comparison between JavaProp and QPROP analysis	23
4.1	Characteristics of the electric motors	26
4.2	Determination of Reynolds number	30
4.3	Description of the components of the system propeller+motor	34
5.1	Systems used in the variation of the efficiency distribution for each parameter	47
5.2	Comparison between the errors of thrust for the different airfoils for the APC 13"×8"	51
5.3	Comparison between the errors of electrical power for the different motor internal resistances for the OS-3810-1050	53
5.4	Comparison between the errors of thrust for the different airfoils for an APC 16"×8"	53
5.5	Comparison between the errors of electrical power for the different resistances for the OS-5020-490	54
5.6	Comparison between the errors of thrust for the different airfoils for an APC 16"×10"	54
5.7	Comparison between the errors of electrical power for the different motor internal resistances	55
5.8	Final comparison between the errors of electrical power for the different propellers for the OS-5020-490	55
5.9	Summary table with the validated characteristics for each propeller	55
5.10	Summary table with the validated internal resistance for each motor	55
6.1	Results of the bounded constrained optimization	63
6.2	Results of the thrust constrained optimization	63
6.3	Results of the initial propeller geometry optimization	66
6.4	Results of the final propeller geometry optimization	68
6.5	Comparison of the results obtained for the initial and the final propeller	69

List of Figures

1.1	Mission profile of the LEEUAV	2
1.2	LEEUAV design	2
1.3	Data obtained for a 15" × 8" APC propeller [2]	3
2.1	Superimposed horseshoes along the lifting line	7
2.2	Vortex lattice theory on a finite wing	8
2.3	Panel method	9
2.4	Blade element theory scheme	9
2.5	Airfoil cross-section geometric properties	10
2.6	Decomposition of lift and drag into thrust and torque	10
2.7	Velocity decomposition and angle definitions	12
2.8	Parametrization of a propeller	14
2.9	Variation of thrust and power coefficients with the aspect ratio [11]	16
3.1	Types of propellers analysed by the software	17
3.2	Design card of JavaProp	19
3.3	Airfoils card of JavaProp	19
3.4	Multi-analysis card of JavaProp	20
3.5	Single-analysis card of JavaProp	20
3.6	Example of a type 1 motor file	21
3.7	Example of a type 2 motor file	21
3.8	Example of a propeller file	22
4.1	Spinner	26
4.2	Calliper used to make the blade measurements	27
4.3	Blade divided in sections	28
4.4	Scheme of the measurement procedure of the blade	28
4.5	3D scanning measurement of the blade	29
4.6	3D CAD model of a measured blade	29
4.7	Polars from the different possible airfoils in use	31
4.8	Relation between flow velocity and frequency	32
4.9	Diagram with the several stages of construction of the balance	33

4.10 Final structure assembly	33
4.11 Support of the system motor+propeller	34
4.12 Resized support of the system motor+propeller	35
4.13 Data acquisition hardware	36
4.14 Labview [®] interface	36
4.15 System used on the load cell calibration	37
4.16 Linear regressions used to calibrate the load cell sensors	38
4.17 Multimeter used to perform the voltage sensor calibrations	38
4.18 Linear regressions used to calibrate the voltage sensor	39
4.19 Current clamp used to perform the current sensor calibration	39
4.20 Linear regression used on current sensor calibration	40
4.21 Linear regression used in the calibration of the airspeed sensor	40
5.1 Variation of thrust with airspeed and RPM for the system OS-3810-1050 + APC 13"×8" for 12.5 V	42
5.2 Variation of electrical power with airspeed and RPM for the system OS-3810-1050 + APC 13"×8" for 12.5 V	43
5.3 Variation of thrust coefficient with airspeed and RPM for the system OS-3810-1050 + APC 13"×8" for 12.5 V	44
5.4 Variation of power coefficient with airspeed and RPM for the system OS-3810-1050 + APC 13"×8" for 12.5 V	44
5.5 Variation of efficiency with airspeed and RPM for the system OS-3810-1050 + APC 13"×8" for 12.5 V	45
5.6 Drag vs airspeed for LEEUAV with and without photovoltaic panels [3]	46
5.7 Variation of propulsion efficiency with propeller diameter	47
5.8 Comparison of the variation of efficiency with airspeed for all systems	48
5.9 Variation of thrust coefficient with advance ratio	49
5.10 Variation of power coefficient with advance ratio	49
5.11 Analysis framework used to make the simulations	50
5.12 Residual variation with β_{add} for an APC 13"×8"	51
5.13 Thrust variation with RPM obtained for each airfoil for the APC 13"×8"	52
5.14 Residual variation with motor internal resistance for an OS-3810-1050	52
5.15 Electrical power variation with RPM obtained for different motor internal resistances for the OS-3810-1050	53
6.1 Overview of different types of optimization methods	59
6.2 Multi-objective optimization pareto front distribution	60
6.3 Optimization process scheme	62
6.4 Illustration of cubic spline method	64

6.5 Geometric pitch angle and chord distributions of the propellers blades designed for cruise and climb conditions, before and after an optimization process	66
6.6 Geometric pitch angle and chord distributions of the final propellers' blades before and after the optimization	67
6.7 Comparison of the three-dimensional models, for rotated views, of the blade of the initial and final optimized propeller	69
6.8 Rotated views of the physical three-dimensional model	70
 A.1 Input files for APC 13"×8" propellers	79
A.2 Input files for APC 16"×8" propellers	80
A.3 Input files for APC 16"×10" propellers	80
A.4 Variation of thrust with airspeed and RPM for the different systems tested	81
A.5 Variation of electrical power with airspeed and RPM for the different systems tested	82
A.6 Variation of thrust coefficient with airspeed and RPM for the different systems tested	83
A.7 Variation of power coefficient with airspeed and RPM for the different systems tested	84
A.8 Variation of efficiency with airspeed and RPM for the different systems tested	85
A.9 Efficiency variation with propeller pitch	86
A.10 Efficiency variation with electrical motor	87
A.11 Efficiency variation with input voltage	88
A.12 Validation parameters for the system OS-5020-490 + 16"×8"	89
A.13 Validation parameters for the system OS-5020-490 + 16"×10"	90
A.14 Validated files for the system OS-3810-1050 + 13"×8"	91
A.15 Validated files for the system OS-5020-490 + 16"×8"	91
A.16 Validated files for the system OS-5020-490 + 16"×10"	92
A.17 First derivative variation in order to the respective design variables for different values of different step size	93
A.18 Parameters evolution along the operation variables unconstrained optimization process, at each iteration	94
A.19 Parameters evolution along the operation variables optimization process with constrained thrust, at each iteration	95
A.20 Parameters evolution along the geometric variables optimization process with constrained thrust and electrical power, at each iteration	96
A.21 Parameters evolution along the final geometric variables optimization process, at each iteration	97

Nomenclature

Greek symbols

α	Angle of attack.
α_0	Original angle of attack.
β	Geometric pitch angle.
ϵ	Weight used in multi-objective optimization.
η	Propeller efficiency.
μ	Molecular viscosity coefficient.
Ω	Angular velocity of the propeller.
ψ	Flow angle.
ψ_0	Original flow angle.
ρ	Air density.
σ	Blade solidity.
θ	Induced angle.

Roman symbols

A	Linear inequality constraints matrix .
a	Speed of sound.
A_{eq}	Linear equality constraints matrix .
\vec{b}_{eq}	Linear equality constraints vector.
\vec{b}	Linear inequality constraints vector.
B	Number of blades.
C	Nonlinear inequality constraints matrix.
c	Propeller chord.

C_d	Airfoil drag coefficient.
C_l	Airfoil lift coefficient.
C_{d_0}	Airfoil profile drag coefficient.
C_{d_2}	Airfoil drag coefficient slope.
C_{eq}	Nonlinear equality constraints matrix .
C_{l_0}	Airfoil lift coefficient at zero angle of attack.
$C_{l_{\alpha_0}}$	Airfoil original lift coefficient derivative with the angle of attack.
C_{l_α}	Airfoil lift coefficient derivative with the angle of attack.
$C_{l_{C_{d_0}}}$	Airfoil lift coefficient corresponding to the profile drag coefficient.
C_{P_1}	Power coefficient calculated by QPROP.
C_P	Power coefficient.
C_Q	Torque coefficient.
C_{T_1}	Thrust coefficient calculated by QPROP.
C_T	Thrust coefficient.
D	Drag; Propeller diameter.
E	Energy.
f	Frequency.
F, G	Objective functions.
h_1	Upper Bound.
h_2	Lower Bound.
I	Current.
I_0	Zero-load current.
J	Advance ratio.
K_v	Motor constant.
\vec{lb}	Lower bound vector.
L	Lift.
M	Mach number.
m	Aircraft mass.

N	Motor rotation velocity in revolutions per second.
P	Electrical power.
p	Pitch.
P^*	Pressure.
P_{shaft}	Mechanical power.
Q	Torque.
R	Motor electrical resistance; Propeller radius.
r	Longitudinal distance between the hub and a given position on a propeller.
Re	Reynolds number.
S	Surface area.
T	Thrust.
U	Velocity.
\vec{ub}	Upper bound vector.
u	External induced velocity.
v	Induced velocity resulting from lift generation.
V^*	Voltage.
W	Aircraft weight.
\vec{x}_0	Initial guess vector.
\vec{x}	Optimization components vector.
x	Nondimensional blade distance.
y_{exp}	Experimental value.
y_{num}	Numerical value.

Subscripts

\vec{x}^*, \vec{y}^*	Position Cartesian components of the airfoils for the optimized propeller.
\vec{x}, \vec{y}	Position Cartesian components of the airfoils before optimization.
a	Axial.
add	Added offset.
$climb$	Climb condition.

cruise Cruise condition.

dyn Dynamic reference.

expo Exponent.

j, k Index.

max Maximum.

min Minimum.

ref Reference condition.

static Static condition.

t Tangential.

tip Tip.

total Total.

val Validated condition.

Glossary

AHP	Analytical Hierarchy Process.
APC	Advanced Precision Composites.
AeroG	Aeronautics and Astronautics Research Center.
BEMT	Blade Element Momentum Theory.
BET	Blade Element Theory.
CAD	Computer-Aided Design.
DAQ	Data Acquisition System.
DC	Direct Current.
ESC	Electronic Speed Controller.
FEUP	Faculdade de Engenharia da Universidade do Porto.
IDMEC	Institute of Mechanical Engineering at Instituto Superior Técnico.
INEGI	Instituto de Ciência e Inovação em Engenharia Mecânica e Engenharia Industrial.
ISA	International Standard Atmosphere.
IST	Instituto Superior Técnico.
LAETA	Associated Laboratory for Energy, Transports and Aeronautics.
LEEUAV	Long Endurance Electrical Unmanned Aerial Vehicle.
MTOW	Maximum Take-Off Weight.
PLA	Polylactic Acid.
PWM	Pulse Width Modulation.
RPM	Rotations per Minute.
RPV	Remote-Person View.
SI	International System.
SMTU	State Marine Technical University.
SQP	Sequential Quadratic Programming.

UAV	Unmanned Aerial Vehicle.
UBI	Universidade da Beira Interior.

Chapter 1

Introduction

1.1 Motivation

An Unmanned Aerial Vehicle (UAV) is a type of aircraft which can be controlled from an external source or autonomously by inboard computers, so it has no crew neither passengers.

Since the second half of the 19th century, the human race saw a big potential in UAVs development. Given that the first entity to invest in the development of these aircrafts was the U.S. Army, at the beginning, UAVs were only used for military purposes, such as vigilance and reconnaissance missions. The use of UAVs for civil applications took a longer period of time, due to the high costs and the complexity of civil missions. However, nowadays, the UAVs are used for missions like delivering mail in inaccessible regions, forest fires detection and recognition operations.

One of the most important systems of a UAV is the propulsion system, which corresponds to nearly 90% of the total energy consumed by the vehicle [1]. At the beginning of UAVs development, fossil fuels were used. However, in the last years, there has been an increase in the demand of electrical motors for reducing emissions, noise and the dependence of non-renewable energy sources.

In this master thesis, the main field of study was the characterization of a system motor + propeller and its optimization to get a better performance for the UAV, by providing higher thrust using less power.

1.2 Larger Project Overview

The propeller designed in this thesis will be implemented in the Long Endurance Electrical Unmanned Aerial Vehicle (LEEUAV) project. This project was developed by AeroG at UBI, IDMEC at IST and INEGI at FEUP. All units involved are a part of LAETA.

The main goal of this project was to develop a cheap and ecological electric UAV, without any carbon dioxide emissions. The aircraft must have the capability to take-off in short airfields, to have an easy construction and maintenance and to be highly flexible to perform several kinds of surveillance missions. The specific mission requirements are:

- Climb 1000 *m* in 10 minutes, which corresponds to a climb rate of 1.67 *m/s*. According to [2], at

1300 m of altitude, it is possible for a Remote-Person View (RPV) camera to record ground footage with an acceptable resolution display;

- Fly for 8 hours in the equinox and reach a range of 200 km , so its velocity must be nearly 7 m/s . To provide a margin in the projected, it was considered a cruise velocity of 7.53 m/s ;
- The aircraft size must be adequate to operations in small airfields and the take-off must be able to be done by hand-launching or using a ground support system;
- The maximum bank angle is 45° , which corresponds to a load factor of 1.414;

The mission profile for this UAV is the typical mission profile for basic operations. It consists of a take-off and climb stage followed by cruise and at the final, it has a descending and landing stage with a possible loiter in the middle of descent, as illustrated in figure 1.1:



Figure 1.1: Mission profile of the LEEUAV [2]

Initially, it was discussed the idea of installing several motors with propellers along the wing. This idea could provide an extra bending relief and reduce the drag of the fuselage, however, due to a possible existence of some engine-out problems that could lead to an increased size of the empennage, it was concluded that for a maximum payload of 10 N , it should be installed only one electrical motor.

After some tests and simulations, an Analytical Hierarchy Process (AHP) model was built and it was concluded that, as a first model, the best UAV configuration would be a pusher propeller on the V-Tail [2]. The UAV designed in this project can be visualized in figure 1.2a).

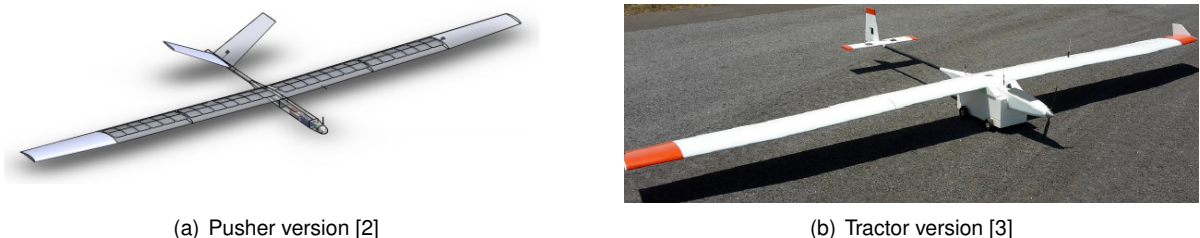


Figure 1.2: LEEUAV design

However, in later versions, it was decided to install a tractor propeller, as seen in figure 1.2b), as the one that was tested in this dissertation.

Taking in account the different flight stages, some studies were done to measure how thrust and power vary along the flight for the UAV fulfil all necessary requirements previously described. In [2], a propeller 15"×8" was used with a motor Hyperion ZS 3025-10. The main characteristics of this system are described in table 1.1.

Motor	Motor characteristics			Propeller	Battery
	K_v [RPM/V]	I_{max} [A]	P_{max} [W]		
Hyperion ZS 3025-10	775	65	1150	0.1976	15" × 8" Lipo 3S 11.1V

Table 1.1: First generation propulsive characteristics [2]

In terms of thrust and power, the climb stage is the most critical. Since the airspeed at this stage reaches 7.67 m/s, it was necessary to calculate how much power was consumed to verify if the system in use was appropriate. After some tests, it was calculated a minimum power of 405W. Knowing that the maximum power that the motor is able to provide during this stage of flight is 721.5W, this system could fulfil this requirement. Knowing the motor maximum efficiency and power, it was possible to obtain the graphics in figure 1.3.

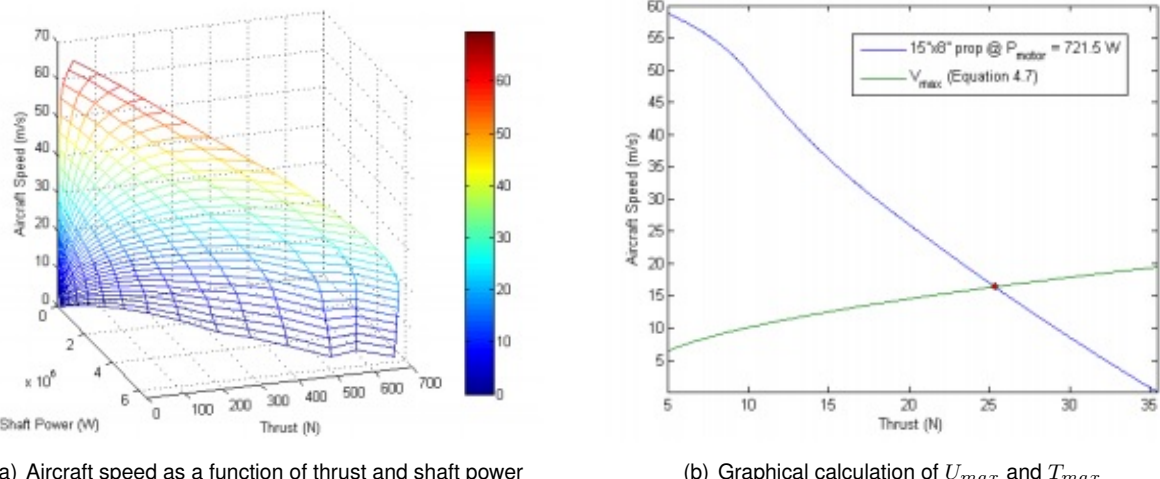


Figure 1.3: Data obtained for a 15" × 8" APC propeller [2]

In figure 1.3b), it is possible to obtain the maximum thrust and the maximum velocity produced by the system motor+propeller considered on [2]. It is also possible to conclude that $(\frac{T}{W})_{max} = 0.43$ for a maximum velocity of 16.39 m/s.

1.3 Objectives

The main objective of this master thesis is to improve the propulsion system for the LEEUAV, a UAV that has already been built, by designing a propeller with an optimized planform shape. With this optimization it is expected an improvement on the performance of the propeller during the different flight stages, mainly at cruise and climb.

The first objective to achieve is to define a software that performs numerical simulations that allows to obtain the performance data of a given system motor+propeller. After defining the software, it is intended to perform a parametrization of the propeller to define the inputs and the outputs of this software.

Secondly, it is intended to rebuild the support that handles the system motor+propeller and to calibrate the sensors to obtain the best possible accuracy in the experimental results.

After reaching the previous objective, wind tunnel tests must be performed to predict the performance of different systems motor+propeller by varying the parameters that define the planform shape of the propeller, to determine which would be the best system to apply in the LEEUAV, before any optimization and to perform a validation of the numerical software by comparing the numerical and the experimental results for each system to guarantee the highest possible accuracy of the numerical software.

The last objective is to build an optimization tool that uses the validated numerical software and determines the optimized planform shape parameters and operating conditions. At the end, it is intended to manufacture the optimized propeller obtained by using the optimization tool.

1.4 Thesis Outline

In chapter 2, initially, the several theoretical methods used in the propeller analysis are described, such as the Disk-Actuator Theory, the Lifting Line Theory for unidimensional analysis, the Vortex Lattice Theory for bidimensional analysis and the Panel Method for tridimensional analysis. The Blade Element Theory and the Blade Element Momentum Theory are also described. At the end, the parametrization of the propeller is presented, where all the input and output parameters expected from an analysis are presented and described.

In chapter 3, initially, the three existing possible softwares to analyse a propeller are presented: the AKPD/AKPA, the Javaprop and the QPROP. At the end of the chapter, it is chosen the software to use and the reasons of its implementation.

In chapter 4, initially, there are some items that are briefly described, such as the main characteristics of the electrical motors; the tested propellers and their acquisition data methods, such as the use of the software XFOIL to obtain the airfoil characteristics, the manually measuring of the planform shape parameters and the 3D scanning method; the wind tunnel; the structure, where the changes made on the motor support system were also described, since this one was overdimensioned for the actual case study; the sensors of the force balance used to perform the experimental tests and the processes of calibration of each sensor to assure the accuracy of the results obtained.

In chapter 5, the execution of the experimental tests for each system motor+propeller is described. At this stage, it is possible to analyse the performance of each system with the variation of the diameter, the pitch, the motor and the input voltage. At this phase, some dynamic and static tests are performed, just by varying the thrust level and the wind tunnel velocity. It is also possible to analyse the way the data obtained can be applied to LEEUAV. Finally, the validation of the software QPROP is presented by comparing the experimental results with the numerical results of the thrust and the electrical power for each airfoil. With the validation, it is possible to determine which airfoil is being used in each propeller

and to fit the best possible the curves thrust *vs* RPM and electrical power *vs* RPM for each propeller.

In chapter 6, initially, the existing methods to solve the optimization problems and the entire formulation of the optimization are described. Then, a progressive optimization is made, using the software MATLAB[®] where at the beginning, the efficiency optimization is performed for cruise and climb conditions and is only analysed for the variation of the RPM and only later the geometry variation is taken in account. At the end, a 3D model of the final propeller is modelled using the software SOLIDWORKS[®] and the new optimised propeller is manufactured using a 3D-Printer.

In chapter 7, the conclusions of this dissertation and the future work that must be done to fulfil this master thesis are presented.

Chapter 2

Analytical Propeller Analysis

In this chapter, initially, the different theoretical methods used in the propeller analysis will be described. At the end, it is going to be made a parametrization of the propeller.

2.1 Theoretical Models

The Disk-Actuator Theory, also known as Integral Momentum Theory, was first introduced by Rankine on 1865 and then developed by Froude on 1885. According to this theory, a physical propeller is replaced for a permeable disk with a given area and a vanishing thickness. By using the Bernoulli equation and a Balance Equilibrium of Forces, all the parameters are determined. To validate this theory, it is necessary to take in account some criteria which can be found in [4, 5].

The Lifting Line theory was developed by Prandtl during the World War I and it is so reliable that it is still used nowadays for preliminary calculations. According with this theory, a vortex filament, bounded to a fixed location experiences a lift force, that makes a contrast with a free vortex which moves with the fluid, along the flow. Due to Helmotz theorem, it is assumed that the vortex is split in two free vortices and continues downstream from the wings to the infinity. To this set of vortices, it is called an horseshoe. This horseshoe produces an induced velocity along the bound vortex, which creates a downwash effect, however, a single horseshoe does not really simulate its true behaviour. To solve this problem, it was decided to represent a wing by a large number of horseshoes, whose all bounded vortex are coincident on a single line, the Lifting Line. This can be regarded in figure 2.1.

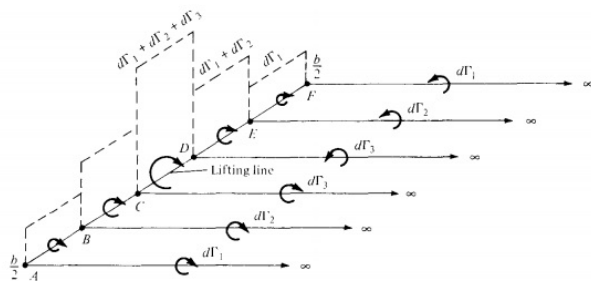


Figure 2.1: Superimposed horseshoes along the lifting line [6]

Based on figure 2.1, it is possible to calculate the induced velocities along the Lifting Line and the to determine the Lift and Drag distributions [6].

However, this theory only works well for high aspect ratios. For low aspect ratios, a model where a single lifting line is replaced by a series of lifting lines must be used. According with this model, two different vortex sheets are obtained, one constituted by the lifting lines that cover the wing plan and another constituted by the wake vortices, forming a lifting surface. The interaction between these two vortex sheets induces a normal component of an induced velocity. The equation of the induced velocity is defined for an arbitrary point and is shown in [6]. The main problem of this method is to solve this equation and to respect the conditions imposed at [6]. To solve this problem, several horseshoe vortices with different strengths are superimposed. This approximation is called the Vortex Lattice theory and is represented in figure 2.2.

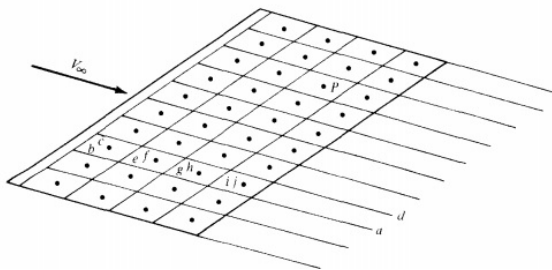


Figure 2.2: Vortex lattice theory on a finite wing [6]

As it is presented in figure 2.2, the entire wing is covered by a lattice of horseshoe vortices, each one with a different unknown strength. Using the criteria presented in [6], a system of algebraic equations can be built and solved for the presented unknowns.

To perform three-dimensional analysis, the Panel Method is used. This method is based in a perturbation in the potential formulation, where the wake surface is included and can be considered as an infinitely thin domain. To simulate the thickness effect, source elements are used and to simulate the lift effect, antisymmetric terms such as doublet are often used. To formulate the three-dimensional problems, Neumann and Dirichelet boundary conditions are applied, but specifying them does not yield an unique solution, as it is explained in [7]. In some cases, it might be showed that the problem can be totally defined by selecting a source distribution. However, this is just valid when there is no lift associated to the flow. For the three-dimensional lifting problem, it is necessary to model a wake, since the bound vorticity needs to be continued beyond the wing. At this point it is assumed that the problem is unique and it was selected a combination of source/doublet distributions with a wake model and the Kutta condition. The surface of the body, as shown on figure 2.3, is divided into a given number of surface panels and additional wake panels.

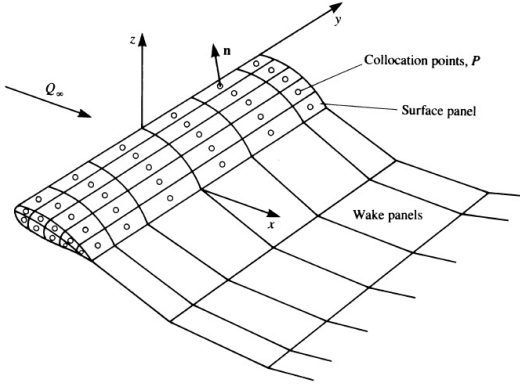


Figure 2.3: Panel method [7]

By applying all the boundary conditions at each panel, a set of algebraic equations, where the unknowns are the source and doublet distributions, is obtained and solved, as explained in [7].

The most common models that are usually used are the Blade Element Theory (BET) and the Blade Element Momentum Theory (BEMT), so, a more detailed description of these theories is shown in the following sections.

2.1.1 Blade Element Theory

The Blade Element Theory (BET) is a simple and fast method based on the total area and geometry of a propeller, so it is possible to predict the propeller dimensions to develop the desired performance.

This theory was proposed by Drzweick in 1982 [8] to study the propeller of an aircraft and it consists in splitting each blade in independent sections which are analysed based on the local velocities. At each section, a bidimensional force balance is applied to obtain lift, drag, thrust and torque distributions. A final integration over the entire blades gives the performance characteristics of the propeller. In figure 2.4, it is possible to visualize a scheme of the model applied in a blade.

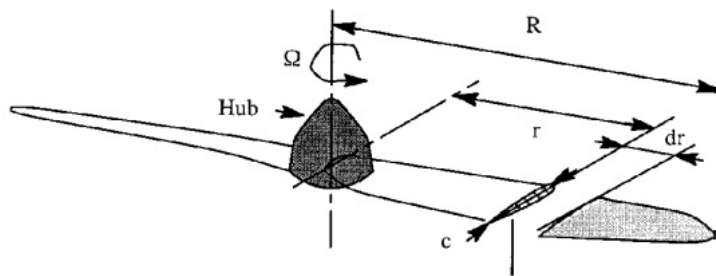


Figure 2.4: Blade element theory scheme [8]

The flow is analysed independently on each section assuming there are only axial and angular velocities and there is no induced flow from any other sections. A scheme from a cut on a blade can be seen in figure 2.5:

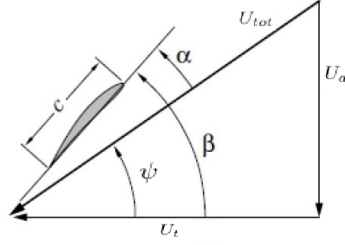


Figure 2.5: Airfoil cross-section geometric properties [9]

By analysing figure 2.5, it is verified that the cross-section experiences a resultant velocity, U_{tot} , that results from the vectorial sum of the axial velocity U_a and the tangential velocity U_t . In this theory, the axial velocity represents the flight velocity and the tangential velocity represents the velocity due to the rotation of the propeller. It is important to understand that the tangential velocity near the hub is much less than the velocity at the tip of the propeller since U_t is given by

$$U_t = \Omega r , \quad (2.1)$$

where Ω is the angular velocity of the propeller in rad/s and r corresponds to the radial distance along the blade between the hub axis and the point where the analysis is being done. The angle ψ is the resultant flow angle with respect to the plane of rotation, β is the geometric pitch angle and α is the cross-section angle of attack. In figure 2.6, a force diagram presented for each cross-section is presented.

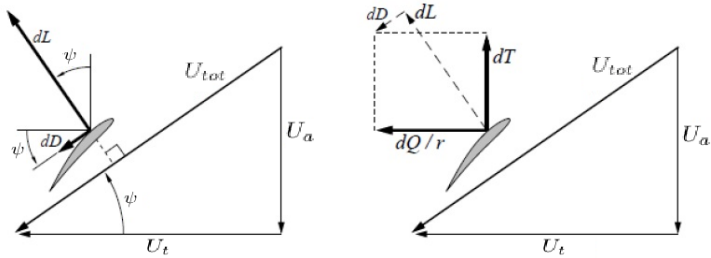


Figure 2.6: Decomposition of lift and drag into thrust and torque [9]

From figure 2.6, it is possible to verify that the lift and drag normal and axial components to the propeller can be calculated. As so, the contribution to thrust and torque for each section can also be calculated. From bidimensional aerodynamics, it is known that

$$dL = \frac{1}{2} \rho U^2 c C_l dr \quad (2.2)$$

and

$$dD = \frac{1}{2} \rho U^2 c C_d dr . \quad (2.3)$$

According to [8], since it is assumed that U_a is constant along the blade and U_t increases linearly along the blade, by analysis of figure 2.6, it is necessary to increase the geometric pitch angle β near the hub to maintain an efficient angle of attack distribution. It is also possible to verify that the local lift

coefficient C_l is not constant along the blade due to the angle of attack distribution not being constant along the blade. The distribution of $C_l(r)$ can be given by

$$C_l(r) = C_{l_\alpha} (\beta(r) - \psi(r)) , \quad (2.4)$$

where C_{l_α} is the derivative of the Lift Coefficient in order to the angle of attack. Also, by analysis of figure 2.6, it is noticed that the elemental lift and drag may be taken in account to calculate other relevant characteristics of the propeller such as the elemental thrust and torque, dT and dQ , for each section. The elemental thrust and elemental torque are calculated as:

$$dT = dL \cos \psi - dD \sin \psi = \frac{1}{2} \rho U_{tot}^2 c (C_l \cos \psi - C_d \sin \psi) dr \quad (2.5)$$

and

$$dQ = (dL \sin \psi + dD \cos \psi) r = \frac{1}{2} \rho U_{tot}^2 c r (C_l \sin \psi + C_d \cos \psi) dr . \quad (2.6)$$

After obtaining the elemental expression for each of these parameters, it is possible to obtain the total thrust and torque by integrating the previous expressions over the total propeller. As so, it is necessary to take in account the number of blades, B , and it is necessary to know all the aerodynamic characteristics of each blade section since these may change due to the linear variation of U_t along the blade. The obtained expressions are

$$T = \frac{1}{2} \rho B \int_0^R U_{tot}^2 c (C_l \cos \psi - C_d \sin \psi) dr \quad (2.7)$$

and

$$Q = \frac{1}{2} \rho \int_0^R U_{tot}^2 c (C_l \sin \psi + C_d \cos \psi) r dr . \quad (2.8)$$

So, this theory allows for the analysis of specific propellers with different geometrics shapes along the blades of a propeller, however, with the trade-off of increased complexity, it is more detailed than the one-dimensional theory. Also, some assumptions are made to simplify the flow analysis and the losses are also taken in account. These assumptions do not account for induced velocities on the blades, swirl in the slipstream, non-uniform flow, or propeller blockage.

2.1.2 Blade Element Momentum Theory

The Blade Element Momentum Theory (BEMT) corresponds to an upgrade of the BET where the induced velocities are taken in account. In figure 2.7, it is possible to visualize the velocity decomposition of the resultant velocity, U_{tot} .

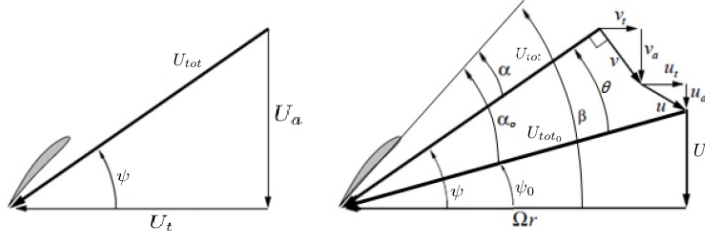


Figure 2.7: Velocity decomposition and angle definitions [9]

As it can be analysed, the axial velocity U_a results from the sum between the flight velocity U and the induced velocities u_a and v_a , while the total tangential velocity U_t results from the sum between the rotation velocity of the propeller Ωr and the induced velocities v_t and u_t . The induced velocities u and v are distinguished since v results from the lift generation by the propeller and u represents the externally-induced velocity. According to [8], to explain this theory, the u induced velocities are vanished. The velocities with the subscript "0" represent the original velocities associated with the BET.

By analysing figure 2.7 and according with Momentum theory, where $dS = 2\pi r dr$, the total-elemental thrust for a propeller with a number B of blades is given by

$$BdT = \rho(2\pi r dr)(U + v \cos \psi)(2v \cos \psi). \quad (2.9)$$

One other definition that can be used to define the total-elemental thrust for a propeller with a number B of blades is the one used for the BET theory

$$BdT = \frac{1}{2} BC_l U_{tot}^2 cdr \cos \psi. \quad (2.10)$$

By setting these two equations equal, an expression for the induced velocity v is obtained,

$$v = \frac{BC_l c U_{tot}^2}{8\pi r(U + v \cos \psi)}. \quad (2.11)$$

However, there is a case where θ , the induced angle, is assumed to be small. In this case, the equation can be re-written in terms of the induced angle,

$$\theta \approx B \left(\frac{c}{8\pi r} \right) \frac{C_{l_{\alpha_0}} (\beta - \psi_0 - \theta)}{\sin \psi_0 + \theta \cos \psi_0}. \quad (2.12)$$

Instead of solving equation (2.12) using an iterative method, two more variable are introduced: the solidity ratio, σ , and the non-dimensional blade section, x . The solidity ratio is defined by

$$\sigma = \frac{Bc}{\pi R}. \quad (2.13)$$

By adding these two variables and replacing them in equation (2.12), a new solution for θ is obtained,

$$\theta = \frac{1}{2 \cos \psi_0} \left\{ - \left(\sin \psi_0 + \frac{C_{l_{\alpha_0}} \sigma}{8x} \right) + \sqrt{\left(\sin \psi_0 + \frac{C_{l_{\alpha_0}} \sigma}{8x} \right)^2 + 4 \cos \psi_0 \frac{C_{l_{\alpha_0}} \sigma}{8x} (\beta - \psi_0)} \right\}. \quad (2.14)$$

From the equation (2.14) and taking in account the assumptions made in [8], the induced velocity is given by

$$v = U_{tip} \left\{ - \left(\frac{U}{2U_{tip}} + \frac{C_{l_{\alpha_0}} \sigma}{16} \right) + \sqrt{\left(\frac{U}{2U_{tip}} + \frac{C_{l_{\alpha_0}} \sigma}{16} \right)^2 + \frac{C_{l_{\alpha_0}} \sigma \beta x}{8} - \frac{C_{l_{\alpha_0}} \sigma U}{8U_{tip}}} \right\}, \quad (2.15)$$

where U_{tip} is the tip velocity of the blade. However, this formula is used for very high values of thrust. For lower values, one approximation that can be done is to discard the term θ^2 , yielding

$$\theta = \frac{\beta - \psi_0}{1 + \frac{8x \sin \psi_0}{C_{l_{\alpha_0}} \cdot \sigma}} \quad (2.16)$$

As so, two possible equations are presented to determine the local induced angle for the two situations previously described. It is finally possible to obtain the elemental thrust and torque expressions for each cross-section as

$$dT = B\rho \left(\frac{2\pi N r}{\cos \psi} \cos \theta \right)^2 c(C_l \cos \psi - C_d \sin \psi) dr \quad (2.17)$$

and

$$dQ = B\rho \left(\frac{2\pi N r}{\cos \psi} \cos \theta \right)^2 cr(C_l \sin \psi + C_d \cos \psi) dr. \quad (2.18)$$

Using BEMT, it is possible to obtain the additional detail of considering the induced velocities, however, it increases the complexity of the theory. The only assumption that can limit this theory is that the flow is considered to be bidimensional.

2.2 Propeller Parametrization

In this section, the main parameters that are necessary to define a propeller will be described. To define a propeller, it is necessary to define the three main categories of parameters:

- Planform shape;
- Airfoil characteristics;
- Performance.

In figure 2.8, it is possible to visualize a flowchart that represents a fully parametrization of a propeller.

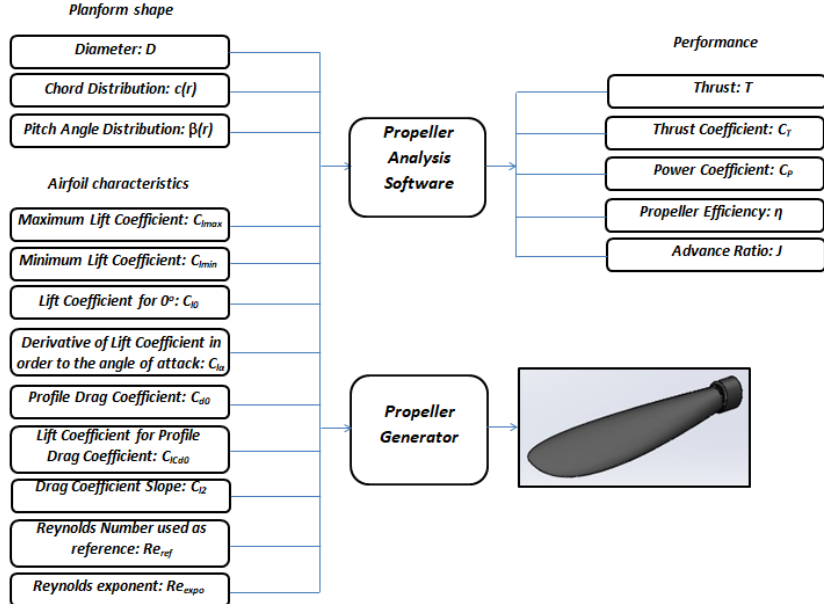


Figure 2.8: Parametrization of a propeller

Regarding the planform shape parameters presented in figure 2.8, the first parameter to take in account is the propeller diameter. It is expected that the higher this parameter is, the better will be the performance of the propeller, however, the fact of a too big radius might cause structural problems must be considered.

The second parameter to take in account is the chord distribution of the blade of the propeller. To define this paremeter, it is necessary to define the value of the chord for each section of the blade. The higher the number of sections considered, the higher the accuracy on the parametrization. Similary to the diameter, the higher the values of chord in each section, the higher the performance. Another advantage of higher chord values is a higher Reynolds number, which will also result in higher values of the thrust and power coefficients [10]. However, like said previously, some structural problems and the maximum motor electrical power can limit this parameter.

The last parameter to consider is the blade pitch angle distribution, which is directly related to the pitch of the propeller. This parameter is also desired to be high enough near the hub to provide the best performance to the propeller.

In relation to the airfoil characteristics, the parameters that are presented in the scheme of figure 2.8 are important to the software in use to determine the lift curve and the drag polar. To determine the lift curve, the four main parameters that must be considered are:

- The maximum lift coefficient $C_{l\max}$;
- The minimum lift coefficient $C_{l\min}$;
- The lift coefficient corresponding to an angle of attack of zero degrees, C_{l0} ;
- The derivative of the lift coefficient with the angle of attack, $C_{l\alpha}$.

Regarding the parameters described above, the only one that is desired to be as low as possible is

the minimum lift coefficient because the lower this parameter, the higher the range of negative angles of attack that the propeller may face without stalling. The maximum lift coefficient is desired to be as high as possible for the same reasons described before, but for positive angles of attack.

Also, the values of C_{l_0} and C_{l_α} must be as high as possible to allow the propeller to produce higher values of thrust for lower angles of attack.

To determine the drag polar, the parameters that are considered are:

- The profile drag coefficient C_{d_0} ;
- The lift coefficient corresponding to the Profile Drag Coefficient $C_{l_{C_{d_0}}}$;
- The drag coefficient slope C_{l_2} ;
- The Reynolds number from which all the previous values are obtained, Re_{ref} ;
- The Reynolds exponent that adjusts the polar for other Reynolds numbers, Re_{expo} .

As expected, the total drag coefficient must be the lowest possible, so all the parameters referred above must be the lowest possible, except the Reynolds number and the $C_{L_{C_{D_0}}}$. By reducing the drag, the resultant axial force produced by the propeller will be higher, using less power.

In relation to the performance parameters presented in figure 2.8, the first that is necessary to take in account is thrust T . This is the resultant axial force responsible for the motion of an aircraft where the propeller might be installed. This is a very important parameter to take in account since it has to present minimum values to assure that the aircraft is able to perform the several stages of flight.

The second performance parameter that must be considered is thrust coefficient, C_T . This is a dimensionless parameter which relates the Thrust produced by a propeller with its diameter and rotation velocity,

$$C_T = \frac{T}{\rho N^2 D^4} . \quad (2.19)$$

Another performance parameter that must be taken in account is Power Coefficient, C_P . This is a dimensionless parameter which is relates the mechanical power produced by a propeller with its diameter and rotation velocity, as

$$C_P = \frac{P_{shaft}}{\rho N^3 D^5} . \quad (2.20)$$

Yet, another parameter that is important is the propeller efficiency η . Since the propeller was pretended to be optimized to reduce the electrical power of the system motor+propeller, this parameter was defined as the ratio between the power that a propeller can use and the electrical power P supplied to the system,

$$\eta = \frac{TU}{P} . \quad (2.21)$$

where P is given by:

$$P = V^* I . \quad (2.22)$$

where V^* is the input voltage of the motor and and I is the current consumed by the motor.

Usually, to analyse the variation of the thrust and the power coefficients or the efficiency, a parameter called advance ratio, J , is used. This is also a dimensionless parameter, that relates the velocity with the rotation velocity and the diameter of a propeller,

$$J = \frac{U}{ND} . \quad (2.23)$$

The existence of this parameter proves that for a given ratio between these three variables and a constant pitch angle distribution, there is only one value for the four performance parameters described above. In figure 2.9, it is possible to visualize two plots with the variation of the thrust and power coefficients with the advance ratio for a typical propeller.

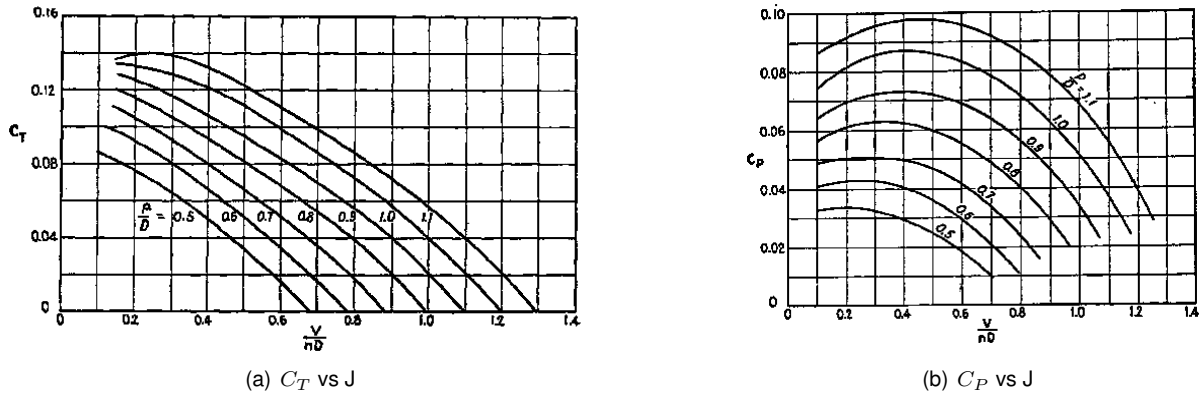


Figure 2.9: Variation of thrust and power coefficients with the aspect ratio [11]

In this chapter, several theoretical methods, such as the Disk-Actuator, the Lifting Line, the Vortex Lattice theories and the Panel method were briefly described since these have a huge importance in the propeller analysis and the BET and BEMT were deeply described due to being the most common models used by softwares. At the end, a parametrization of the propeller was performed with the objective of establish which parameters will be analysed and how important is their analysis.

Chapter 3

Numerical Propeller Analysis

In this chapter, the way each software works will be described and at the end, it will be decided which one will be implemented for the propeller performance analysis and optimization to be conducted in subsequent work.

3.1 Software Description

3.1.1 AKPD/AKPA

AKPD/AKPA is a software built for the design and analysis of open propellers and multi-component propulsors and it was developed by State Marine Technical University (SMTU), together with Marintek [12]. This software has a design algorithm based on a nonlinear surface theory while the propeller analysis is based on the Blade Element Theory. The program consists mainly of two parts: the design program AKPD and the analysis program AKPA. The main difference between these two parts is that AKPA allows the calculation of propeller geometry in open-water conditions and into a prescribed flow. The several kinds of propellers which this software can handle are shown in figure 3.1.

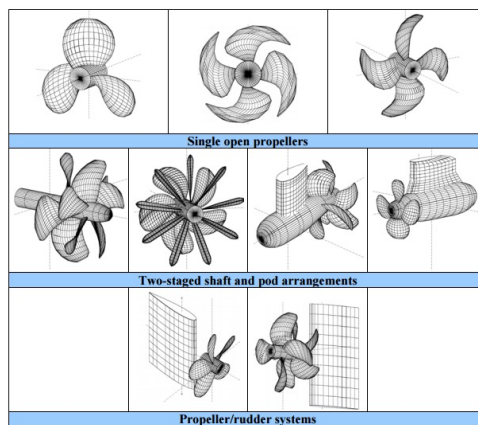


Figure 3.1: Types of propellers analysed by the software [12]

The design program AKPD implements the design calculation of the propeller by defining the pitch and chamber of the blade sections according to the main propeller parameters, such as diameter, RPM, number of blades, blade chord and blade thickness.

The main objective of this program is to meet the required operation point (J, C_T). The design calculation is performed either in uniform flow and in pre-set radial variable inflow.

The analysis program performs steady and unsteady calculations for a given propeller by only prescribing an external velocity field, except when there are oblique flows due to the shaft inclination. The main outputs are:

- Propeller integral performance: C_T, C_Q, η , force and momentum Cartesian components, which are given independently for each section of the blade;
- Total horizontal, vertical and side force components;
- Blade pressure distribution;
- Induced velocity field of the propellers in environment.

Due to this software not being available, it is not possible to run any analysis, however, its working method is all explained in [12].

3.1.2 Javaprop

JavaProp [13] is a software used for the design of propellers and wind-turbines and it is used either on aeronautical and marine applications. The software is based in Blade Element Momentum Theory. So, it has some limitations such as:

- The disk-loading of the propeller must be lower than 2;
- The propeller must have less than 15 blades to avoid interactions due to thickness;
- Three-dimensional effects are not taken in account;
- Compressible effects are ignored.

JavaProp is based on an inverse design module which means that the user starts by specifying only a few basic parameters, as shown in figure 3.2, and a geometry is automatically produced for the optimum propeller efficiency. Later, it is possible to modify this design to adapt to additional off-design conditions.

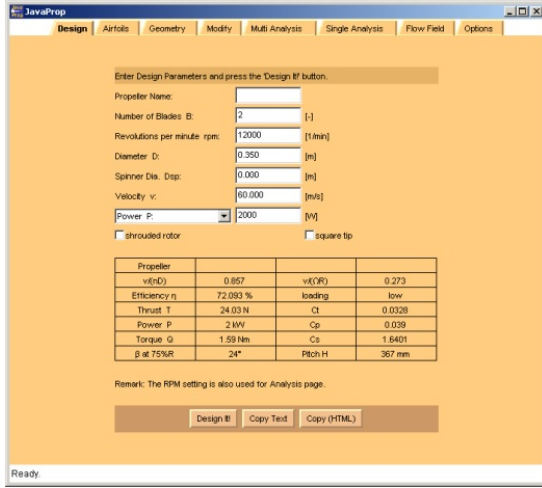


Figure 3.2: Design card of JavaProp [13]

The most relevant cards for the design of the propeller in this software are Design, Airfoils and Options cards.

As it can also be seen in figure 3.2, it is possible to choose the option between a shrouded rotor and a square tip. The several advantages and disadvantages of each one are explained in [13].

In addition to the basic parameters of the Design Card, it is necessary to select the airfoils. JavaProp has already some examples of airfoils and its tables and graphics of lift and drag coefficients versus angle of attack. However, it is also possible for the user to define new airfoils and to implement them on the software.

At this stage, airfoils must be selected for the four radial stations and the respective angle of attack. The maximum efficiency is obtained when each airfoil is being operated at its maximum L/D. An example can be seen in figure 3.3.

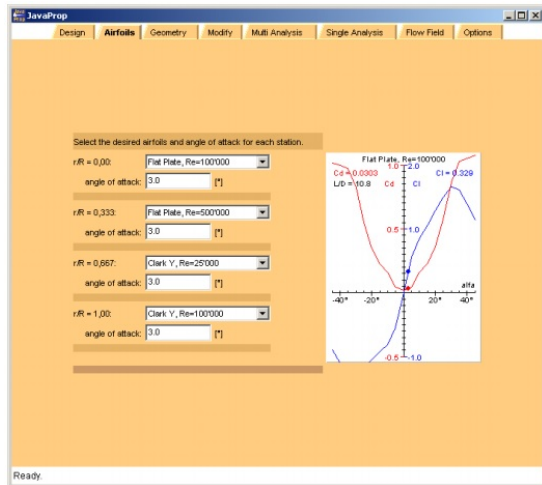


Figure 3.3: Airfoils card of JavaProp [13]

At the end, in the Options card, the density of the fluid is used as a design variable. For example, a propeller designed for a low density medium must have blades with a larger chord than a propeller in a high density medium. The explanation for the other cards can be found in [13]. With this software it is

possible to make two kinds of analysis: Multi-analysis and Single analysis.

The multi-analysis card is used to analyse the propeller in its complete operating range since static operation until the beginning of the windmilling regime at higher velocities. The output of this card consists of the global data of the propeller, showed in graphics of thrust, power and efficiency versus the advance ratio. An example of the output window of a multi-analysis is show in figure 3.4.

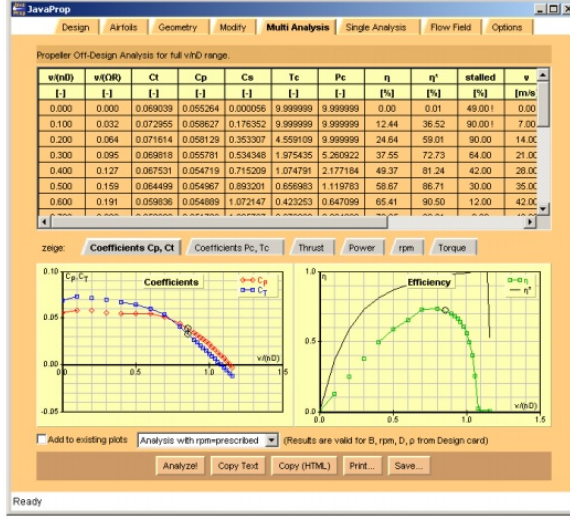


Figure 3.4: Multi-analysis card of JavaProp [13]

The single-analysis card is used to analyse the propeller at a single point defined by the flight velocity U , the rotational velocity N and diameter D on the Design Card.

The output of a single-analysis is more detailed than the previous one because it consists of the distribution of the aerodynamic parameters in every sections along each blade, which also includes coefficients related to structural loads. The display of the results presentation for this kind of analysis can be seen in figure 3.5.

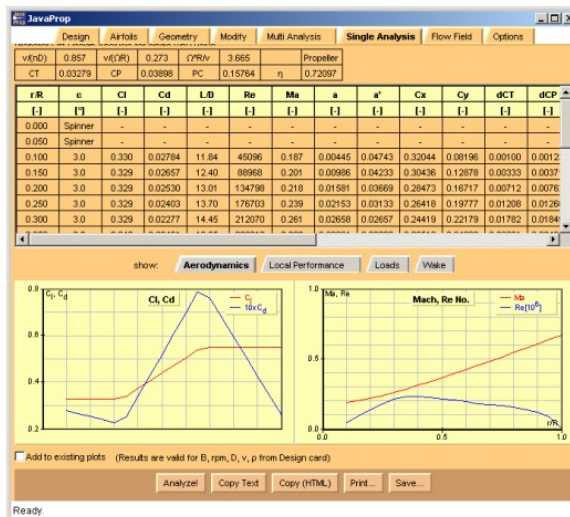


Figure 3.5: Single-analysis card of JavaProp [13]

3.1.3 QProp

QPROP [14] is an analysis program which has the ability to predict the propulsive performance using several combinations of electrical motors and propellers.

Relatively to the aerodynamic propeller model, this one consists of an enhanced version of the analysis method developed by Larabee [15]. It is possible to say that the high-accuracy of this software is primarily due to the correct accounting self-induction of the propeller, which allows the study of the performance even with high disk-loadings, mainly in the static-thrust case. The function between the lift coefficient versus angle of attack of the blade airfoil is assumed to be linear, so it is only necessary to define the values for the maximum and minimum lift coefficient. Relatively to the profile drag function, its characteristic curve results from a quadratic $C_d (C_l)$ function of the airfoil. To execute the software there are two main files that are necessary: the motor file and the propeller file.

There are two different types of motors. The default motor type 1 corresponds to a DC motor and is modelled using the following variables:

- Constant K_v that corresponds to the ratio between the motor rotation speed and the voltage;
- Electrical resistance R ;
- Constant rotational friction described by a zero-load current I_0 .

The equations used to calculate each parameter are described in [14]. In figure 3.6, it is possible to visualise an example of a type 1 motor file.

```
Speed-400 3321 (6V) direct drive      ! name
1          ! motor type (1 = permanent-magnet brushed or brushless DC motor)
0.31      ! motor parameter 1 , R (Ohms)      for motor type 1
0.77      ! motor parameter 2 , Io (Amps)     for motor type 1
2760.0    ! motor parameter 3 , Kv (rpm/Volt) for motor type 1
.
.
```

Figure 3.6: Example of a type 1 motor file [14]

The motor type 2 also corresponds to a DC motor, however, its parametrization is more accurate than the previous one. In this model, the extensions are improved models of frictional torque, temperature-dependent resistance and magnetic lags. A more complete description might be found in [14]. In figure 3.7, it is possible to visualise an example of a type 2 motor file.

```
Speed-280 6328 (6V) direct drive
2          ! motor type (brushed DC, higher-order model)
0.70      ! R0      (Ohms)
0.160     ! Io0     (Amps)
3800.0    ! Kv      (rpm/Volt)
3800.0    ! Kq      (Amps/N-m)*30/pi
1.0E-5    ! tau     (s)
5.7E-5    ! Io1     (Amp-s)
4.0E-8    ! Io2     (Amp-s^2)
0.012     ! R2      (Ohms/Amps^2)
```

Figure 3.7: Example of a type 2 motor file [14]

Relatively to the propeller file, QPROP requires a detailed description of the propeller geometry and of the blade airfoil characteristics. For some softwares, it is only necessary to specify the diameter and the pitch, however, for QPROP that is not enough. The propeller must be measured in an detailed and accurate way. An example of a propeller file is shown on figure 3.8.

```

Graupner CAM 6x3 folder
2      3.05 ! Nblades [ R ]
0.50  5.8   ! CL0     CL_a
-0.3   1.2   ! CLmin   CLmax
0.028  0.050  0.020 0.5   ! CD0     CD2u   CD2l   CLCD0
70000   -0.7   ! REref   REexp
0.0254  0.0254  1.0   ! Rfac   Cfac   Bfac
0.          0.       ! Radd   Cadd   Badd
# r      chord   beta
0.75    0.66   27.5  ! root station
1.00    0.69   22.0
1.50    0.63   15.2
2.00    0.55   10.2
2.50    0.44   6.5
2.875   0.30   4.6
3.00    0.19   4.2  ! tip station, also gives R = r if R is omitted from Line 2

```

Figure 3.8: Example of a propeller file [14]

By analysing the previous figure, it is possible to verify the format of the propeller file. In the first line, it is written the description name of the propeller. In the second line, some inputs like the number of blades and the radius of the propeller are placed. In lines 3 and 4 the parameters for the definition of the linear function $C_l(\alpha)$ are defined. This function is limited between the minimum and the maximum values of the lift coefficient and is given by

$$C_l(\alpha) = \frac{(C_{l_0} + C_{l_\alpha}\alpha)}{\sqrt{1 - M^2}}. \quad (3.1)$$

In lines 5 and 6, the inputs introduced provide the quadratic function $C_d(C_l, Re)$ for the airfoil, which is given by

$$C_d(C_l, Re) = \left[C_{d_0} + C_{d_2} \left(C_l - C_{l_{C_{d_0}}} \right)^2 \right] \left[\frac{Re}{Re_{ref}} \right]^{Re_{expo}}, \quad (3.2)$$

where the parameter C_{d_2} is determined according to the condition:

$$\begin{aligned} C_{d_2} &= C_{d_{2u}}, \text{ if } C_l > C_{l_{C_{d_0}}} \\ C_{d_2} &= C_{d_{2l}}, \text{ if } C_l < C_{l_{C_{d_0}}} \end{aligned} \quad (3.3)$$

The Reynolds number Re_{ref} corresponds to the value from the polar where the previous parameters are obtained and Re_{expo} is the exponent that adjusts the airfoil drag coefficient for other Reynolds numbers. Usually the value that is chosen to this parameter is - 0.5. In lines 7 and 8 are specified some scaling factors and constants that must be added to define the blade geometry. In this particular case, it is possible to observe the presence of the constant 0.0254 due to the radius input being in inches and all the calculations must be realized in SI units. The blade angle input is in degrees, but the software automatically converts it to radians. From line 9 until the end of the file, all the blade geometry is specified by splitting it in several sections. In each section, the chord and the blade angle are defined, from the root to the tip.

As other softwares, QPROP also makes possible the execution of different types of simulations. The simplest execution is the single-point run. This type of execution consists on a simulation where all parameters are calculated in a given instant of time. The initial conditions are defined and all the analysis are done assuming stationary conditions. To execute this simulation, it is necessary to provide to the software the velocity and the RPM inputs. For multi-point simulations, the parameters that are used in single-point simulation are replaced by an initial value, a step and a final value. So, it is possible to verify that, in this type of simulations, the conditions are no longer stationary which enables to make different simulations and obtaining different results by varying the velocity or the RPM.

3.2 Software Implementation

In the previous section, three softwares that exist to analyse propellers were described.

By analysing the software AKPD-AKPA, it is possible to verify that it is capable of making several types of simulations, requiring similar inputs to JavaProp. Its outputs are not just data disposed in tables, but also three-dimensional diagrams with distributions of some important parameters, such as pressure. It must be taken in account that it is desired to execute this program using an external software, in this case MATLAB[®], to later enable the optimization process. As so, it would be necessary to have access to the Java classes files that allows MATLAB[®] to create and implement this software. Also, due to the fact of this software not being available commercially, since only SMTU and Marintek are allowed to use it, it is not possible to show an example of an analysis using this software.

Another software that was described was JavaProp. Due to this software being based on Java programming, it is possible to use it with MATLAB[®], by using Java classpaths provided by the author Martin Herpelle. However, it only enables the analysis of optimised propellers and does not account with the motor analysis, so the user only has the possibility of defining the inputs required by the program.

The last software analysed, QPROP, is the simplest to use and to implement since MATLAB[®] has a command that allows to execute external software. Since to execute the program all the details of the motor and the propeller are required, including its geometry, the software allows to test all kind of propellers.

To compare the performance and reliability of both available softwares, it was done a simulation of a propeller 24"×9", at a airspeed of 7 m/s and a rotation velocity of 2000 RPM, with a Clark-Y airfoil at $Re = 100000$. As expected, the output parameters from the softwares are different, so only the matching parameters can be compared. The results are presented in table 3.1.

Software	J	C_T	C_P	P [W]	T [N]	η [%]
JavaProp	0.35	0.0264	0.017	60.01	4.64	54.23
QPROP	0.35	0.0274	0.0153	54.13	4.83	62.51

Table 3.1: Comparison between JavaProp and QPROP analysis

By analysis of table 3.1, it is possible to verify some differences in the analysis between the softwares. The existence of these differences is justified by the fact of each software uses different methods to

calculate each output and due to the difference of the airfoil characteristics provided by the software JavaProp and the parameters of the polar drag curve calculated on the software XFOIL [16]. The values presented in previous table are already in the same units, however, it is important to notice that JavaProp and QPROP use formulas with different units to calculate the values of C_T and C_P . So, to allow the correctly comparison of these values, it is necessary to convert the values to the same unit.

Although the desired software to use is QPROP, the desired formulas are the ones described in section 2.2. As so, the values that QPROP exports must be converted. The formula that QPROP uses to calculate the thrust coefficient, C_T , is given by

$$C_{T_1} = \frac{T}{\frac{1}{2}\rho(\Omega R)^2\pi R^2}. \quad (3.4)$$

By converting equation (3.4) to the units of equation (2.19), it is obtained the conversion

$$C_T = \frac{\pi^3}{8}C_{T_1}. \quad (3.5)$$

In relation to the C_P values, it is possible to verify the same difference in the units of the formula used by QPROP. The formula QPROP uses is given by

$$C_{P_1} = \frac{P_{shaft}}{\frac{1}{2}\rho(\Omega R)^3\pi R^2}. \quad (3.6)$$

By converting equation (3.6) to the units of equation (2.20), it is obtained the conversion

$$C_P = \frac{\pi^4}{8}C_{P_1}. \quad (3.7)$$

After describing the three softwares, it is possible to verify that the software AKPD-AKPA can not be chosen to perform the analysis since it is not available to be used. As such, the software that was selected to be used in the propeller analysis and design framework was QPROP due to the fact of allowing the analysis of any propeller, and not just an optimized propeller and due to the fact of being the only software that considers the entire system motor+propeller.

Chapter 4

Experimental Facility

In this chapter, initially, the characteristics of the electrical motors that were used and the acquiring data methods from the propeller and the airfoil will be briefly described. Then, main characteristics of the wind tunnel are also described and at the end the structure, the corrections made on the motor support system, the sensors of the force balance used to perform the tests and the processes of calibration of each sensor are also referred and described.

4.1 Electric Motors

The motors used in this thesis are DC electrical motors which basically, are electromechanical devices whose main function consists in converting electrical power received from a battery into mechanical power which assures the rotation of the motor shaft, using Direct Current.

There are two main types of *DC* electrical motors: brushed motors and brushless motors. While the brushed motors use a mechanical system of commutation, the brushless motors use an electronic system to change the direction of the electric current and generate a pulling magnetic force between the stator and the magnets.

The motors that are being used are brushless since these type of motors present some advantages in relation to brushed motors, such as higher efficiency, longer lifetime, lower noise generation and higher $\frac{P}{W}$.

Within the range of brushless motors, it is also possible to distinguish between in-runner, where the magnets are placed on the shaft of the motor and the windings at the outer part of the motor and out-runner, where the magnets are turning around the stator.

In spite of the in-runner has some advantages such as having a lower inertia, which allows it to reach higher values of RPM, the out-runner has a cooler running and provides higher values of torque which eliminates the necessity of using a gear-box [17].

The two motors used were the O.S. Engines OS-3810-1050 and OS-5020-490 [18], whose characteristics are presented in table 4.1, where I_{max} is the maximum current supported by the motor and η_{max} is the maximum efficiency the motor can reach.

Motor	Shaft Diameter [mm]	V^* [V]	I_{max} [A]	I_0 [A]	η_{max} [%]	K_v [RPM/V]	R [mΩ]
OS-3810-1050	5	12.5	30	1.1	85	1050	51.3
OS-5020-490	6	21.0	68	1.5	85	490	23

Table 4.1: Characteristics of the electric motors

To allow the connection between the motor and the propeller, there is a structure called spinner, which has a conic shape, usually metallic, held by the motor shaft and holding the blades, as it can be visualized in figure 4.1.



Figure 4.1: Spinner [19]

Usually, this device is used because it streamlines the incoming air toward the cooling inlets and the motor. In the cases where the propeller is controllable, it also protects the mechanisms used to control the propeller blades.

However, it is necessary to pay attention to this device because it is subjected to high stresses, which can cause cracks on its surface. These cracks lead to vibrations that may cause fatigue and the loss of the spinner during the flight.

A spinner is basically constituted by three main parts: the spinner itself and two main bulkheads. The propeller is placed between the bulkheads and the spinner is attached with fasteners to both bulkheads. It is important to center this structure to avoid vibrations while the motor is running. More information about the manufacture process of a spinner may be found in [20].

In this thesis, two different spinners are used, each one for each motor. The smallest spinner has 38mm of diameter and a shaft diameter of 5mm. The biggest spinner has 47mm of diameter and a shaft diameter of 6mm.

4.2 Propellers

4.2.1 Description of Tested Propellers

The first propeller to be analysed was an APC 13"×8", which means that the propeller has a diameter of 13 inches and has a pitch of 8 inches. The pitch is the axial distance that a propeller can perform on a single revolution.

To compare the performance by varying the diameter, the second propeller was an APC 16"×8". As it can be seen, it has the same pitch as the previous one, however, it has a diameter of 16 inches, which enabled to verify how does the performance change with the increasing of the diameter of the propeller.

Finally, to compare the performance for propellers with the same diameter, but with different pitch, the third propeller was an APC 16"×10", which enabled to evaluate the change on the performance due to the pitch increase.

Since different propellers were to be tested, it was important to choose the most adequate motor for each propeller to obtain the highest possible value of efficiency. Therefore, different systems motor+propeller were considered.

For the APC 13"×8", the two available brushless out-runner electrical motors described in section 4.1 were used to compare the performance between them. For the APC 16"×8" and the APC 16"×10", the motor used was the OS-5020-490.

4.2.2 Manual Geometry Measurement

Due to the fact of the non-existence of geometry details of any of the propellers to be tested, it was necessary to find a way to measure them. The method described below was used for all propellers.

Initially, each blade was measured from the hub until the tip to determine the propeller radius. The instrument used to make all the measures was a calliper with a scale of $1 \pm 0.05 \text{ mm}$ shown in figure 4.2.

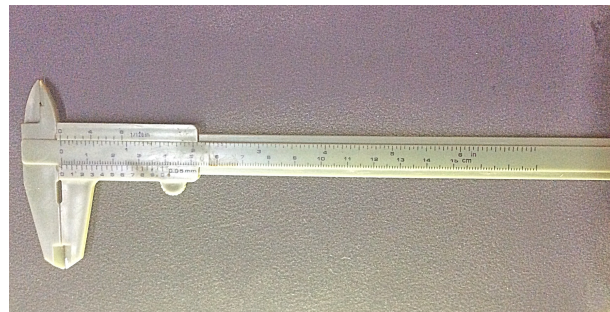


Figure 4.2: Calliper used to make the blade measurements

After measuring the radius, the blade was placed in a glass surface. The purpose of using this type of surface was the definition of a referential to make the measures and to have a smooth surface to avoid as much as possible some uncertainties in the measurements. Then, the blade was divided in several sections with a given length using white ink and a tissue line. The result of this stage can be seen in figure 4.3.



Figure 4.3: Blade divided in sections

Following that, the heights h_1 and h_2 of each section were measured with the calliper. The blade was then removed from the surface and the chord of each section measured. A scheme of the previous explanation is presented in figure 4.4.

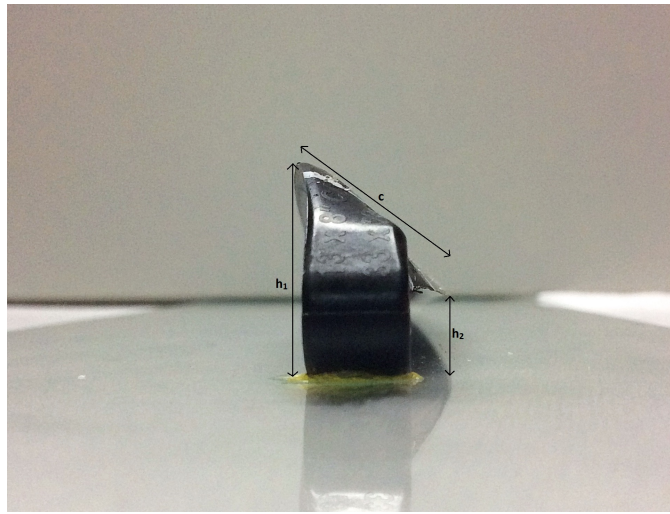


Figure 4.4: Scheme of the measurement procedure of the blade

As it can be seen in figure 4.4, by measuring the heights h_1 , h_2 and the chord c , it was possible to determine the β and the chord distributions along the blade, for each section k , as

$$\beta_k = \arcsin \frac{h_{1k} - h_{2k}}{c_k}. \quad (4.1)$$

4.2.3 3D Laser Scanning Geometry Measurement

Due to the fact of the measuring method described previously not being particularly accurate, an alternative method was tried, namely a 3D laser scanning.

This method was performed by handling a laser scanner that uses reflective markers to position the object in space, needing only a computer and an appropriated software to use on the data acquisition. The 3D Scanner used is the $ZScanner^{TM}$ 700 together with the software $ZScan^{TM}$. The device specifications are presented in [21].

To measure the three different propellers, three independent tests were executed, in which each blade was marked, put on a black board and then scanned. It was important to take into account that

the black board was also filled with markers with a minimum distance of 20 mm between each other, with the objective of avoiding regular distribution and positioning errors that it could cause. It was also important to keep the distance between the board and the scanner near from 300 mm [21].

The procedure of this process can be visualized in figure 4.5.

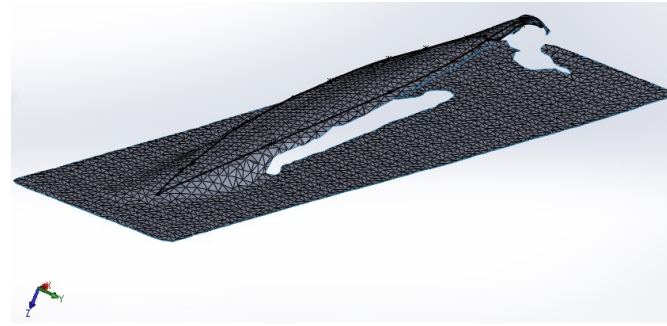


Figure 4.5: 3D scanning measurement of the blade

After scanning, the acquisition data was saved in a file with a *.stl* format and then treated in SOLIDWORKS®, to enable the splitting of the blades in the same number of sections. These sections should have been equally distant, as the ones measured before to make possible the comparison between the geometric data of each propeller. In figure 4.6, it is possible to visualize several views of the results of the measures performed using this method.



(a) Front View



(b) Rear View

Figure 4.6: 3D CAD model of a measured blade

However, this method showed to be very inaccurate, due to the imprecision of the measuring laser system used and, as so, the measurements obtained by the method described in 4.2.2 were used in the initial simulations.

4.2.4 Airfoil Drag Polar

To predict the performance of a propeller, it was not enough to determine only the geometry parameters, it was also necessary to determine the airfoil parameters.

According to [22], the airfoils used in APC propellers are the Clark-Y and the NACA 4412. However, there was not any information about what airfoil was used in the propellers in use. As such, simulations were performed to determine the aerodynamic parameters of each one of these airfoils. To determine all the aerodynamic parameters for both airfoils, the software XFOIL was used [16].

Initially, it was obtained a reading file with the airfoil points coordinates [23] and then these were loaded in XFOIL. Before the execution of the simulations, a mesh refinement on the leading and trailing edge was made to assure a better accuracy on the final results. According with [24], to calculate the Reynolds number to set in these analysis, it was considered that

$$Re = \frac{\rho \Omega R c_{avg}}{\mu}, \quad (4.2)$$

where c_{avg} is the arithmetic mean of the chord values of each section, for each propeller and μ is the kinematic viscosity. Taking in account the characteristics of each system motor+propeller, it was expected in this phase that all systems could reach a rotation speed of 5000 RPM, which corresponds to 533.33 rad/s, without damaging the motor. As such, this was the value considered on these calculations for the angular velocity of the propeller and sea level conditions were considered as approximation [8]. The data obtained for each propeller is presented in table 4.2.

Propeller	c_{avg} [mm]	R [mm]	Re
APC 13"×8"	17.47	145	94416
APC 16"×8"	20.37	183	138908
APC 16"×10"	21.15	180.2	142073

Table 4.2: Determination of Reynolds number

Since it was desired to set an unique Reynolds number for all the propellers and by analysing the table 4.2, it was decided to set the Reynolds number to $Re = 100000$ due to this value being a good approximation of all the tested cases. To allow the software to calculate the values of C_l and C_d to build the polar curve, a sequence of angles of attack was defined, starting in the angle for minimum lift coefficient and ended in an angle higher than the one for maximum lift coefficient, to have a more detailed curve, with a step of 0.05°. The resulting graphic can be visualized in figure 4.7.

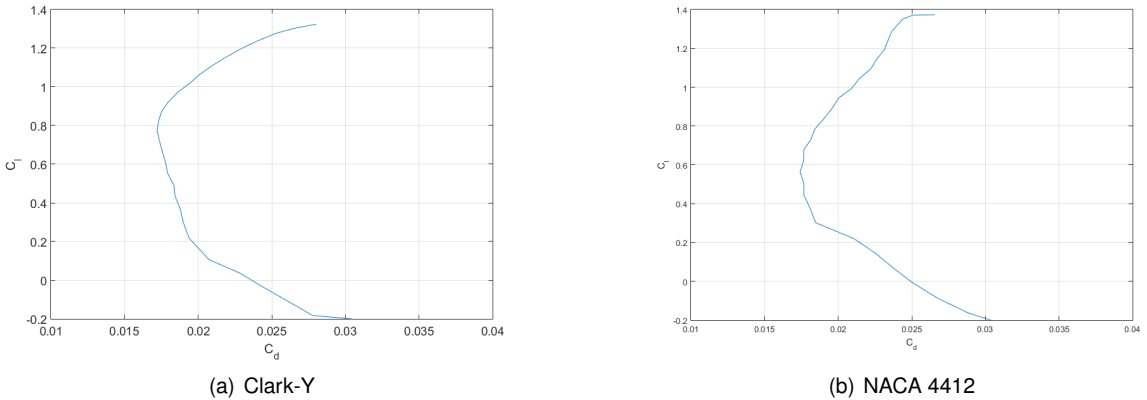


Figure 4.7: Polars from the different possible airfoils in use

While building the polar drag curve, the software also produced a file with all the data used to build the graphic. As such, it was possible to find the values of C_{d_0} and $C_{l_{C_{d_0}}}$ by searching these points where C_d presented the lowest value and its corresponding value of C_l . To find the value of $C_{d_{2u}}$ for each airfoil, the last point from the polar curve was chosen, corresponding to an angle of attack of 4° , where $C_l \gg C_{l_{C_{d_0}}}$ to avoid errors in the calculations since that the polar shown in figure 4.7 does not present a total parabolic behaviour. To find the value of $C_{d_{2l}}$ the same procedure was done, but for the point corresponding to an angle of attack of -1.35° where $C_l \ll C_{l_{C_{d_0}}}$. This specific point corresponds to the last point where the polar curve varies in a constant way. To estimate the variables described above, equation (3.2) was used. As an approximation, it was considered that $Re = Re_{ref}$.

After defining all the geometric and airfoil characteristics, these were put in three different files, each one corresponding to a different propeller. The detailed input files, for each airfoil, can be analysed in figures A.1, A.2 and A.3 in Appendix A.

4.3 Wind Tunnel

To obtain the desired data for the determination of the parameters of the propeller, it is necessary to perform static and dynamic tests on the wind tunnel. The wind tunnel where these tests were performed has a closed circular section with a diameter of 1.3 m, can produce a maximum flow velocity of 40 m/s and it is located in the Aerospace Laboratory at Instituto Superior Técnico. Previously, some tests were made[25] with the main objective of measuring some parameters, such as the flow velocity and the acoustic noise in function of the motor operation frequency that drives the wind tunnel fan.

During the tests, the physical variables measured were:

- The fan motor operation frequency in Hz;
- The continuous voltage on the terminals of the associated signal conditioned module associated to the differential pressure sensor, used to measure the dynamic pressure, in V, connected to a Pitot tube;
- The acoustic noise measured by a sonometer in dBA.

After making some tests, all the relations between the several variables were found. The relation between the frequency f and the flow velocity U found at the time is given by

$$U = 1.2635f . \quad (4.3)$$

However, this relation was obtained with the use of a converging nozzle upstream of the test section of the wind tunnel. As such, a new calibration was performed since the nozzle was removed. After making the new calibration, the obtained relation was

$$U = 1.325f - 0.38 . \quad (4.4)$$

The graphic obtained with the relation between the flow velocity and the frequency is shown in figure 4.8.

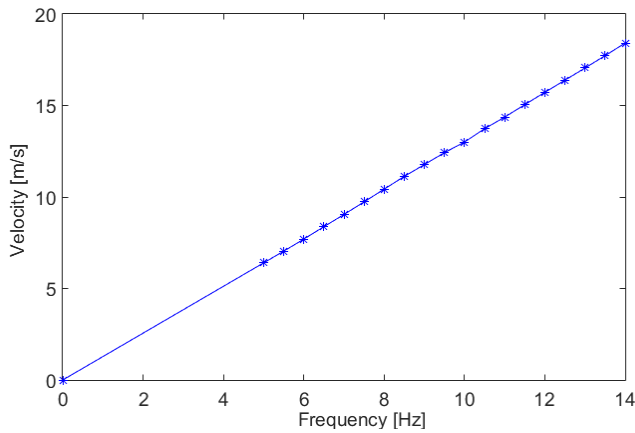


Figure 4.8: Relation between flow velocity and frequency [25]

There are also some recommendations about the realization of similar tests, such as the maintenance of its components, the checking of the consumed power by the motor and to define the maximum frequency values that can be used to define the maximum value of the flow velocity.

4.4 Force Balance

To enable the measurements of the propeller performance during experimental tests, a force balance previously built was used [1]. This section will be split in three subsections:

- Structure, where the structural studies that were made to achieve the actual geometry of the balance will be referred;
- Sensors, where all the electronic devices and the software used to obtain the performance data will be described;
- Calibration, where the processes of calibration of each sensor to assure the accuracy of the obtained results will be described.

4.4.1 Structure

According to [1], the construction of the balance was divided in several stages, which are presented in the diagram of figure 4.9:

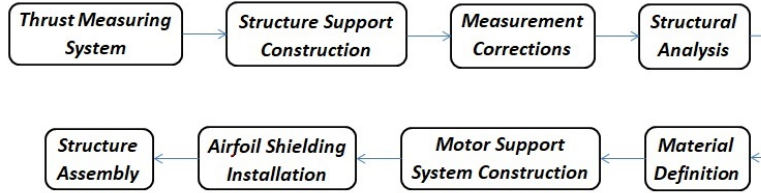


Figure 4.9: Diagram with the several stages of construction of the balance

As it can be read at [1], every stages described in the diagram of figure 4.9 were carefully studied and analysed to choose the best options to fulfil all the requirements. The final assembly of the built balance can be visualized in figure 4.10:

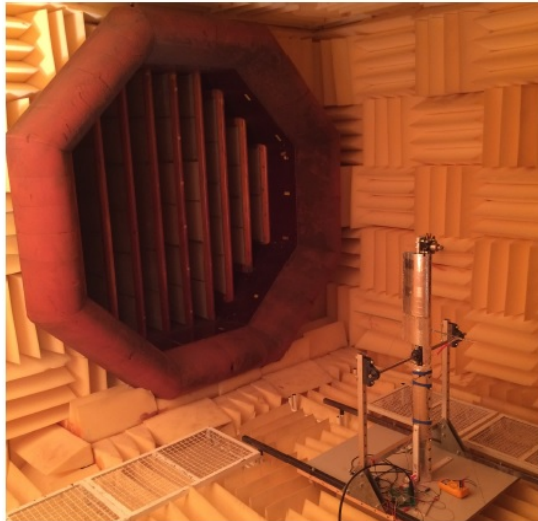


Figure 4.10: Final structure assembly [1]

There was the possibility of varying the position of the load cell along the main beam. Each hole was distanced 55 mm from each other and the value measured at the load cell depended of where the user would position it. In this thesis, the load cell was chosen to place at an equal distance from the pin held in the main beam as the one from the pin to the motor support system. This means that the force that was detected in the load cell was the actual force that was being applied in the support system.

For the design of the connection between the motor and the propeller, some changes had to be done since the previous support was oversized. The CAD model of the new designed structure is presented in figure 4.11 and the list of the main components can be visualized in table 4.3.

Component	Name
1	Motor
2	Support Plate
3	Structural Cross
4	L connection

Table 4.3: Description of the components of the system propeller+motor [1]

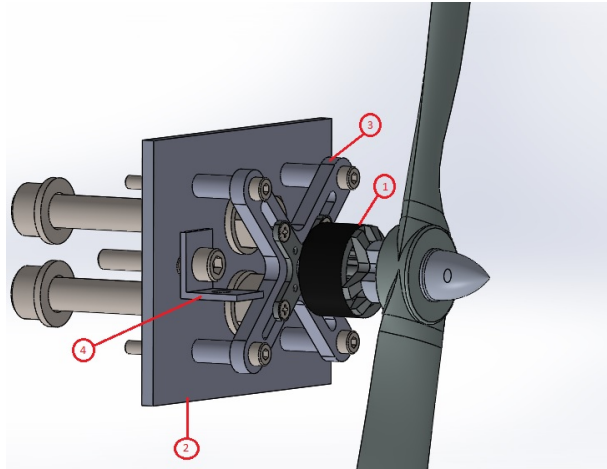


Figure 4.11: Support of the system motor+propeller

The cross was then supported by four bolts that cross the plate, which were resized to correct the over-dimensionating on [1]. According with [1], the balance was designed with a capability to test propellers up to 27" of diameter that can generate a force equivalent to 30 kgf. Using the method present in [26], it was concluded that the best option would be to replace the existing M10 bolts by M4 bolts of Steel AISI 1035HR, which would still provide a safety factor of 32.

Since the previous structure was not properly sized to install the motors in use in this thesis, it was necessary to build new structural crosses and new structural plates to support each motor. To build the structural crosses, a 3D Printing process was used, using PLA as construction material. The structural plates were replaced by new ones made of acrylic and the new holes were made using a drilling process, for each plate. It is possible to observe the new measuring system in figure 4.12.



Figure 4.12: Resized support of the system motor+propeller

4.4.2 Sensors

To enable the measurement of the necessary data to analyse the performance of the motor and the propeller, it was necessary to mount sensors installed in the structure. In this balance there were:

- Load Cell;
- Voltage and Current sensors;
- RPM sensor;
- Temperature sensor;
- Airspeed sensor.

For the load cell sensor, the Vishay Model STC [27] was chosen. This load cell can be used in traction or compression and it becomes with a signal conditioner to amplify the voltage output cell to have a better fulfillment of range values.

To measure the voltage and the current, the 60 V version of PitLab 75A [28] were chosen due to its simplicity on the wiring and the possibility of measuring both inputs at the same time.

To measure the RPM, the Sensor CNY 70 from Vishay [27] was chosen. In this process, the motor was lined with a black and white tape and when passing by the black part of the tape, a different frequency was generated in the sensor, which allowed it to calculate the RPM value.

For the temperature sensor, the Analog Devices TMP36GZ [29] was chosen, to measure the temperature of the air stream and the temperature of the motor.

To measure the airspeed, two sensors Freescale MPXV7002DP from NXP [30] were used, due to the fact of the first one being used to measure the static pressure and the second one to measure the total pressure. With these two values of pressure, the software obtained the airspeed value using Bernoulli

equation,

$$U = \sqrt{\frac{2(P_{tot}^* - P_{static}^*)}{\rho}}. \quad (4.5)$$

To control the speed of the motor, an Electronic Speed Control (ESC) was chosen. Using a Pulse Width Modulation (PWM) and the software Labview[®] Interface, the sensor detected the signal generated by the motor and then it was set on. As much time the signal was on, the higher was the power on use. More information about the calibration of this sensor is presented in [1].

To compile all the data acquired by the sensors, a DAQ system NI PCIe-6321, from National Instruments was used. This system was installed in a board similar to the one shown in figure 4.13 and it was directly connected to a computer where the user could analyse the overall experimental data.



Figure 4.13: Data acquisition hardware [1]

As referred previously, for the realization of the tests, the user had to have a way to control the inputs. The simplest way to enable it was the creation of an Interface using the software Labview[®] Interface. A scheme of the main interface can be visualized in figure 4.14. In the interface, initially, the user established the correct position of the load cell and only then, it was possible to start the program.

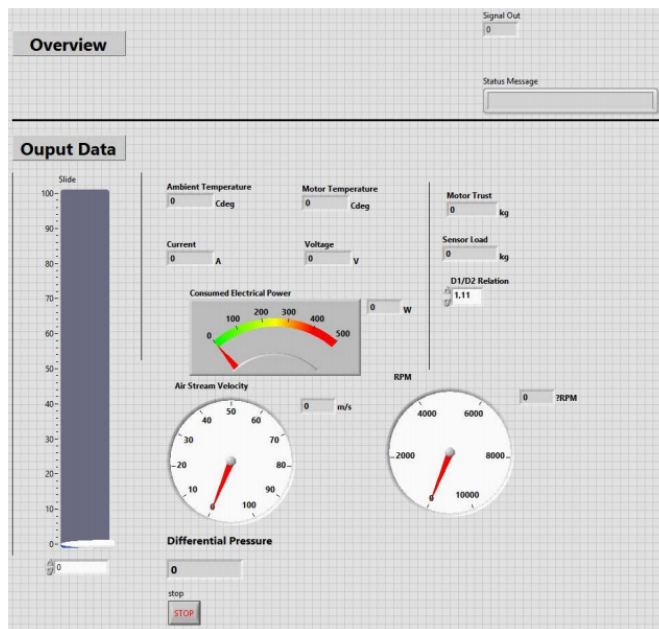


Figure 4.14: Labview[®] interface [1]

More details about the force balance can be found in [1].

4.4.3 Calibration

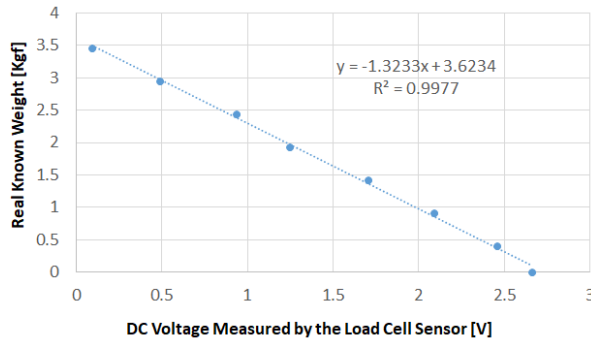
Before starting the experimental tests, it was necessary to make sure that the obtained values would be correct and accurate. For that, it was necessary to calibrate some of the sensors that were used. The sensors that had to be calibrated were the load cell sensor, the voltage sensor, the current sensor and the airspeed sensor.

Initially, the load cell sensor was calibrated using a sheave system. In this system, a wire was attached to the motor, perfectly straight between the motor and the sheave to provide the best possible accuracy of the results. The assembly system can be visualized in figure 4.15.

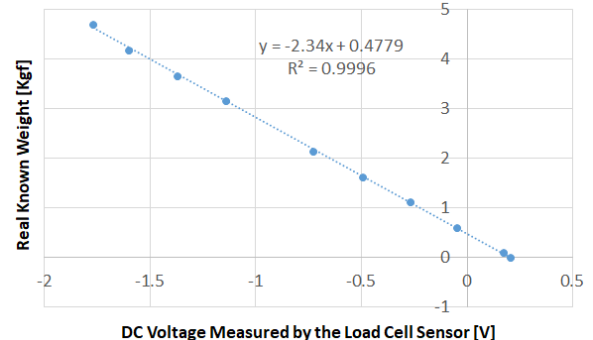


Figure 4.15: System used on the load cell calibration

Then, the load cell was mounted without any weight applied and was "zeroed" by applying an offset in the LabView® software. After this stage, several load weights were applied and the values measured by the load cell sensor were registered. Then, using the registered data, a linear regression was made to define the relation between the load applied and the voltage measured by the sensor [1]. In the experiments, two different load cells were used: one with a load range corresponding to 5 kgf and another with a load range corresponding to 10 kgf . The use of two load cells was justified by the fact of being expected that the larger propeller could produce loads that exceed the range of the load cell with the lower range. The graphics with the resulting linear regressions are presented in figure 4.16.



(a) 5 kg Load Cell



(b) 10 kg Load Cell

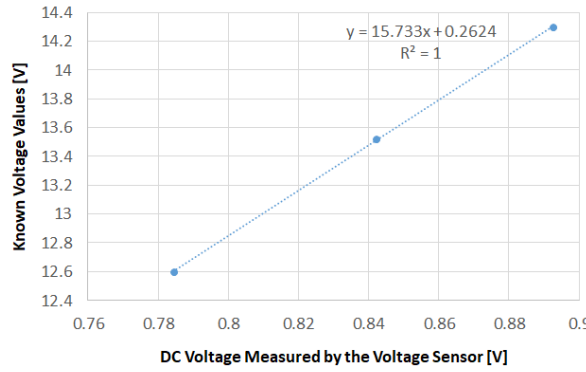
Figure 4.16: Linear regressions used to calibrate the load cell sensors

To calibrate both electrical sensors responsible to measure voltage and current, two tests were conducted. To calibrate the voltage sensor, it was used a multimeter connected to a variable power supply. Two calibrations were performed due to the fact of the different motors work on different ranges of voltage. The calibration of the sensor, using the motor OS-3810-1050, was made in a range from 12.5 V to 14 V, and the calibration using the motor OS-5020-490 was made in a range from 12.5 V to 21.7 V. By increasing the voltage of the power supply, the data from the power supply and the sensor was registered. In figure 4.17, it is possible to see the multimeter used to perform these calibrations. The multimeter is a *CENTER 120 RS232* with a degree of uncertainty of $1 \pm 0.1 \text{ mV}$.

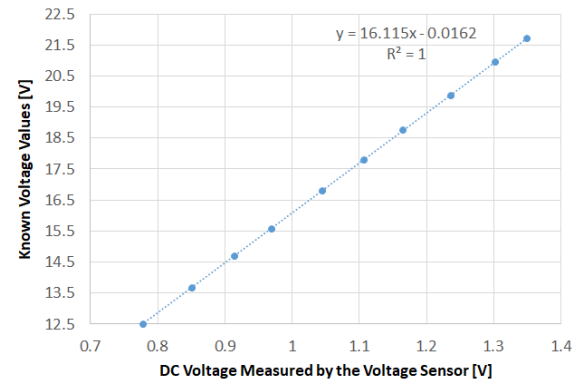


Figure 4.17: Multimeter used to perform the voltage sensor calibrations

The graphics with the linear regressions resulting of the calibrations of the sensor for each motor are presented in figure 4.18.



(a) Calibration using the electrical motor OS-3810-1050



(b) Calibration using the electrical motor OS-5020-490

Figure 4.18: Linear regressions used to calibrate the voltage sensor

The current calibration was performed by increasing progressively the thrust level. This process resulted in the comparison between the DC voltage signal registered by the sensor and the value of the current measured with a current clamp *Center 233*, represented in figure 4.19. This device has a range of current measure from 0 A until 100 A and has a degree of uncertainty of $1 \pm 0.1 \text{ mA}$.



Figure 4.19: Current clamp used to perform the current sensor calibration

The method used to perform this calibration is similar to the one described for the voltage sensor: the obtained data was plotted using linear regression to provide the correct equation to calibrate the sensor. The resulting graphic is shown in figure 4.20.

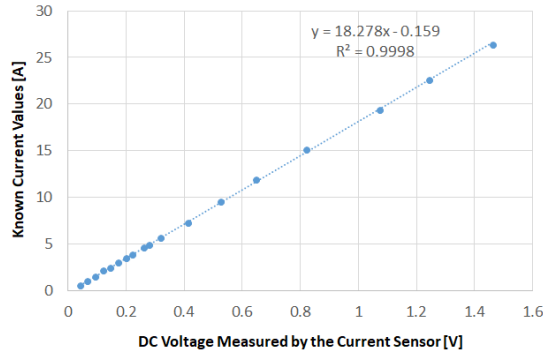


Figure 4.20: Linear regression used on current sensor calibration

The procedure to calibrate the airspeed sensor started with the measurement of the signals obtained by the sensor for each frequency read by the controller present in the wind tunnel. The tests were conducted by varying the frequency of the motor of the wind tunnel and by using two different pitot tubes, connected to two different sensors. One of the pitots was connected to a liquid column manometer system, using mercury as a fluid. The second pitot tube was the one mounted in the force balance. From the first pitot tube, the following relation was obtained

$$P_{dyn}^* = 592.406V^*, \quad (4.6)$$

where P_{dyn} is the dynamic pressure measured using the liquid column manometer system and V^* is the voltage measured by the sensor connected to this pitot tube. Knowing the values of the dynamic pressure and using a linear regression, the relation between the dynamic pressure and the voltage values measured by the sensor connected to the pitot tube placed at the balance was determined. The graphic obtained from this linear regression is shown in figure 4.21.

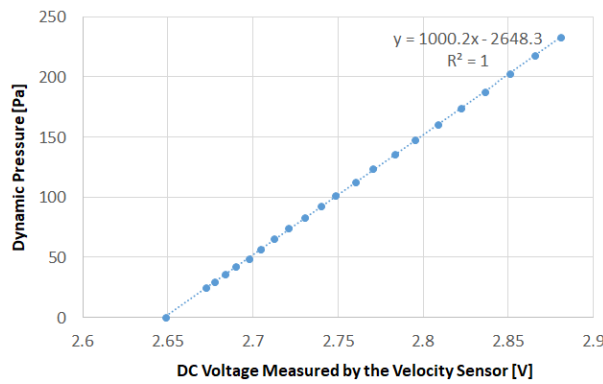


Figure 4.21: Linear regression used in the calibration of the airspeed sensor

The airspeed was then calculated using equation (4.5). The value of density ρ corresponded to the value calculated for the day when the tests were performed.

Chapter 5

Initial Propeller Analysis

In this chapter, the process of execution of the experimental tests for each system motor+propeller will be described and the results of each test will be shown. After this, the way the obtained data can be applied to the LEEUAV will be described and finally, the validation of the software QPROP by comparing the experimental results and the numerical results will be presented.

5.1 Wind-Tunnel Tests

In the propeller performance analysis, it is important to analyse two different conditions: static conditions and dynamic conditions.

Static conditions are verified when the aircraft is at rest (zero axial speed), so there is not any income flow on the propeller's plane. In this case, the propeller produces what is called static thrust. The analysis in this condition is important because it represents the most adverse conditions that a propeller experiences. This study is quite important because, since there is not any air moving towards the propeller due to the inexistence of velocity, the propeller creates its own inflow. Usually, a propeller designed for dynamic conditions has not the best performance under static conditions. This happens due to the flow around small propellers being distorted which can easily originate separated regions and cause stall effects on the blade [31].

However, it is also important to analyse the performance of the propeller when the flow velocity assumes values different from zero. When facing an axial inflow, it is expected that the propeller, for equal values of RPM, may produce lower values of thrust compared with the static case. In these tests, it was necessary to assure that the propeller was operating at high enough RPM values to ensure that positive thrust was being generated. When the propeller rotated at RPM values lower than these minima, it was working as a windmill and not as a propeller.

At this stage, the experimental tests were performed before the realization of the simulations, using the force balance previously described, inside the wind tunnel located in the Aerospace Laboratory at the Mechanical Building III at IST, which had an environment where it was possible to assure a laminar flow.

After mounting the system motor+propeller and every sensors being calibrated, the LabView[®] Interface User software was used. This software allows the user to change the thrust level which causes a direct variation on the rotation of the system motor+propeller.

Before the experiments were conducted, an experiment was performed where the structure was mounted without any blades. In this experiment, the frequency of the wind tunnel fan motor varied from 0 Hz to 10 Hz and then back to 0 Hz and it was conducted twice. By doing this experiment, it was possible to minimize possible errors on the load cell sensor readings due to possible drag caused by the devices that constitute the motor support system.

For the experiments where the motor OS-3810-1050 was used, the thrust level ranged from 10% to 70%, in steps of 5%. The limitation on the maximum value of the thrust level while using this motor was due to the risk of reaching a current value that could damage permanently the motor. For the experiments where the motor OS-5020-490 was used, the thrust level ranged from 10% to 85%, in steps of 5%. However, in the last experiment test, where the propeller in use was the APC 16"×10" and the voltage was set to 21.0 V, the maximum thrust level was only 80% also due to the risk of reaching a current value that could damage permanently the motor.

In the experimental tests, several parameters were analysed for each combination of motor+propeller, for different electrical conditions, in particular:

- thrust;
- electrical power;
- thrust coefficient;
- power coefficient;
- efficiency.

In figure 5.1, it is possible to visualize the graphic with the data acquired on the experiments for the variation of thrust with the variation of RPM and airspeed for the system OS-3810-1050 + APC 13"×8" for an input voltage of 12.5 V.

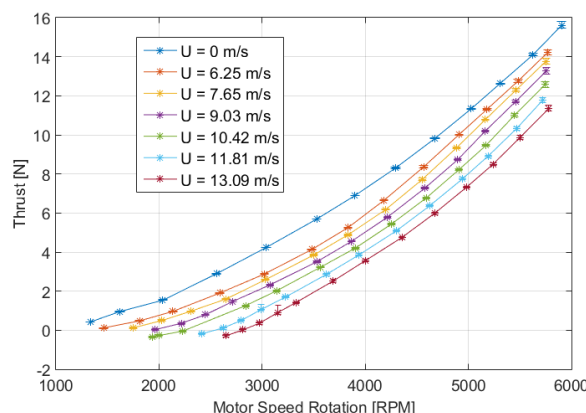


Figure 5.1: Variation of thrust with airspeed and RPM for the system OS-3810-1050 + APC 13"×8" for 12.5 V

By analysing figure 5.1, it is shown that for this system, the load cell sensor presented small uncertainties since the error bars are difficult to be distinguished at the most part of the measured values. It is possible to visualize the higher the airspeed, the lower the thrust and to verify that the relation between thrust and RPM has a cubic parabolic behaviour, for every values of airspeed. It is also possible to notice that the higher the airspeed the higher the RPM necessary for the generation of positive thrust and to see that the maximum thrust value registered was nearly 16 N and it is verified for static conditions. The graphics for the other systems are shown in figure A.4 in Appendix A.

In figure 5.2, it is possible to visualize the graphic with the data acquired on the experiments for the variation of electrical power with the variation of RPM and airspeed for the system OS-3810-1050 + APC 13"×8" for an input voltage of 12.5 V .

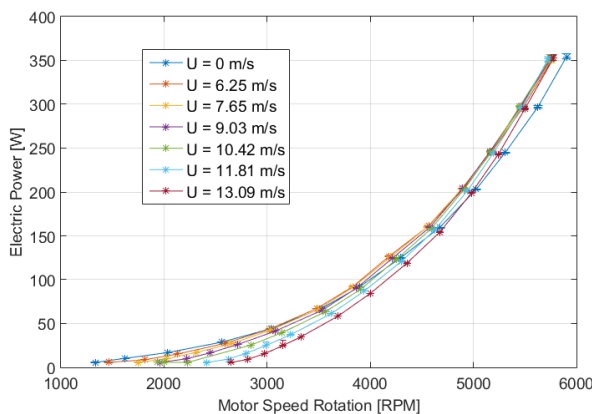


Figure 5.2: Variation of electrical power with airspeed and RPM for the system OS-3810-1050 + APC 13"×8" for 12.5 V

By analysing figure 5.2, it is shown that for this system, the voltage and current sensors presented small uncertainties since, similarly to thrust, the error bars are difficult to be distinguished for most part of the measured values. One thing that is possible to visualize is that the airspeed barely affects the values of electrical power. As such, it is not possible to take any conclusions about the variation of this parameter with the airspeed. It is also possible to notice that, similarly to thrust, the relation between electrical power and RPM has a cubic parabolic behaviour in every cases that are about to be analysed. In this system, the maximum value of electrical power was nearly 350 W . The graphics for the other systems are shown in figure A.5 in Appendix A.

In figure 5.3, it is possible to visualize the graphic with the data acquired on the experiments for the variation of thrust coefficient with the variation of RPM and airspeed for the system OS-3810-1050 + APC 13"×8" for an input voltage of 12.5 V .

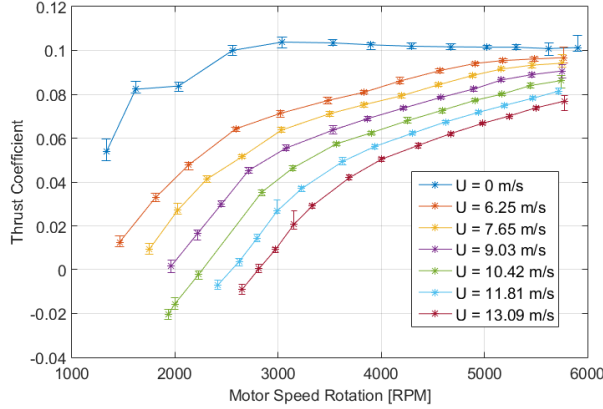


Figure 5.3: Variation of thrust coefficient with airspeed and RPM for the system OS-3810-1050 + APC 13"×8" for 12.5 V

By analysing figure 5.3, it is possible to visualize more easily the error bars, due to the uncertainties associated to the RPM sensor and that the thrust coefficient decreases with the airspeed. It is also possible to note that the relation between thrust coefficient and RPM presents an asymptotic behaviour and that the thrust coefficient negative values correspond to the cases where the produced thrust was negative. Another thing that can be regarded is that the higher the RPM, the lower the effect of the airspeed. The maximum thrust coefficient value registered was nearly 0.1 and, similar to thrust, this is verified for static conditions. The graphics for the other systems are shown in figure A.6 in Appendix A.

In figure 5.4, it is possible to visualize the graphic with the data acquired on the experiments for the variation of power coefficient with the variation of RPM and velocity for the system OS-3810-1050 + APC 13"×8" for an input voltage of 12.5 V.

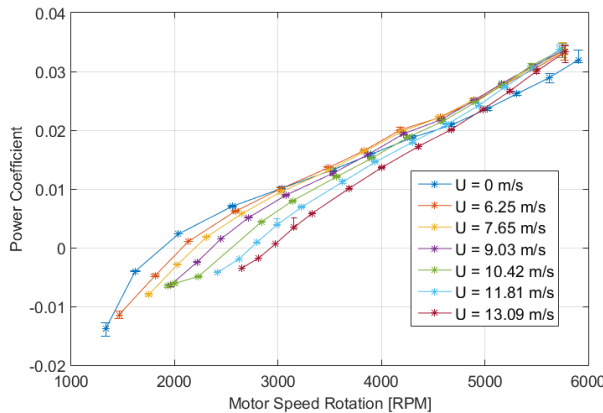


Figure 5.4: Variation of power coefficient with airspeed and RPM for the system OS-3810-1050 + APC 13"×8" for 12.5 V

By analysing figure 5.4, it is possible to notice uncertainties in some points also associated to the uncertainties of the RPM sensor. It is possible to visualize that the airspeed effect over power coefficient tends to vanish with the increasing of RPM. For lower RPM values, it is verified that the power coefficient increases with the increasing of airspeed. The power coefficient negative values correspond to the cases where the current on the motor was lower than I_0 . In this system, the maximum value of power

coefficient was nearly 0.034. The graphics for the other systems are shown in figure A.7 in Appendix A.

In figure 5.5, it is possible to visualize the graphic with the data acquired on the experiments for the variation of efficiency with the variation of RPM and airspeed for the system OS-3810-1050 + APC 13"×8" for an input voltage of 12.5 V:

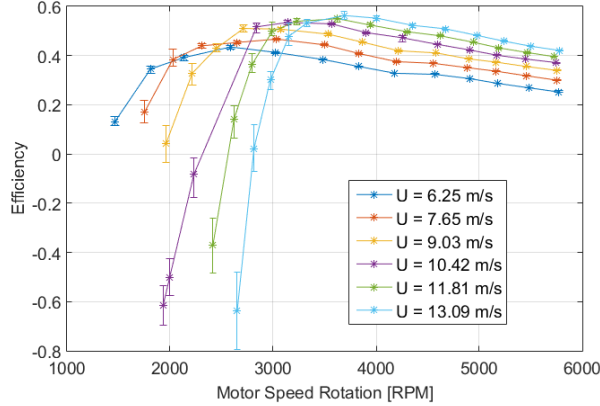


Figure 5.5: Variation of efficiency with airspeed and RPM for the system OS-3810-1050 + APC 13"×8" for 12.5 V

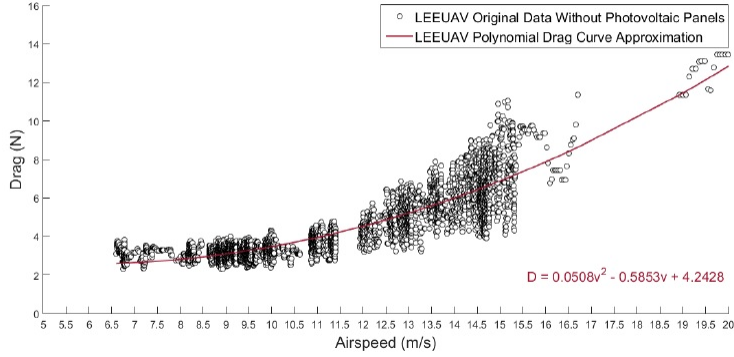
By analysing figure 5.5, it can be seen that higher uncertainties occur for lower values of RPM and that the higher the airspeed, the higher the efficiency values reached by the system. Since for lower RPM, with increasing airspeed, the values of thrust tend to be negative, the efficiency also decreases, reaching negative values for higher speeds. It is also possible to regard that the maximum efficiency is reached between 2500 RPM for the static case and 3700 RPM for maximum airspeed conditions. For higher values of RPM, the efficiency decreases. The maximum value of efficiency registered was 56.7% for the maximum airspeed. The graphics for the other systems are shown in figure A.8 in Appendix A.

The different values of airspeeds verified in the graphics obtained from the experimental tests showed in Appendix A are due to uncertainties of the airspeed sensor and due to the fact of these tests had been performed in different days, where the air density presented different values. It is also verified that for every experiments, the accuracy of the RPM for values below 1600 RPM is really low due to the accuracy of the RPM sensor.

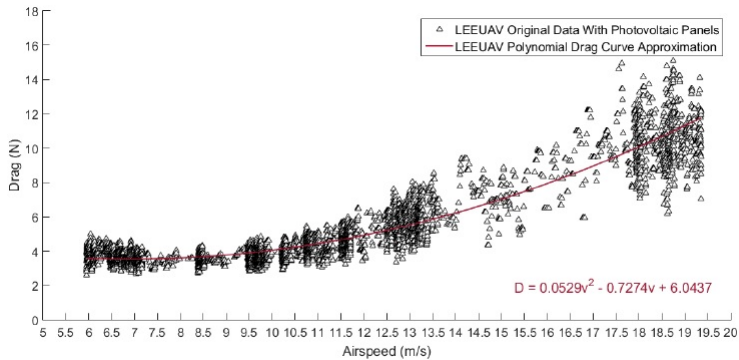
5.2 LEEUAV Case Study

After obtaining the experimental results for each parameter, it was analysed how it was possible to apply it to the case in study, the LEEUAV.

In [3], several flight tests were performed in cruise conditions, which is the stage of flight where the UAV spends more time. Knowing that in this stage, it was considered that $T = D$, one of the objectives of these tests was to determine the drag values for each flight velocity with and without the use of photovoltaic panels in the wings. The graphics obtained for these two conditions are shown in figure 5.6.



(a) LEEUAV without photovoltaic panels



(b) LEEUAV with photovoltaic panels

Figure 5.6: Drag vs airspeed for LEEUAV with and without photovoltaic panels [3]

By analysing figure 5.6, it is possible to note some differences in the drag values for the situation where the LEEUAV is equipped or not with photovoltaic panels. As such, the worst case scenario must be assumed which corresponds to the situation when the aircraft is equipped with the panels. From this graphic, the values of required thrust for each airspeed were determined.

Since the efficiency for each airspeed and thrust was determined in the experimental tests, it was possible to analyse the way the efficiency of a given system varies by applying the LEEUAV cruise flight conditions. This process was important since it was possible, before any optimization, to verify which system would be more efficient to apply in the LEEUAV. The parameters taken in account in this analysis were:

- Propeller diameter;
- Propeller pitch;
- Electric Motor;
- Input voltage.

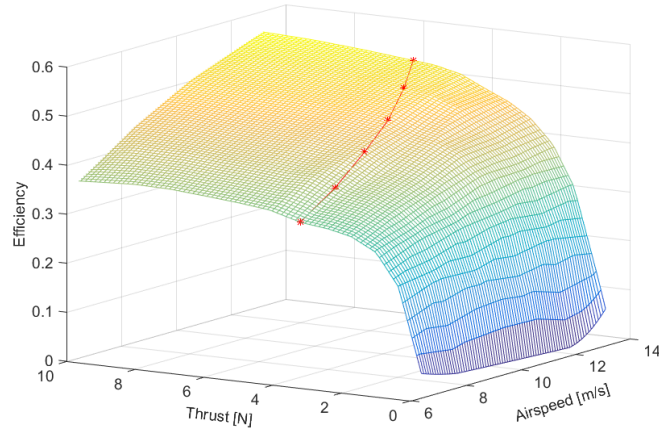
It is important to consider that this problem was analysed for a range of airspeeds between 6 m/s and 14 m/s, which allowed to reach, by analysing figure 5.6, a range of drag between 3 N and 6 N. To facilitate the analysis, this was performed for values of thrust between 0 and 10 N.

In table 5.1, the selection of systems chosen for the comparison of the efficiency distribution with the parameters referred above is shown.

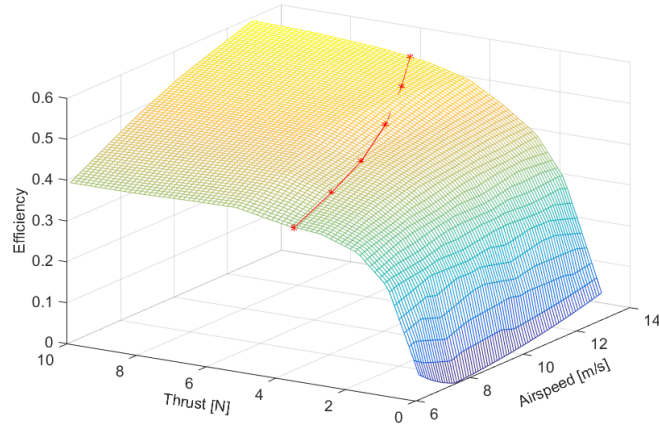
System	Diameter	Pitch	Motor	Input Voltage
OS-3810-1050 + APC 13"×8" for 12.5 V	—	—	X	—
OS-5020-490 + APC 13"×8" for 12.5 V	—	—	X	—
OS-5020-490 + APC 13"×8" for 16.5 V	X	—	—	—
OS-5020-490 + APC 16"×8" for 16.5 V	X	X	—	—
OS-5020-490 + APC 16"×10" for 16.5 V	—	X	—	X
OS-5020-490 + APC 16"×10" for 21.0 V	—	—	—	X

Table 5.1: Systems used in the variation of the efficiency distribution for each parameter

The results of the analysis for the comparison of the efficiency distribution with the variation of the propeller diameter are presented in figure 5.7.



(a) OS-5020-490 + APC 13"×8" for 16.5 V



(b) OS-5020-490 + APC 16"×8" for 16.5 V

Figure 5.7: Variation of propulsion efficiency with propeller diameter

Regarding figure 5.7, it is possible to visualize for each system, a three-dimensional surface corresponding to the data obtained from the wind tunnel tests, a contour intersecting the points with the data obtained at [3] and the corresponding interpolated efficiency. The graphics obtained to the other systems used on the comparison of the other three parameters are shown in figure A.9 to figure A.11 in Appendix A.

A bidimensional graphic, corresponding to the red contours shown previously, is shown in figure 5.8. This graphic allows an easier comparison between the several systems in order to analyse which would be the best to use on the LEEUAV, before any optimization.

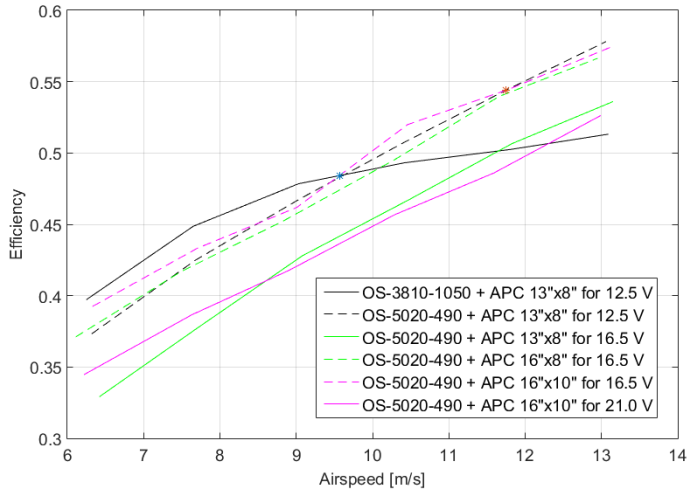


Figure 5.8: Comparison of the variation of efficiency with airspeed for all systems

In figure 5.8, it can be seen that for airspeeds between 6 m/s and 9.57 m/s , the most efficient system for the LEEUAV is the OS-3810-1050 + APC $13'' \times 8''$ for 12.5 V , until it reaches an efficiency of 48.4% . For airspeeds between 9.57 m/s and 11.75 m/s , the system OS-5020-490 + APC $16'' \times 10''$ for 16.5 V revealed to be the most efficient until it reaches an efficiency of 54.4% . For higher airspeeds, the system that revealed to be the most efficient was the OS-5020-490 + APC $13'' \times 8''$ for 12.5 V . So, it is possible to take some conclusions with the analysis of figure 5.8:

- The motor OS-3810-1050 is the most efficient for velocities below 9.57 m/s ;
- The higher the diameter, the higher the efficiency;
- The higher the pitch the higher efficiency;
- The higher the input voltage on a given motor+propeller system, the lower the efficiency.

Since the LEEUAV at cruise conditions travels at an airspeed of 7.53 m/s , the most efficient system to implement would be the OS-3810-1050 + APC $13'' \times 8''$ for 12.5 V .

Besides the efficiency, it was also analysed the variation of the thrust coefficient, C_T , and the power coefficient, C_P , with the advance ratio, J . In figure 5.9, the experimental results obtained for the variation of C_T with J and the literature results obtained from [4] are presented for comparison.

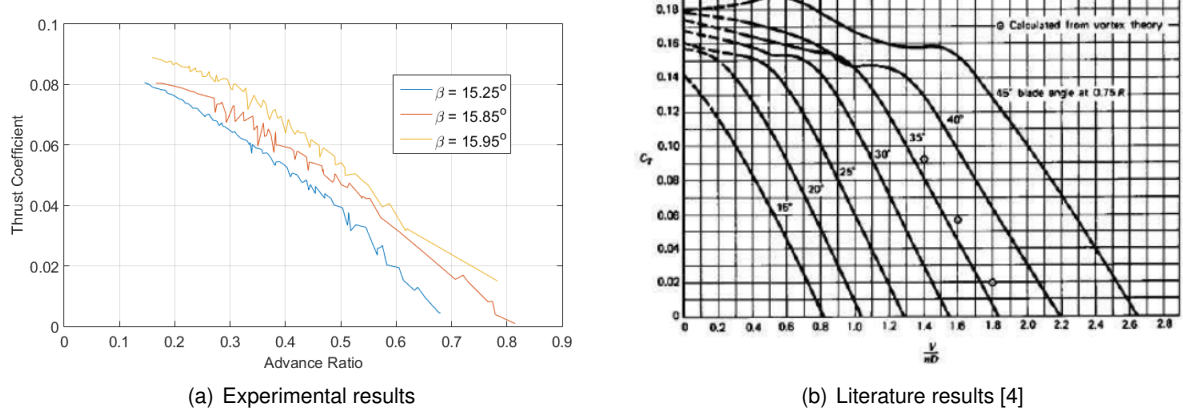


Figure 5.9: Variation of thrust coefficient with advance ratio

As it is shown in figure 5.9, in both graphics, the thrust coefficient decreases with the increase of the advance ratio. It is also noted that although the curves exhibit similar behaviour, the experimental values are lower relatively to the literature, which means that the calculated blade angles were higher than the real ones.

In figure 5.10, the experimental results obtained for the variation of C_P with J and the literature results obtained at [4] are presented.

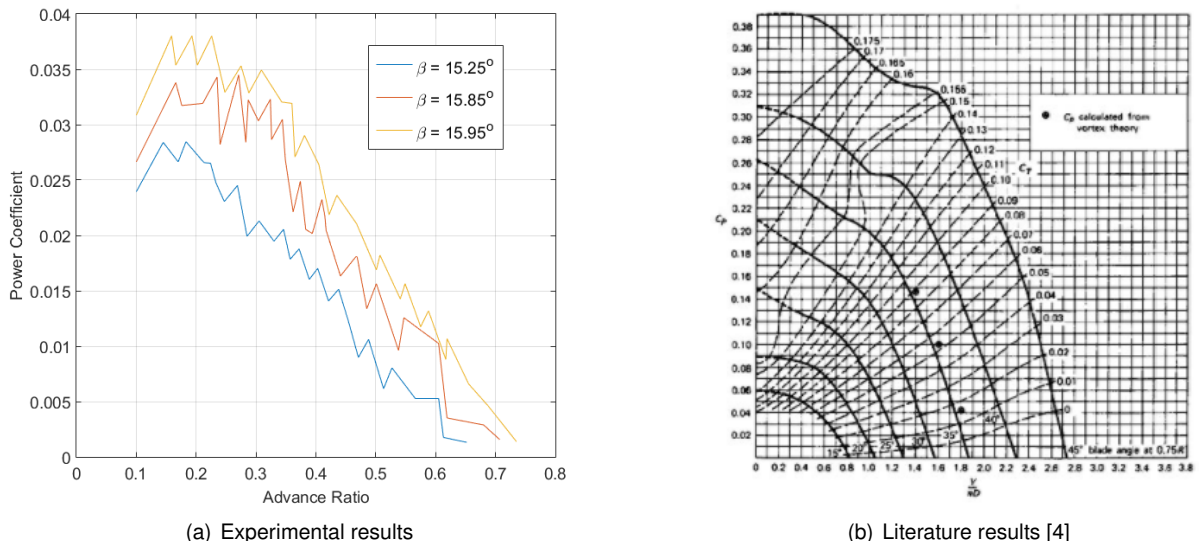


Figure 5.10: Variation of power coefficient with advance ratio

As it is shown in figure 5.10, in both graphics, the power coefficient decreases with the increase of the advance ratio. Similarly to the previous analysis, the experimental values are lower compared to the expected literature results, which is also explained for an overestimation of the blade angle of each propeller.

5.3 Verification and Validation

5.3.1 Analysis Framework

To obtain the simulations data, a routine in MATLAB[®] was built where the user defined the input parameters and then obtained the outputs. This routine was called "Analysis Framework" and it was defined this way for a question of simplicity. Its objective was to make the routine easier to understand and more practical to build the optimizer. The way the Analysis Framework was developed allowed the user to only insert the necessary input parameters and then to present the outputs, as schematically shown in figure 5.11.

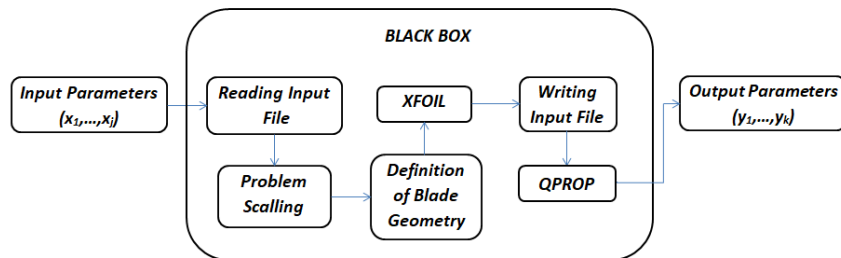


Figure 5.11: Analysis framework used to make the simulations

5.3.2 Validation Procedure

After obtaining the experimental results, it was possible to compute the numerical results using the software QPROP.

In this stage, it was necessary to consider that the power supply used during the experimental tests only provided values of voltage between 11.6 and 21.0 V, depending on the RPM values and the system in use. However, the software QPROP considers the use of a power supply that could provide any value of voltage. As such, to obtain credible results, instead the voltage and current, the output that was taken in consideration from the software at this stage was the electrical power. The other parameter that was being validated at this stage was the thrust.

The main purpose of this validation procedure was to assure that the numerical software results were the closest possible to the experimental results. It was important to assure an high level of accuracy due to the intention of using this numerical software later in the optimization process.

To validate the software, it was necessary to find a criteria of validation. In this case, the *Least Squares Fitting* method was used. This method is based on a mathematical procedure that finds the best-fitting curve to a given set of points by minimizing the sum of the squares of the offsets of the points from the curve. The sum of the squares of the offsets is used instead of the offset of the absolute values because this allows the residuals to be treated as a continuous differentiable quantity. However, due to the squares of the offsets being used, outlying points can have a disproportionate effect on the fit [32]. As such, the system was considered to be validated when the residual reached the lowest possible

positive value. The formula used to calculate the residual is given by

$$\text{Residual} = \sum (y_{exp} - y_{num})^2 . \quad (5.1)$$

In this validation procedure, two parameters were considered: β_{add} and the internal resistance of the motor, R . The β_{add} represents an offset inserted in the β distribution. This parameter was chosen due to be the one subjected to higher errors, since it was calculated using manual measurement as described in subsection 4.2.2 and it affects the numerical results of thrust. As such, this parameter was used to study the variation of the thrust residual in this procedure. The internal resistance of the motor affects the numerical results of electrical power consumed by the system and was used to study the the variation of the electrical power residual due to the fact of being the only motor parameter that could be modified.

The validation of the system OS-3810-1050 + 13"×8" was conducted at an airspeed of 7.65 m/s, for each airfoil. In figure 5.12, it is presented the variation of the thrust residual with β_{add} .

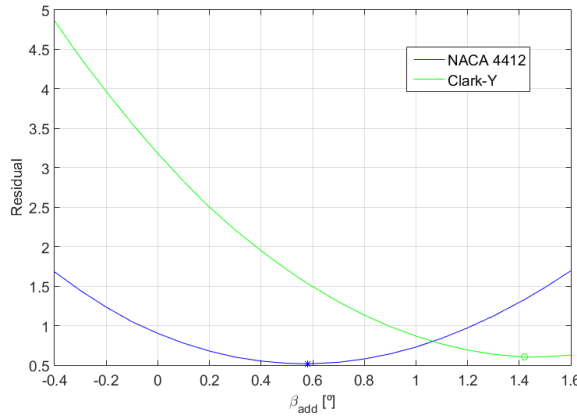


Figure 5.12: Residual variation with β_{add} for an APC 13"×8"

As shown in figure 5.12, the residual values obtained with equation (5.2) were analysed for different values of β_{add} . In table 5.2, the errors obtained with *Least Squares Fitting* method for the thrust, for each airfoil, are presented. The condition $\beta_{add} = 0^\circ$ corresponds to the software default value, since it represents the situation where no offset is inserted.

	Residual		
	$\beta_{add} = 0^\circ$	$\beta_{add} = 0.58^\circ$	$\beta_{add} = 1.42^\circ$
NACA 4412	0.90	0.52	1.33
Clark-Y	3.18	1.53	0.60

Table 5.2: Comparison between the errors of thrust for the different airfoils for the APC 13"×8"

As it can be analyzed in table 5.2, the lowest residual was obtained for the profile NACA 4412, with a value of $\beta_{add} = 0.58^\circ$. It is also noted that until the value of $\beta_{add} = 1.42^\circ$ was reached, the residual for the airfoil Clark-Y decreased, but it did not reach a value as lower as the one reached by the airfoil

NACA 4412. As such, it was possible to conclude that the airfoil used in this propeller was the NACA 4412. In figure 5.13, the experimental and numerical results for thrust validation are presented.

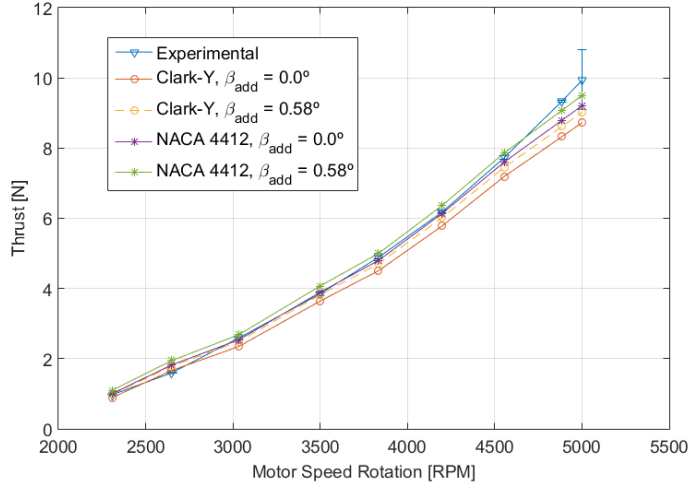


Figure 5.13: Thrust variation with RPM obtained for each airfoil for the APC 13"×8"

As it can be analysed in figure 5.13, as it was expected, the curve for the modified NACA 4412 is the one that fits better the curve of the experimental results. After the thrust validation, the electrical power was validated. To validate this output, it was necessary to change the internal resistance of the motor, as referred previously. In figure 5.14, the variation of the electrical power residual for different values of the motor internal resistance is presented.

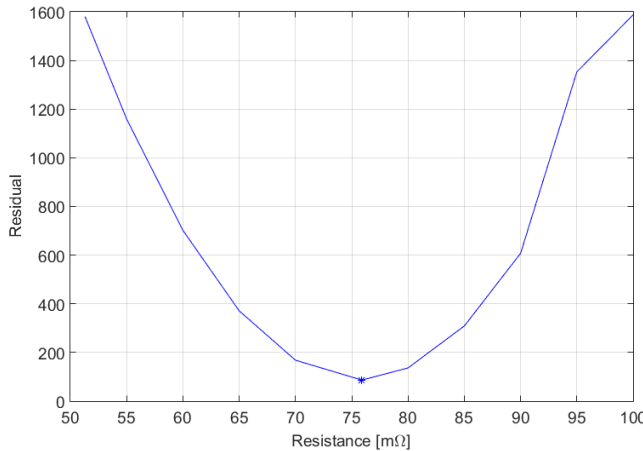


Figure 5.14: Residual variation with motor internal resistance for an OS-3810-1050

As shown in figure 5.14, only one analysis was performed. The main reason to this fact was that the airfoil was already validated. So, it was not necessary to analyse the variation of this residual for the Clark-Y airfoil. In table 5.3, the residuals obtained for the electrical power are presented. As referred in subsection 4.1, the value of motor internal resistance of $51.3\text{ m}\Omega$ was the software default value, since this was the value declared on the O.S datasheets for the OS-3810-1050.

Motor internal resistance [$m\Omega$]	Residual
51.3	1580.3
75.9	86.6

Table 5.3: Comparison between the errors of electrical power for the different resistances for the OS-3810-1050

As it can be analysed in table 5.3, the lowest residual value was obtained for a resistance of $75.9 m\Omega$. So, this resistance was the one that was used to validate the motor. The results from this validation are presented in figure 5.15.

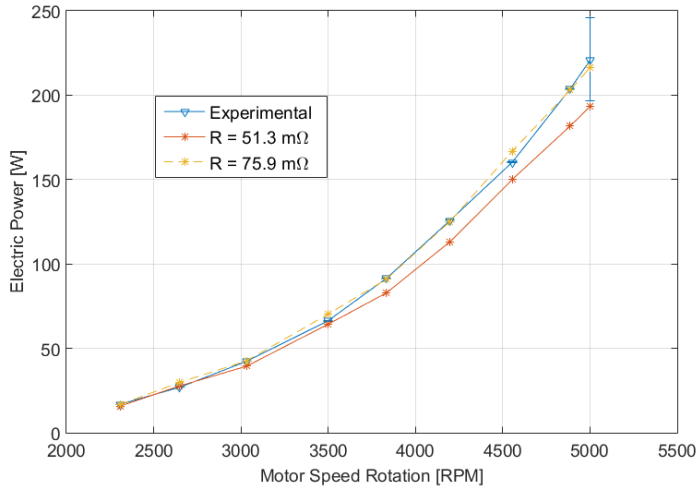


Figure 5.15: Electrical power variation with RPM obtained for different motor internal resistances for the OS-3810-1050

As shown in figure 5.15, the results between the experimental and the numerical results for each resistance were compared. It is possible to visualize that the modified curve with $R = 75.9 m\Omega$ fitted better the experimental results than the original one with $R = 51.3 m\Omega$. The new file corresponding to the validated propeller and motor is presented in figure A.14, in Appendix A.

Then, it was necessary to validate the other motor and the other different propellers that were tested. To validate the system OS-5020-490 + 16"×8", the same process was done. The validation was conducted at an airspeed of $7.49 m/s$, for each airfoil. The results for the variation of the residuals with β_{add} are presented in figure A.12, in Appendix A. In table 5.4, the residuals obtained for the thrust, for each airfoil, are presented.

β_{add}	Residual		
	$\beta_{add} = 0^\circ$	$\beta_{add} = -0.5^\circ$	$\beta_{add} = -1.21^\circ$
NACA 4412	5.90	2.33	0.30
Clark-Y	0.92	0.03	1.84

Table 5.4: Comparison between the errors of thrust for the different airfoils for an APC 16"×8"

As it can be analysed in table 5.4, the lowest residual was obtained for the airfoil Clark-Y with a value

of $\beta_{add} = -0.5^\circ$. It was also noted that with the variation of β_{add} , the residual for NACA 4412 decreased, however, it did not reach a residual value as lower as the one reached by the Clark-Y. As such, it was possible to conclude that the airfoil used in this propeller was Clark-Y. The graphical results for thrust validation is presented in figure A.12 in Appendix A.

After the thrust validation, the electrical power was validated. The results for the variation of the residuals with the motor internal resistance are presented in figure A.12 in Appendix A. In table 5.5, the residuals obtained for the electrical power, for the validated airfoil are presented. As referred in subsection 4.1, the value of motor internal resistance of $23 \text{ m}\Omega$ was the software default value, since this was the value declared on the O.S datasheets for the OS-5020-490.

Resistance [$\text{m}\Omega$]	Residual
23	2151.6
95	462.05

Table 5.5: Comparison between the errors of electrical power for the different resistances for the OS-5020-490

As it can be analysed in table 5.5, the motor internal resistance that minimized the residual using a Clark-Y airfoil was $R = 95 \text{ m}\Omega$. At this moment, the motor was not validated since it was unknown which resistance would fit better the system OS-5020-490 + 16"×10". The results of this validation are also presented in figure A.12.

Lastly, the validation of the system OS-5020-490 + 16"×10" was done. For this validation, an air-speed of 7.70 m/s was considered for each airfoil. The graphic with the results for residual variation with β_{add} is presented in figure A.13 in Appendix A. In table 5.6, the maximum errors obtained for thrust, for each airfoil are presented.

	Residual		
	$\beta_{add} = 0^\circ$	$\beta_{add} = -0.63^\circ$	$\beta_{add} = -1.07^\circ$
NACA 4412	1.05	0.10	0.58
Clark-Y	2.97	0.52	0.03

Table 5.6: Comparison between the errors of thrust for the different airfoils for an APC 16"×10"

As it can be analysed in table 5.6, the value of β_{add} that minimized the maximum error in the validation was -1.07° , for the airfoil Clark-Y. As such, it was possible to conclude that the airfoil used in this propeller was also the Clark-Y. The graphical results for thrust validation is presented in figure A.13 in Appendix A.

After the thrust validation, the electrical power was validated. The results of the variation of the residual with the motor internal resistance are presented in figure A.13. In table 5.7, the residuals obtained for the electrical power, for the validated airfoil are presented. In this case, the value determined in the previous validation of this motor is considered as software default value.

As it can be analysed in table 5.7, the value of resistance that minimized the residual in the validation was $R = 82 \text{ m}\Omega$. The results of this validation are also presented in figure A.13.

Resistance [$m\Omega$]	Residual
95	523.6
82	439.5

Table 5.7: Comparison between the errors of electrical power for the different motor internal resistances

Since this motor could only have one value for its internal resistance, for the motor validation, it was decided that the final resistance would result from an arithmetic average from the two optimum values obtained for each validated system,

$$R_{val} = \frac{95 + 82}{2} = 88.5 \text{ } m\Omega . \quad (5.2)$$

In table 5.8, the maximum errors obtained for the electrical power, for each system, using a resistance of $88.5 \text{ } m\Omega$ are presented.

Propeller	Residual
$16'' \times 8''$	475.8
$16'' \times 10''$	461.5

Table 5.8: Final comparison between the errors of electrical power for the different propellers for the OS-5020-490

By analysing table 5.8, it was seen that the residuals for each system increased, however, these were the minimum values of error that could be reached. The new files corresponding to the validated propellers and motor are presented in figures A.15 and A.16 in Appendix A.

To organize all the information presented in this subsection, tables 5.9 and 5.10 present a summary of all the important values obtained:

Propeller	Airfoil	β_{add} [°]
$13'' \times 8''$	NACA 4412	0.58
$16'' \times 8''$	Clark-Y	-0.5
$16'' \times 10''$	Clark-Y	-1.07

Table 5.9: Summary table with the validated characteristics for each propeller

Motor	Resistance [$m\Omega$]
OS-3810-1050	75.9
OS-5020-490	88.5

Table 5.10: Summary table with the validated internal resistance for each motor

In this chapter, a validation process was performed, using the *Least Squares Fitting* method to compare the residuals between the experimental and the numerical results. With this validation, the airfoils used in each propeller were determined and the propeller and motor input files were updated with the

new values of β_{add} and motor internal resistance, respectively. Since in the next chapter, an optimization of the system motor+propeller will be performed, this procedure was essential to assure the accuracy and realism of the numerical optimal results that are expected to be obtained.

Chapter 6

Propeller Optimization

In this chapter, the existing optimization methods will be described and a progressive optimization will be performed until reaching the final optimum propeller. The main goal of propeller optimization is to dimensioning a propeller with the capability of generate the amount of thrust necessary for each flight stage by consuming the lowest possible electrical power.

6.1 Problem Definition

6.1.1 Objective function and Design Variables

Before using any kind of optimization algorithm, it was necessary to define the problem and what was desired to be optimized. So the first step when thinking in optimization is to define an objective function.

An objective function, or fitness function, is a function that the optimizer analyses with the main goal of finding its minimum. The function should accept a vector, whose length is the number of independent variables of the problem itself and, depending on the optimizer in use and of what is desired, it can return a scalar or a row vector [33]. So, an objective function can be defined as

$$\begin{aligned} F : \mathbb{R}^j &\rightarrow \mathbb{R}^k, \text{ for } j, k \in \mathbb{N} \\ \vec{x} = (x_1, \dots, x_j) &\rightarrow F(\vec{x}) = (y_1, \dots, y_k) \end{aligned} \tag{6.1}$$

where \vec{x} is the vector of inputs (design variables) and \vec{y} is the vector of outputs (functions of interest). Sometimes, the maximum of the objective function is desired to be found. To find it, it is necessary to define a new objective function such as

$$G(\vec{x}) = -F(\vec{x}), \tag{6.2}$$

where the minimum of objective function $G(\vec{x})$ corresponds to the maximum of objective function $F(\vec{x})$ [34].

After analysing which were the parameters that would have a better impact on the propeller performance, it was decided that the objective of the optimization problem was to optimize the propeller

efficiency, (2.21).

However, at the beginning, the efficiency for each flight stage was desired to be optimized. As such, two different objective functions were created: η_{cruise} and η_{climb} which correspond to the propeller efficiency for cruise and climb condition, respectively. However, since it was not intended to generate two optimum propellers, in the final optimization, a final objective function was created, η_{total} , whose objective was to optimize η_{cruise} and η_{climb} simultaneously.

The second thing to be defined in an optimization process is the set of design variables \vec{x} . The design variables vector is presented in the form

$$\vec{x} = (x_1, \dots, x_j) \quad (6.3)$$

where x_j corresponds to each scalar independent variable.

6.1.2 Constraints and Bounds

It is important to distinguish between two main kinds of optimization: unconstrained optimization and constrained optimization. Usually, the unconstrained optimization is used when there are not any kind of constraints, so the optimizer finds the minimum of the function in all its domain. In this kind of optimization, it is possible to verify some convergence problems due to the fact of the existence of several local minima. To mitigate this problem, different initial guesses must be given to the optimizer to improve the accuracy of the results.

The constrained optimization is used when it is desired to find the optimum point in a certain defined domain and codomain. In this kind of optimization it is possible to distinguish between several types of constraints: linear inequality constraints, linear equality constraints, bound constraints and nonlinear constraints. By using linear inequality constraints, it allows the establishment of linear relations between the bounds of the several domain variables, which helps to ensure the accuracy of the results even if a nonsense initial guess is given to the optimizer. When this kind of constraints are used, it is not necessary to provide the function gradient, since solvers calculate it automatically. This type of constraint is presented in the form

$$[A]\{\vec{x}\} < \{\vec{b}\}, \quad (6.4)$$

where A has dimensions $j \times k$ and the vectors \vec{x} and \vec{b} have dimensions $j \times 1$. In this case, j is the number of linear constraints and k is the number of domain components covered in the constraint [35].

In relation to the linear equality constraints, the same criteria is applied. The only difference is that these constraints are presented in the form

$$[A_{eq}]\{\vec{x}\} = \{\vec{b}_{eq}\}. \quad (6.5)$$

Other type of constraints referred above in the topic list are the bound constraints. These constraints are the easiest to be set since these only limit the upper and the lower limits of the values of the components of \vec{x} [36]. If it is known the range of values where each component must be contained, it is only

necessary to build two vectors, one for each bound, as

$$\begin{aligned}\vec{l}b &= [x_{1_{lower}}, \dots, x_{j_{lower}}] \\ \vec{u}b &= [x_{1_{upper}}, \dots, x_{j_{upper}}].\end{aligned}\quad (6.6)$$

The last type of constraints are the nonlinear constraints. This type of constraints are often used when it is desired to constrain the objective function into determined regions of its domain. This type of constraints can also be used to constrain the outputs of the objective function. Contrary to the linear constraints, everytime that a nonlinear constraint is defined, the inequalities and the equalities must be clarified [37]. So, these constraints are presented in the form:

$$\begin{aligned}C(\vec{x}) &< 0 \\ C_{eq}(\vec{x}) &= 0.\end{aligned}\quad (6.7)$$

6.1.3 Methods Overview and Selection

In the optimization field, there are many available methods which can be divided in two main categories: deterministic and heuristic methods. In figure 6.1, it is possible to visualize a scheme where it is presented an overview of the methods:

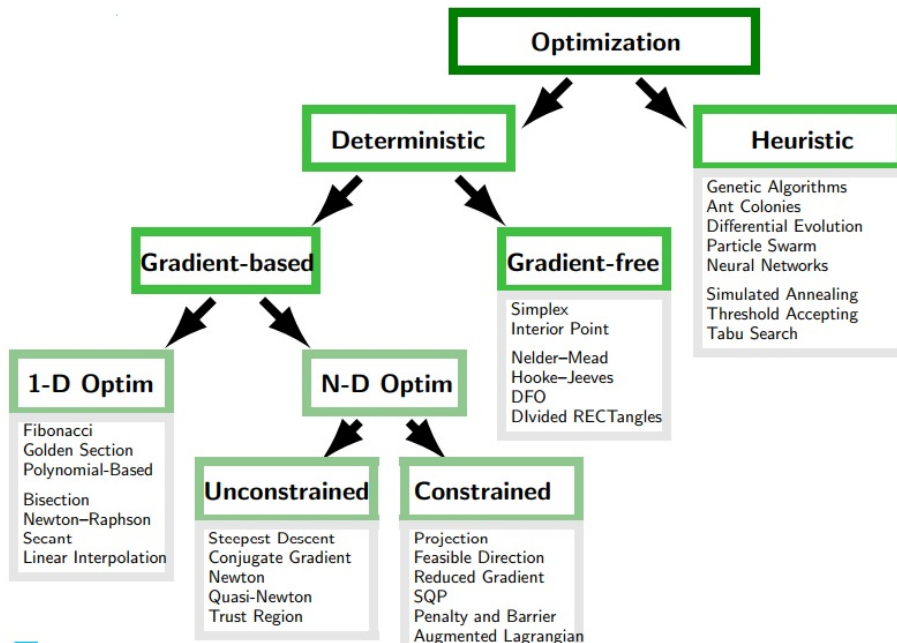


Figure 6.1: Overview of the different types of optimization methods [38]

The deterministic methods assume that the data for a given problem is known accurately. However, in many problems, the data can not be known accurately for several reasons such as the error measurement and the fact of some data representing information about the future, which it might not be possible to know with certainty [39]. There are two kinds of deterministic methods: the gradient-based and the gradient-free. Usually, when the functions have a smooth behaviour, the use of gradient-based methods is advisable, as the *SQP* method or the *Newton* method to improve the accuracy and the efficiency of

the optimization process. However, if the function is not considered to be smooth, it is more advisable to use gradient-free methods such as the *Hooke-Jeaves* method or the *Nelder-Mead* method [38].

The heuristic methods assume that there is an uncertainty incorporated into the model. The goal is to find a solution that is feasible for all data and optimal in some sense. Heuristic models take advantage of the fact that probability distributions governing the data are known or can be estimated. Some examples of this kind of methods are *Genetic Algorithms*, *Partical Swarm* and *Neural Networks* [38].

In this thesis, a deterministic gradient-based constrained method was pretended to be used, since the initial data was known accurately and as seen in the results of the wind tunnel tests, the studied parameters functions presented a smooth behaviour and due to the existence of bound and nonlinear constrains in all optimization problems that will be defined. As such, the *Interior-Point* method was selected to be used. This method was also selected due to handling large, sparse problems, as well as small dense problems [40].

6.1.4 Multi-objective optimization

A multi-objective optimization problem is an optimization problem that involves multiple objective functions. This type of problems has been applied in many fields of science, including engineering, where optimal decisions need to be taken in the presence of trade-offs between two or more conflicting objectives. This type of problem can be defined exactly like a single-objective optimization problem. In multi-objective optimization problems, there is not a single solution that simultaneously optimizes each objective. As such, the objective functions are considered to be conflicting, which means that there are an infinite number of pareto fronts for a given problem. A solution is called a pareto front if none of the objective functions can be improved without degrading some of the other objective values. In figure 6.2, an illustration of pareto front in a multi-objective problem is presented.

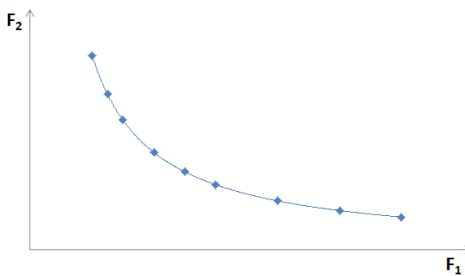


Figure 6.2: Multi-objective optimization pareto front distribution

As shown in figure 6.2, there are several possible solutions for a multi-objective problem. So, the main goal of this type of problems is to find the pareto-front that better suits the desired solution. To choose the desired pareto-front, there are several methods that can be used. One of the most used methods is the weighted aggregation method, which consists in converting a multi-objective problem into a single-objective problem. This is done by applying a linear function where the objectives are combined using weights, ϵ_k that specify the relative importance that each objective function has in the definition of the final solution, yielding

$$G_{opt} = \sum_{k=1}^K \epsilon_k G_k(\vec{x}), \quad (6.8)$$

where

$$\sum_{k=1}^K \epsilon_k = 1. \quad (6.9)$$

More information about the other methods that can be used to estimate the desired pareto front can be found in [41]. In the case of this thesis, it is desired to optimize the cruise efficiency and the climb efficiency, however, a propeller optimized for a given flight condition provides lower values of propeller efficiency for the other condition. As such, to build the final optimum propeller, it was necessary to use multi-objective optimization, where each objective function had a given associated weight.

6.2 Process Description

The system used as a starting point in this process was the OS-3810-1050 + APC 13"×8" with the NACA 4412 airfoil since this was the motor already installed in the LEEUAV. The optimization process was performed both for climb and cruise conditions. Since the optimization was done for these flight stages, the atmospheric conditions of the simulation were changed to the ones corresponding to maximum altitude conditions, that is, for an altitude of 1000 m. Using the models presented in [8], the new values for the atmospheric parameters are

$$\begin{aligned} c &= 336.4 \text{ m/s} \\ \mu &= 1.758 \times 10^{-5} \text{ kg/ms} \\ \rho &= 1.112 \text{ kg/m}^3. \end{aligned}$$

To solve the optimization problems, an algorithm was built in MATLAB[®] divided in three main parts:

- Analysis script;
- Nonlinear constraints script;
- Optimization script;

The analysis script receives and processes the input variables from the optimization script, runs the software QPROP and then exports the outputs obtained back to the optimization script. This script is responsible for evaluating the objective function.

The nonlinear constraints script works in a similar way as the analysis script, however, it constrains the exported values that are used in the optimization process.

The optimization script is where the inputs are defined and the outputs provided by the other two scripts handled to make the optimization possible. The command used in this script to make the optimization was the *fmincon*, using the *Interior-Point Algorithm*, as explained in subsection 6.1.3.

Because QPROP only exports discrete results, it was necessary to set a relative step size factor to define the initial step in finite differences approximations to the function gradients. To determinate the accuracy of each optimization process, a study to the variation of the derivative of each objective function in a given point in order to different design variables with the finite differences was performed. At the end, the chosen relative step size was the one that generates the inflection point in the derivative function. A flowchart describing the entire optimization process is presented in figure 6.3.

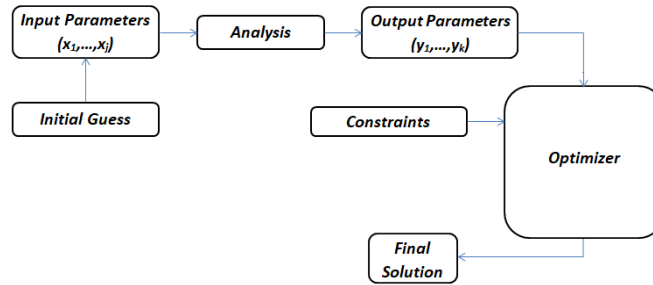


Figure 6.3: Optimization process scheme

6.3 Operating Conditions Optimization

Since it was pretended to study the propeller's performance in two different flight stages, two different problems were created. Initially, it was only intended to study how does the efficiency vary with the RPM, so, the objective function considered for the different flight stages was described by

$$\eta = F(RPM) . \quad (6.10)$$

For each problem, the bound constraints considered were

$$\begin{aligned} \vec{l}_b &= [3000] \\ \vec{u}_b &= [10000] . \end{aligned} \quad (6.11)$$

The value used as initial guess was 4000 RPM. It was important to notice that in the implementation, there was the necessity to scale the problem due to disparities in the order of magnitude between the values of the inputs and outputs. All the input values defined in the optimization script were delimited between 1 and 10. Only when the inputs are admitted in the analysis script, they are converted into the real values by using a scalar factor. As previously referred in section 1.2, a climb velocity of 7.67 m/s and a cruise velocity of 7.53 m/s were considered. After each problem being totally defined, the optimum

relative step size factor was determined to obtain accurate results from the optimization. The results of the derivative of the objective function calculated in the RPM value considered as initial guess, for each flight stage, obtained for each relative step size factor are displayed in figure A.17, in Appendix A. In figure A.18, in Appendix A, the evolution of the propeller efficiency η , thrust T and electrical power P, for both flight stages, is shown along the iterations during the optimization. The results of this optimization, for each flight stage, are presented in table 6.1.

Flight Stage	U [m/s]	RPM	T [N]	C_T	C_P	J	P [W]	η [%]
Climb	7.67	3003	2.683	0.0654	0.0425	0.4547	42.74	48.15
Cruise	7.53	3000	2.716	0.0644	0.0427	0.4469	42.87	47.7

Table 6.1: Results of the bounded constrained optimization

However, for the previous flight stages, there are main requirement that must be fulfilled. By using the formula that relates drag with airspeed presented in figure 5.6, it was possible to verify that for a cruise airspeed of 7.53 m/s, a value of 3.57 N was obtained. Since the thrust value is equal to drag in cruise conditions, this means that the condition that must be verified now is $T \geq 3.57N$. Consequently, to assure that this requirement was fulfilled, it was necessary to apply a nonlinear constraint in the form:

$$C = 3.57 - T \quad (6.12)$$

$$C_{eq} = [] .$$

For climb conditions, it was necessary to take in account the ratio $\frac{T}{W}$ for this stage. From the data presented for the LEEUAV [3], using the method in [42] for climb conditions, a ratio of $\frac{T}{W} = 0.26$ was obtained. Knowing that the aircraft Maximum Take-Off Weight (MTOW) was 53.4 N, it was obtained that the thrust necessary to perform this flight stage was 13.88 N. Therefore, to assure that this requirement was fulfilled, it was necessary to apply a nonlinear constrain in the form:

$$C = 13.88 - T \quad (6.13)$$

$$C_{eq} = [] .$$

The results of the derivative of the objective function calculated in the RPM value considered as initial guess, for each flight stage, obtained for each relative step size factor are displayed in figure A.17, in Appendix A. In figure A.19, in Appendix A, it is shown the evolution of the propeller efficiency, thrust and electrical power, for both flight stages, along the optimization iterations. The results of the optimization after applying this constraint are presented in table 6.2.

Flight Stage	U [m/s]	RPM	T [N]	C_T	C_P	J	P [W]	η [%]
Climb	7.67	5934	13.88	0.0867	0.0433	0.2301	375.2	28.38
Cruise	7.53	3317	3.57	0.0714	0.0435	0.4042	59.36	45.28

Table 6.2: Results of the thrust constrained optimization

By analysing table 6.2, it is possible to notice that the system can perform cruise conditions without

any difficulties. For an input voltage of 12.5 V, it was only possible to obtain a maximum current of 30 A to perform in total secure conditions. As such, it was decided to limit the maximum electrical power of the motor to the corresponding 375 W. The electrical power consumed at climb is slightly above this limit. The reached limit is still acceptable, however, it should be as minimized as possible.

6.4 Propeller Geometry Optimization

In the previous section, it was proved that the system was capable to fulfil the thrust requirements for cruise, but not for climb. However, the only parameter that was used in the previous optimization process was the RPM and there are other design variables that can be optimized, such as those that define the propeller geometry, to increase the propeller efficiency η , by reducing the consumed electrical power P .

The first design variables taken in account are the geometric pitch angle distribution $\beta(r)$ and the chord distribution $c(r)$. It is important to notice that the values of $\beta(r)$ are in degrees. In order to optimize these distributions, four equidistant points along the radius of the propeller blade, including the hub and the tip, were selected using a cubic spline method, as illustrated in figure 6.4.

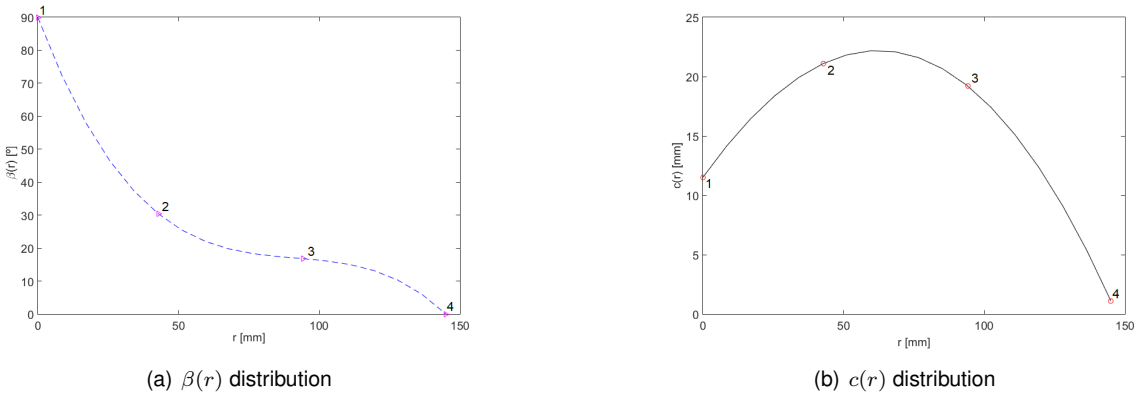


Figure 6.4: Illustration of cubic spline method

As seen in figure 6.4a), the four equidistant points used to build the cubic spline for $\beta(r)$ distribution are represented and can be defined as $\beta_1, \beta_2, \beta_3$ and β_4 according with the index denoted in the figure. In figure 6.4b), the four equidistant points used to build the cubic spline for $c(r)$ distribution are represented and can be defined as c_1, c_2, c_3 and c_4 according with the index denoted in the figure. For each iteration performed by the optimizer, a different distribution for each parameter is calculated until the optimizer finds which distribution for each parameter provides the best value for the propeller efficiency. The other geometric design variable taken in account by the optimizer is the radius of the propeller, R . To build this new problem, it is necessary to define two objective functions, one for each flight stage, described by

$$\begin{aligned}\eta_{cruise} &= F(\beta_1, \beta_2, \beta_3, \beta_4, c_1, c_2, c_3, c_4, R, RPM_{cruise}) \\ \eta_{climb} &= F(\beta_1, \beta_2, \beta_3, \beta_4, c_1, c_2, c_3, c_4, R, RPM_{climb}) .\end{aligned}\quad (6.14)$$

In the previous equations system, RPM_{cruise} corresponds to the RPM for cruise conditions and RPM_{climb} corresponds to the RPM for climb conditions. Like in the previous optimizations, it was nec-

essary to define the bound constraints. The bound constraints applied for the cruise problem were:

$$\begin{aligned}\vec{l}b_{cruise} &= [88, 26, 16, 0, 10, 20, 19, 1, 145, 3620] \\ \vec{u}b_{cruise} &= [90, 34, 19, 1, 12, 28, 24, 2, 184, 6000] .\end{aligned}\quad (6.15)$$

The bound constraints applied for the climb problem were:

$$\begin{aligned}\vec{l}b_{climb} &= [85, 25, 14.5, 0, 10, 20, 19, 1, 145, 6350] \\ \vec{u}b_{climb} &= [90, 34, 19, 1, 14, 28, 24, 2.1, 184, 10000] .\end{aligned}\quad (6.16)$$

The initial guesses, in this case, for each problem were:

$$\begin{aligned}\vec{x}_0_{cruise} &= (90, 33, 18, 0.9, 11, 27, 23, 1.9, 150, 4000) \\ \vec{x}_0_{climb} &= (90, 26, 16, 0.6, 11, 22, 20, 1.9, 150, 6500) .\end{aligned}\quad (6.17)$$

As it happened in the previous optimizations, these problems were also scaled. After the problem being totally defined, as previously performed, the optimum relative step size factor for each objective problem was determined to obtain accurate results from the optimization. While in the previous problems, the derivative of the objective function was only determined using the RPM as design variable, in this optimization problem this study was performed using the design variables RPM, c_2 , β_3 and R . The variables c_2 and β_3 were selected because they represent values of chord and pitch angle of sections that are not placed at the hub neither at the tip of the propeller blades. The results of the derivative of the objective function calculated in the design variables values considered as initial guess, for each flight stage, obtained for each relative step size factor are displayed in figure A.17. In figure A.20 in Appendix A, it is shown the evolution of the propeller efficiency, thrust and electrical power, for both flight stages, along the iterations. After performing the optimization of each problem, it was determined that the optimum blade radius, R , for cruise conditions was 145.11 mm and for climb conditions was 146.65 mm, which correspond to the lower bound defined for this design variable. In figure 6.5, it is possible to visualize the comparison of $c(r)$ and $\beta(r)$ distributions between the initial and the optimum propellers, for each flight stage.

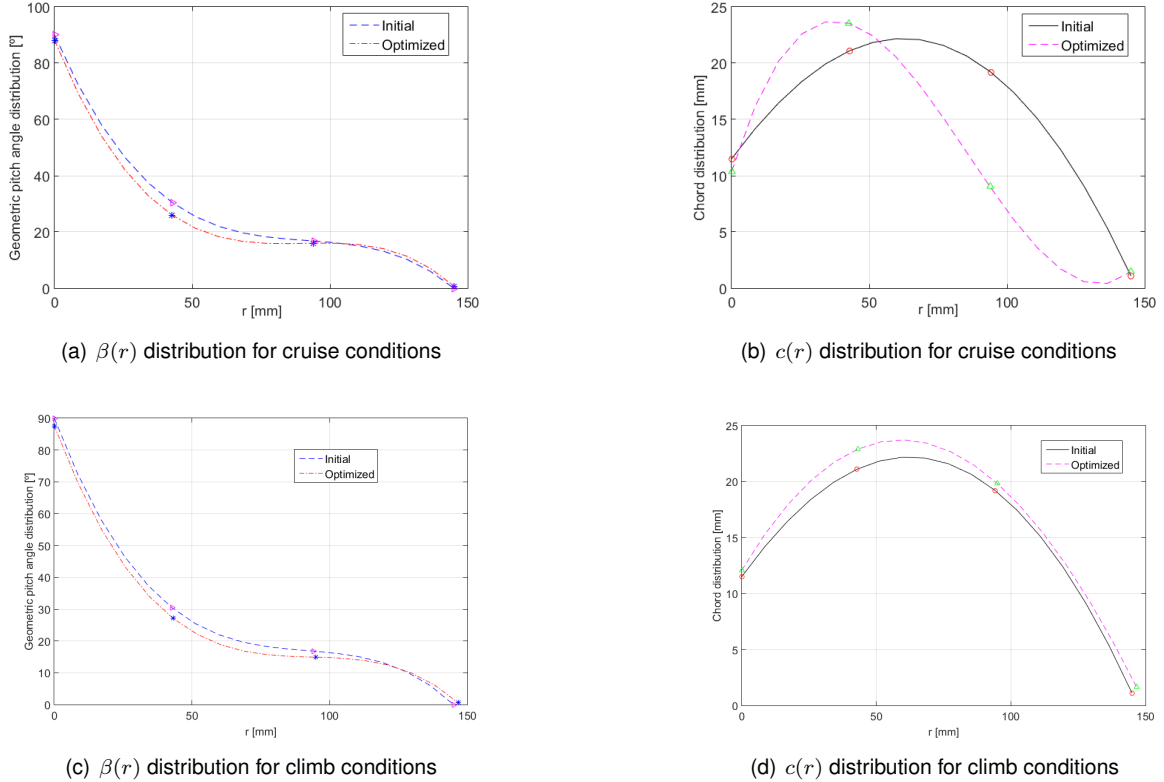


Figure 6.5: Geometric pitch angle and chord distributions of the propellers blades designed for cruise and climb conditions, before and after an optimization process

The results of these optimizations are presented in table 6.3.

Flight Stage	$U [m/s]$	RPM	$T [N]$	C_T	C_P	J	$P [W]$	$\eta [\%]$
Climb	7.67	6348	13.88	0.0725	0.0329	0.2151	348.1	30.42
Cruise	7.53	3665	3.571	0.0584	0.0332	0.3658	59.21	45.42

Table 6.3: Results of the initial propeller geometry optimization

By analysing table 6.3, an increase in the propeller efficiency for each problem was obtained. As expected, by changing the geometry of the blades, it was possible to reduce the consumed electrical power, which resulted in an increased efficiency. However, the results presented in this table correspond to two different propellers and the objective was to find a single optimized propeller. Therefore, a multi-objective optimization with the weighted aggregation method described in section 6.4 was used. In this case, it was decided to define the weight ϵ as

$$\epsilon = \frac{E_{cruise}}{E_{cruise} + E_{climb}}, \quad (6.18)$$

where E_{cruise} is the total energy spent by the UAV during the cruise flight and E_{climb} is total energy spent by the UAV during the climb. According to [43], the required energy during climb is 266.9 kJ and the required energy during cruise is 1370.9 kJ, which means that $\epsilon = 0.837$. As such, it was possible to

build a new objective problem as

$$\eta_{total} = F(\beta_1, \beta_2, \beta_3, \beta_4, c_1, c_2, c_3, c_4, R, RPM_{cruise}, RPM_{climb}) . \quad (6.19)$$

However, this new problem has a new particular condition. In this case, the variable η_{total} was defined as

$$\eta_{total} = \epsilon\eta_{cruise} + (1 - \epsilon)\eta_{climb} = 0.837\eta_{cruise} + 0.163\eta_{climb} \quad (6.20)$$

The bound constraints applied in this optimization were

$$\begin{aligned} \vec{l}b_{total} &= [87, 22, 13, 0, 6, 22, 12, 1, 145, 3500, 6200] \\ \vec{u}b_{total} &= [90, 24, 15, 0.5, 9, 25, 15, 2.1, 184, 3700, 6400] \end{aligned} \quad (6.21)$$

and initial guess considered was

$$\vec{x}_{0_{total}} = (90, 23, 14, 0.3, 7, 24, 13, 1.2, 150, 3550, 6250) . \quad (6.22)$$

As it happened in the previous optimizations, this problem was also scaled. The optimum relative step size factor for each objective problem was also determined as displayed in figure A.17. The only difference in this optimization problem is that the study was performed for the variables RPM_{cruise} and RPM_{climb} instead of variable RPM. In figure A.21, at Appendix A, it is shown the evolution of the propeller efficiency, thrust and electrical power, for both flight stages, along the iterations. In this figure, the total efficiency of the flight η_{total} is also shown, along the iterations. After performing the optimization of each problem, it was determined that the optimum blade radius, R , was 168.52 mm. In figure 6.6, it is possible to visualize the $c(r)$ and $\beta(r)$ distributions comparison between the initial and the optimum propeller.

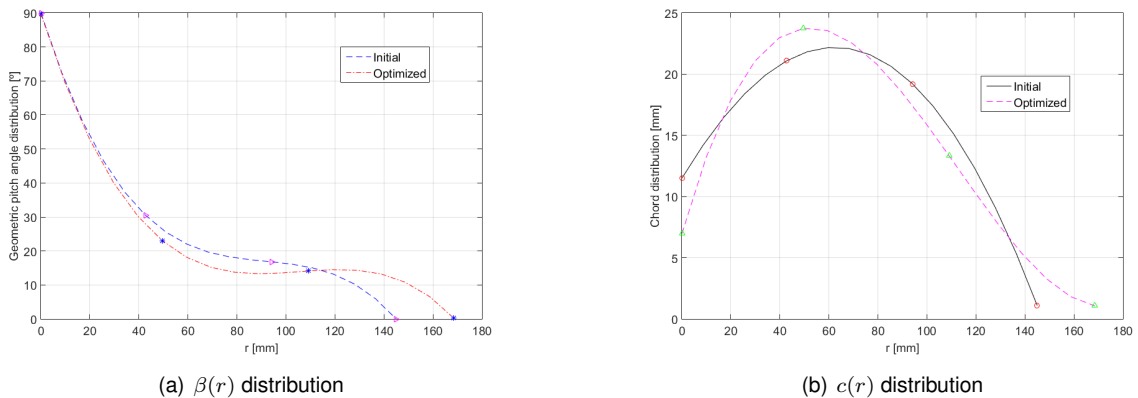


Figure 6.6: Geometric pitch angle and chord distributions of the final propellers' blades before and after the optimization

The results of these optimization are presented in table 6.4.

Flight Stage	U [m/s]	RPM	T [N]	C_T	C_P	J	P [W]	$\eta[\%]$
Climb	7.67	6270	13.88	0.0462	0.0185	0.218	344.1	30.94
Cruise	7.53	3610	3.57	0.036	0.018	0.371	58.77	45.76

Table 6.4: Results of the final propeller geometry optimization

By analysing table 6.4, it is possible to notice a slight increase in both the climb and cruise efficiency, due to the change of the boundaries of the problem. At the end, a total efficiency of the flight $\eta_{total} = 43.34\%$ was obtained.

6.5 3D Optimal Design

After the optimization process being complete, a new propeller file was obtained with the detailed geometry distribution parameters. The following phase was to find a way to design a tridimensional model of the blades of the optimized propeller. Initially, it was necessary to make a file for each point presented in the geometry description of the propeller file. Each file contains the points coordinates of the profile NACA 4412 for each section. The coordinates of the points for a n-section are calculated according to

$$\begin{bmatrix} \vec{x}_k^* \\ \vec{y}_k^* \end{bmatrix} = c_k \times \begin{bmatrix} \cos \beta_k & \sin \beta \\ -\sin \beta_k & \cos \beta_k \end{bmatrix} \times \begin{bmatrix} \vec{x}_k \\ \vec{y}_k \end{bmatrix} \quad (6.23)$$

where \vec{x}_k and \vec{y}_k are the vectors of coordinates of the original profile, \vec{x}_k^* and \vec{y}_k^* are the new coordinates of the profile for each section of the blade and c_k is the chord value for each section. It is important to notice that the transformation matrix on the previous expression causes a clockwise rotation, which makes easier the projection of the blades.

After having all the files with the rotated coordinates for each section, these files were independently imported to SOLIDWORKS®. When importing data of the files, SOLIDWORKS® automatically matches all the points. Since the airfoil points are disposed in the plane, it was necessary to match them using a spline. After all airfoils being totally defined, a three-dimensional loft was applied and the final 3D shape of each blade that constitutes the propeller was obtained. In figure 6.7, the three-dimensional models, for rotated views, of the blade of the initial and final optimized propeller are presented.

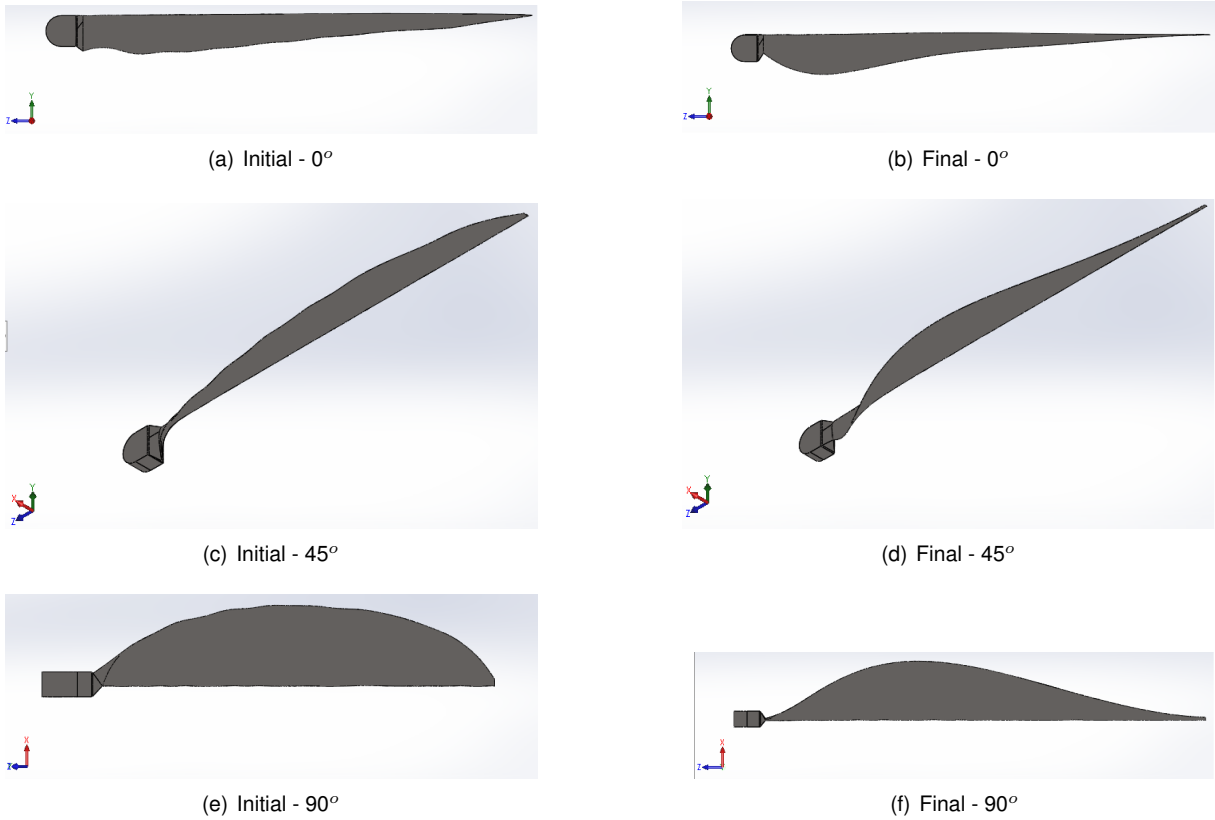


Figure 6.7: Comparison of the three-dimensional models, for rotated views, of the blade of the initial and final optimized propeller

At the end of this chapter, it is possible to compare the results between the performance of the initial propeller and the final propeller. The results of each propeller are presented in table 6.5.

Flight Stage	U [m/s]	RPM	T [N]	C_T	C_P	J	P [W]	η [%]
Climb - initial	7.67	5934	13.88	0.0867	0.0433	0.2301	375.2	28.38
Climb - final	7.67	6270	13.88	0.0462	0.0185	0.218	344.1	30.94
Cruise - initial	7.53	3317	3.57	0.0714	0.0435	0.4042	59.36	45.28
Cruise - final	7.53	3610	3.57	0.036	0.018	0.371	58.77	45.76

Table 6.5: Comparison of the results obtained for the initial and the final propeller

As it can be analysed in table 6.5, there is an improvement in the performance with the optimization process. With the optimization process, a significant reduction in the thrust and power coefficients due to the increase on the rotation velocity of the motor and the propeller diameter is verified. A reduction of the electrical power consumed, mainly for climbing conditions, is also verified which caused the increasing on the propeller efficiency for both flight stages. After this optimization, a value of 244.8 kJ is obtained for climb conditions and a value of 1356.52 kJ is obtained for cruise conditions, which results in an increasing of 9 minutes of flight time. After modelling the blade, one blade was printed in PLA with a filament diameter of 0.4 mm, using a 3D-printer. The physical model of the optimized blades can be visualized in figure 6.8.



(a) Front view



(b) Side view



(c) Rear view

Figure 6.8: Rotated views of the physical three-dimensional model

It is important to notice that due to the fact of the planform shape of the blade being too thin, it was not possible to print an accurate model. As such, an offset was added to the longitudinal component of the airfoil to allow the printing of the visual physical model.

Chapter 7

Conclusions

The main objective of this thesis was to optimize the propulsion system of the LEEUAV.

To perform the optimization system analysis, it was necessary to select a software to do it. There were several options, but the best choice was QPROP, since it was the only one that considers the characteristics of the complete system, and not only the characteristics of the propeller. Another factor that influenced the decision was that it was the only available software that allowed both an initial analysis and a posterior use in the optimization process.

Since it was pretended to optimize the propeller efficiency by reducing the electrical power consumed by the system, it was concluded that the best option was to define this parameter as the ratio between the power that a propeller can use and the electrical power supplied to the system.

To perform the numerical simulations, it was necessary initially to determine the airfoils aerodynamic characteristics and to measure the external shape of the blades. To determine the airfoil characteristics, the software XFOIL was used considering $Re = 100000$, since this value would be a good approximation for the tested cases. Due to the fact of not knowing which airfoil each propeller had, two different airfoils were considered, the Clark-Y and the NACA 4412. To perform the measurements of the planform shape of the blades, two methods were used. The first method consisted in splitting the blades in several sections, and to measure them manually, using a calliper. The second method consisted in using a 3D scan to determine the propeller geometry. However, contrary to the expected, the accuracy of the results obtained with the 3D scan method was very low. As such, the results provided from the manual measurements were taken in consideration.

In this thesis, some experimental tests were also performed using a wind tunnel, that must be calibrated when there is a change in the medium temperature of the place where it is located due to the variation of the dynamic pressure. To perform the tests, a force balance previously built was used. However, the motor support system had to be changed since the previous one was oversized, which could lead to additional drag that could affect the experiments. In spite of the creation of the new support system, several runs at the tunnel were performed each day before any experimental tests to help reducing possible errors that could exist.

Since the software QPROP also takes in account the electrical motor parameters, by performing the

experimental tests, it was concluded that motors with a lower constant K_v are able to support higher values of input voltage and electrical power, which was reflected the fact that the motor with the higher K_v was only used to test the propellers with a smaller diameter. After performing the experimental tests and applying the gathered data to the specific case of the LEEUAV, it was concluded that the use of the motor OS-3810-1050 was more efficient for airspeeds below 9.57 m/s ; the higher the diameter and the pitch of a propeller, the higher the efficiency and that the efficiency decreases with the increase of the input voltage. It was also concluded that the geometric pitch angle distribution obtained from the manual measuring was overestimated in the three tested propellers.

After performing the experimental tests, the numerical tests were performed to validate each motor and each propeller models. To validate the propellers, the parameter β_{add} was used since this was the parameter most sensible to uncertainties. To validate the motor, the internal resistance was used as a parameter. Since the motor OS-5020-490 was validated in two different tests, at the end, it was considered that the final resistance for this motor would result from an arithmetic average between the two values of resistances obtained in each test.

After the validation was performed, the optimization process was progressively done. Initially, only single objective optimizations were performed, for each flight condition, where the only input parameter was the RPM. However, it was verified that for the climb condition, the required electrical power for the motor was higher than the maximum electrical power supported by the motor to work safely. As such, it was decided to perform single-objective optimizations where the geometric shape of the propeller could be modified. At the end of these optimizations, higher values for the propeller efficiency were obtained, which was reflected on a decrease of electrical power of each flight stage. Contrary to what was expected, the best efficiency in both cases was obtained for the smaller allowed propeller diameter.

However, since the objective of this dissertation was to produce a single propeller, it was necessary to perform a multi-objective problem optimization, where a single propeller was optimized for both flight conditions simultaneously. To perform this optimization, the weighted aggregation method was used, where the weights were determined according to the energy spent in each flight stage. Contrary to what was expected, the efficiency reached with this optimization was higher for both flight conditions by comparing with the previous ones. This might be explained by the fact of the bound constraints defined in this problem being different comparatively to the other optimization problems. At the end, the new blade was projected using the software SOLIDWORKS® and a physical model was printed using the rapid prototyping method.

7.1 Achievements

The major achievements of this dissertation were:

- Characterization of two different airfoils, the Clark-Y and the NACA 4412, whose data can be used in any propeller performance analysis;
- Study of the influence of the variation of the diameter, chord distribution and geometric pitch angle

distribution in the propeller's performance;

- Validation of the motor models described in this dissertation, which allowed the analysis of the performance of a given system using each motor;
- Validation of three propeller models described in this dissertation;
- LEEUAV performance analysis by simulating the use of each system;
- Computational program that performs a multi-operation point (climb and cruise conditions) optimization of the external shape of a propeller.

7.2 Future Work

As it was referred in this dissertation, a blade measuring using a 3D scanning method was performed. However, as it was presented, the accuracy of the results was less than expected. Therefore, as a future work, it is recommended to perform a blade measuring using a system with a higher accuracy to obtain more accurate measures than the ones obtained with the manual measuring used here.

Another fact that can be noticed is that it was only optimized the external geometry of the propeller used in the propulsion system for the LEEUAV. As a future work, it would be recommended to make the optimization of the airfoil shape in order to build a propeller even more optimized than the one built in this dissertation.

Lastly, to print the blades of the optimized propeller it was used the rapid prototyping method. However, this method might not be the most accurate. As so, it is recommended as a future work, to manufacture the blades using the mold construction blade. Using this method will allow to experimentally test the new propeller in the wind tunnel to validate the optimization results obtained by the numerical model.

Bibliography

- [1] M. Borges. Design of an Apparatus for Wind Tunnel Tests of Electric UAV Propulsion Systems. Master's thesis, Instituto Superior Técnico, June 2015. https://fenix.tecnico.ulisboa.pt/downloadFile/282093452007371/MiguelBorges_Thesis.pdf.
- [2] L. M. A. Parada. Conceptual and Preliminary Design of a Long endurance Electric UAV. Master's thesis, Instituto Superior Técnico, Nov. 2016. https://fenix.tecnico.ulisboa.pt/downloadFile/1970943312279038/LuisParada_Thesis.pdf.
- [3] A. Rodrigues. Airframe Assembly, Systems Integration and Flight Testing of a Long Endurance Electric UAV. Master's thesis, Universidade da Beira Interior, Feb. 2017.
- [4] B. W. McCormick. *Aerodynamics Aeronautics and Flight Mechanics*. Pennsylvania State University, 2nd edition, Apr. 1995. ISBN:0-471-5706-2.
- [5] Z. S. Spakovszki. *16.Unified: Thermodynamics and Propulsion*. D.Quattrochi, 2006. <http://web.mit.edu/16.unified/www/FALL/thermodynamics/notes/notes.html>.
- [6] J. D. Anderson. *Fundamentals of Aerodynamics*. McGraw-Hill, 2nd edition, Dec. 1991. ISBN:0-07-001679-8.
- [7] J. Katz and A. Plotkin. *Low-Speed Aerodynamics*. Cambridge University Press, 2nd edition, Dec. 2003. ISBN:0-521-66219-2.
- [8] J. Roskam. *Airplane Aerodynamics and Performace*. DARcorporation, 1st edition, 1997. ISBN: 1-884885-44-6.
- [9] M. Drela. QPROP formulation. http://web.mit.edu/drela/Public/web/qprop/qprop_theory.pdf, June 2006.
- [10] M. El-Samanoudy, A. A. E. Ghorab, and S. Z. Youssef. Effect of some design parameters on the performance of a Giromill vertical axis wind turbine. *Ain Shams Engineering Journal*, 1(1):85–95, Sept. 2010. doi:10.1016/j.asej.2010.09.012.
- [11] The Propulsion Group. Propeller Performance Sample Plots, Jan. 1997. http://aero.stanford.edu/aa292/propulsion/prop_plots.html accessed on Dec 2017.

- [12] A. Berg. AKPD/AKPA. https://www.sintef.no/globalassets/upload/marintek/pdf-filer/software/akpd-akpa_programpackage.pdf accessed on Mar 2017.
- [13] M. Hepperle. JavaProp - Users Guide. <http://www.mh-aerotools.de/airfoils/javaprop.htm> accessed on Mar 2017., .
- [14] M. Drela. QPROP User Guide. http://web.mit.edu/drela/Public/web/qprop/qprop_doc.txt, July 2007.
- [15] E. Larabee. *Practical Design of Minimum Induced Loss Propellers*. SAE Preprint 790585, 1979. doi:10.4271/790585.
- [16] M. Drela. XFOIL Subsonic Airfoil Development System. <http://web.mit.edu/drela/Public/web/xfoil/>, Dec. 2013.
- [17] M. Bronz, J.-M. Moschetta, and G. Hattenberger. Multi-Point Optimisation of a Propulsion Set as Applied to a Multi-Tasking MAV. HAL, July 2012. <https://hal-enac.archives-ouvertes.fr/hal-00993461>.
- [18] O.S. Engine. <https://www.osengines.com/> accessed on Feb 2018.
- [19] Propeller Parts Market. <http://propellerpartsmarket.com/d-4798-1p-hartzell-spinner-assembly> accessed on Feb 2018.
- [20] E.A.I. Spinners and Props. <https://www.experimentalaircraft.info/articles/aircraft-spinner-propeller.php> accessed on Jun 2017.
- [21] S. Santos, B. Soares, M. Leite, and J. Jacinto. Design and development of a customised knee positioning orthosis using low cost 3D printers. *Virtual and Physical Prototyping*, Mar. 2017. doi: 10.1080/17452759.2017.1350552.
- [22] APC Propellers. <https://www.apcprop.com/Articles.asp?ID=262#airfoil> accessed on May 2017.
- [23] U. of Illinois. UIUC Applied Aerodynamics Group, 2017. http://m-selig.ae.illinois.edu/ads/coord_database.html accessed on May 2017.
- [24] M. Drela. DC Motor / Propeller Matching, Mar. 2005. <http://web.mit.edu/drela/Public/web/qprop/motorprop.pdf>.
- [25] A. Fonseca. Medição de parâmetros do Tunel Aeroacústico (TAA), Mar. 2012.
- [26] R. G. Budynas and J. K. Nisbett. *Shigley's Mechanical Engineering Design*. McGraw-Hill Education, 10th edition, 2015. ISBN:978-981-4595-28-5.
- [27] V. Intertechnology. <http://www.vishay.com/> accessed on Jun 2017.
- [28] P. innovative electronics. <http://www.pitlab.com/> accessed on Jun 2017.

- [29] A. Devices. <http://www.analog.com/> accessed on Jun 2017.
- [30] *MPXV7002 Integrated Silicon Pressure Sensor On-Chip Signal Conditioned, Temperature Compensated and Calibrated.* NXP, Mar. 2017. <https://www.mouser.com/ds/2/302/MPXV7002-1127332.pdf>.
- [31] M. Hepperle. Static Thrust of Propellers. <http://www.mh-aerotools.de/airfoils/prpstati.htm> accessed on Oct 2017., .
- [32] P. R. Bevington. *Data Reduction and Error Analysis for the Physical Sciences*. McGraw-Hill, New York, 1969. ISBN: 0-07-247227-8.
- [33] *Compute Objective Functions.* The MathWorks, Inc., 2017. <https://www.mathworks.com/help/gads/computing-objective-functions.html>.
- [34] *Maximizing an Objective.* The MathWorks, Inc., 2017. <https://www.mathworks.com/help/optim/ug/maximizing-an-objective.html>.
- [35] *Linear Constraints.* The MathWorks, Inc., 2017. <https://www.mathworks.com/help/optim/ug/linear-constraints.html#brhkghv-14>.
- [36] *Bound Constraints.* The MathWorks, Inc., 2017. <https://www.mathworks.com/help/optim/ug/bound-constraints.html>.
- [37] *Nonlinear Constraints.* The MathWorks, Inc., 2017. <https://www.mathworks.com/help/optim/ug/nonlinear-constraints.html>.
- [38] A. C. Marta. *Multidisciplinary Design Optimization of Aircrafts.* Instituto Superior Técnico, Lisbon, Feb. 2015. <https://fenix.ist.utl.pt/homepage/ist31052/optimizacao-multidisciplinar-de-aeronaves>.
- [39] NEOS. Types of Optimization Problems, 2017. <https://neos-guide.org/optimization-tree> accessed on Sep 2017.
- [40] *Choosing the Algorithm.* The MathWorks, Inc., 2017. <https://www.mathworks.com/help/optim/ug/choosing-the-algorithm.html>.
- [41] P. Ngatchou, A. Zarei, and M. A. El-Sharkawi. Pareto Multi Objective Optimization. *Intelligent Systems Application to Power Systems*, pages 84–89, 2005. doi: 10.1109/ISAP.2005.1599245.
- [42] T. C. Corke. *Design of Aircraft*. Pearson Education, Inc., University of Notre Dame, 2003. ISBN: 0-13-089234-3.
- [43] A. C. Marta and P. V. Gamboa. Long Endurance Electric UAV for Civilian Surveillance Missions. *29th Congress of International Council of the Aeronautical Sciences*, Sept. 2014. https://www.researchgate.net/publication/272162620_Long_Endurance_Electric_UAV_for_Civilian_Surveillance_Missions.

Appendix A

Input Files and Results

As referred previously in this thesis, in this Appendix it is possible to visualize the propeller and motor input files for each measure and airfoil and the results obtained from the experimental tests and the validation.

A.1 Propeller Files

APC 13x8 Clark_Y										APC 13x8 NACA_4412															
2	! Nblades								2	! Nblades															
0.366	6.67	! CL0		CL_a		0.4455	6.76	! CL0		CL_a		-0.35	1.37	! CLmin		CLmax									
-0.48	1.324	! CLmin		CLmax		0.0172	0.038	0.0058	0.7926	! CD0		CD2u	CD2l	CLCDO	0.0174	0.012	0.023	0.5651	! CD0		CD2u	CD2l	CLCDO		
100000	-0.7	! REref		REexp		100000	-0.5	! REref		REexp		0.001	0.001	1.0	!	Rfac	Cfac	Bfac	0.025	0.0	0.0	!	Radd	Cadd	Badd
# r	chord	beta								# r	chord	beta													
0.0	11.50	90.00								0.0	11.50	90.00													
8.56	13.50	51.06								8.56	13.50	51.06													
17.12	17.80	44.16								17.12	17.80	44.16													
25.68	19.40	37.46								25.68	19.40	37.46													
34.24	20.40	35.07								34.24	20.40	35.07													
42.80	21.10	30.47								42.80	21.10	30.47													
51.36	21.20	28.14								51.36	21.20	28.14													
59.92	21.30	24.55								59.92	21.30	24.55													
68.48	21.05	23.22								68.48	21.05	23.22													
77.04	20.50	20.26								77.04	20.50	20.26													
85.60	19.75	19.22								85.60	19.75	19.22													
94.16	19.20	16.80								94.16	19.20	16.80													
102.72	18.25	16.06								102.72	18.25	16.06													
111.28	16.57	15.76								111.28	16.57	15.76													
119.84	14.50	15.40								119.84	14.50	15.40													
128.40	12.00	12.02								128.40	12.00	12.02													
136.96	7.95	9.41								136.96	7.95	9.41													
145.00	1.10	0.00								145.00	1.10	0.00													

(a) APC 13"×8" Clark-Y airfoil

(b) APC 13"×8" NACA 4412 airfoil

Figure A.1: Input files for APC 13"×8" propellers

APC 16x8 Clark_Y

```

2           ! Nblades
0.366 6.67 ! CL0      CL_a
-0.48 1.324 ! CLmin   CLmax
0.0172 0.038 0.0058 0.7926 ! CDO     CD2u   CD21    CLCD0
100000 -0.7          ! REref   REexp
0.001 0.001 1.0 ! Rfac   Cfac   Bfac
0.028 0.0 0.0 ! Radd   Cadd   Badd
# r      chord  beta
0.0    11.55  90.00
11.40  17.20  48.84
22.80  21.60  41.16
34.20  24.05  33.15
45.60  25.30  30.79
57.00  26.20  27.19
68.40  26.45  23.86
79.80  26.60  19.82
91.20  26.35  17.79
102.60 25.60  17.62
114.00 24.40  15.82
125.40 23.05  15.73
136.80 21.35  15.35
148.20 18.85  12.87
159.60 15.22  9.15
171.00 11.32  7.87
183.00 1.12   0.00

```

(a) APC 16"×8" Clark-Y airfoil

APC 16x8 NACA_4412

```

2           ! Nblades
0.4455 6.76 ! CL0      CL_a
-0.35 1.37 ! CLmin   CLmax
0.0174 0.012 0.023 0.5651 ! CDO     CD2u   CD21    CLCD0
100000 -0.5          ! REref   REexp
0.001 0.001 1.0 ! Rfac   Cfac   Bfac
0.028 0.0 0.0 ! Radd   Cadd   Badd
# r      chord  beta
0.0    11.55  90.00
11.40  17.20  48.84
22.80  21.60  41.16
34.20  24.05  33.15
45.60  25.30  30.79
57.00  26.20  27.19
68.40  26.45  23.86
79.80  26.60  19.82
91.20  26.35  17.79
102.60 25.60  17.62
114.00 24.40  15.82
125.40 23.05  15.73
136.80 21.35  15.35
148.20 18.85  12.87
159.60 15.22  9.15
171.00 11.32  7.87
183.00 1.12   0.00

```

(b) APC 16"×8" NACA 4412 airfoil

Figure A.2: Input files for APC 16"×8" propellers

APC 16x10 Clark_Y

```

2           ! Nblades
0.366 6.67 ! CL0      CL_a
-0.48 1.324 ! CLmin   CLmax
0.0172 0.038 0.0058 0.7926 ! CDO     CD2u   CD21    CLCD0
100000 -0.7          ! REref   REexp
0.001 0.001 1.0 ! Rfac   Cfac   Bfac
0.028 0.0 0.0 ! Radd   Cadd   Badd
# r      chord  beta
0.0    9.35   90.00
11.40  21.35  47.34
22.80  25.00  39.05
34.20  26.60  33.03
45.60  27.20  29.32
57.00  27.50  26.69
68.40  27.60  23.94
79.80  27.55  21.44
91.20  27.25  18.95
102.60 26.25  17.06
114.00 25.00  14.76
125.40 23.20  13.97
136.80 21.05  11.09
148.20 18.25  7.40
159.60 15.00  7.09
171.00 10.25  6.16
180.20 1.20   0.00

```

(a) APC 16"×10" Clark-Y airfoil

APC 16x10 NACA_4412

```

2           ! Nblades
0.4455 6.76 ! CL0      CL_a
-0.35 1.37 ! CLmin   CLmax
0.0174 0.012 0.023 0.5651 ! CDO     CD2u   CD21    CLCD0
100000 -0.5          ! REref   REexp
0.001 0.001 1.0 ! Rfac   Cfac   Bfac
0.028 0.0 0.0 ! Radd   Cadd   Badd
# r      chord  beta
0.0    9.35   90.00
11.40  21.35  47.34
22.80  25.00  39.05
34.20  26.60  33.03
45.60  27.20  29.32
57.00  27.50  26.69
68.40  27.60  23.94
79.80  27.55  21.44
91.20  27.25  18.95
102.60 26.25  17.06
114.00 25.00  14.76
125.40 23.20  13.97
136.80 21.05  11.09
148.20 18.25  7.40
159.60 15.00  7.09
171.00 10.25  6.16
180.20 1.20   0.00

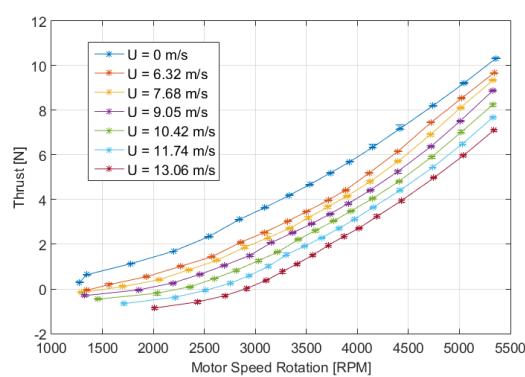
```

(b) APC 16"×10" NACA 4412 airfoil

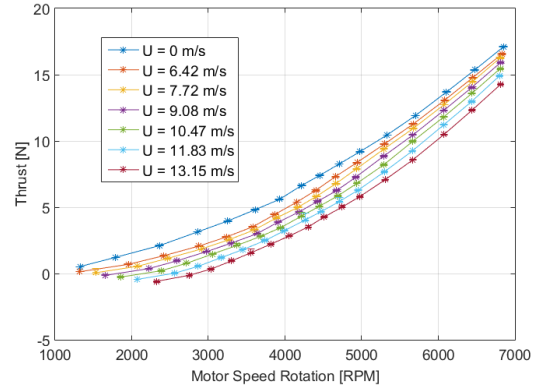
Figure A.3: Input files for APC 16"×10" propellers

A.2 Experimental Results

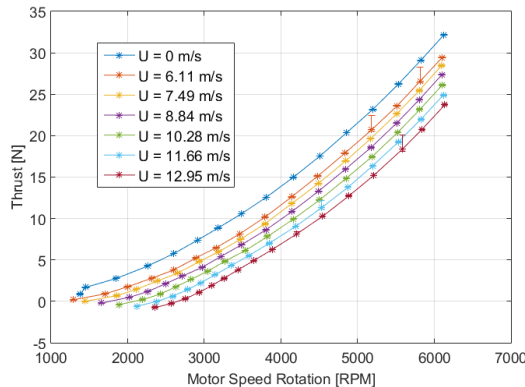
A.2.1 Thrust



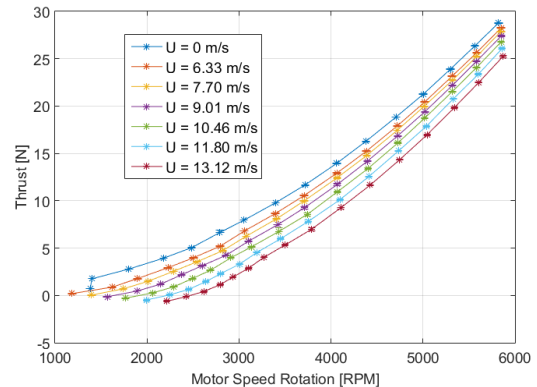
(a) OS-5020-490 + APC 13"×8" for 12.5 V



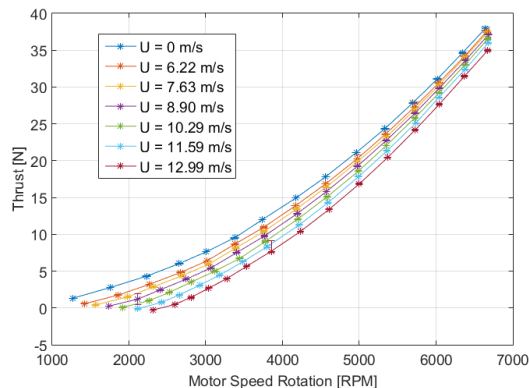
(b) OS-5020-490 + APC 13"×8" for 16.5 V



(c) OS-5020-490 + APC 16"×8" for 16.5 V



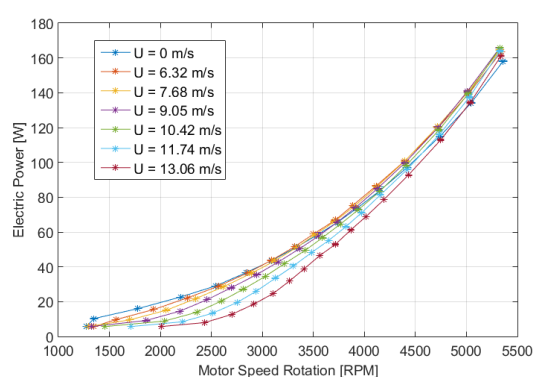
(d) OS-5020-490 + APC 16"×10" for 16.5 V



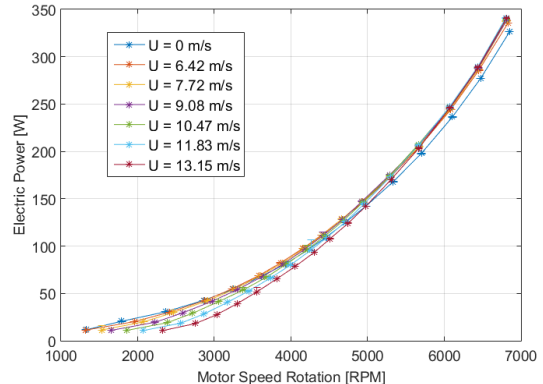
(e) OS-5020-490 + APC 16"×10" for 21.0 V

Figure A.4: Variation of thrust with airspeed and RPM for the different systems tested

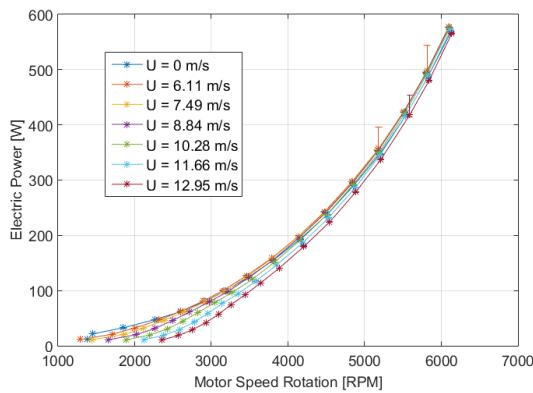
A.2.2 Electrical Power



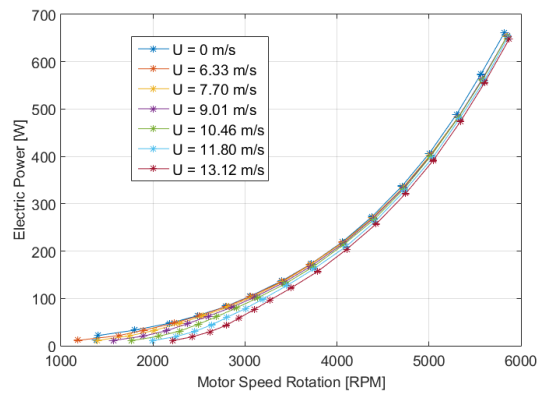
(a) OS-5020-490 + APC 13" x 8" for 12.5 V



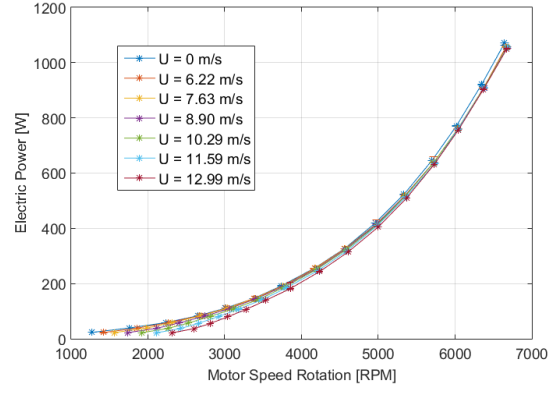
(b) OS-5020-490 + APC 13" x 8" for 16.5 V



(c) OS-5020-490 + APC 16" x 8" for 16.5 V



(d) OS-5020-490 + APC 16" x 10" for 16.5 V



(e) OS-5020-490 + APC 16" x 10" for 21.0 V

Figure A.5: Variation of electrical power with airspeed and RPM for the different systems tested

A.2.3 Thrust Coefficient

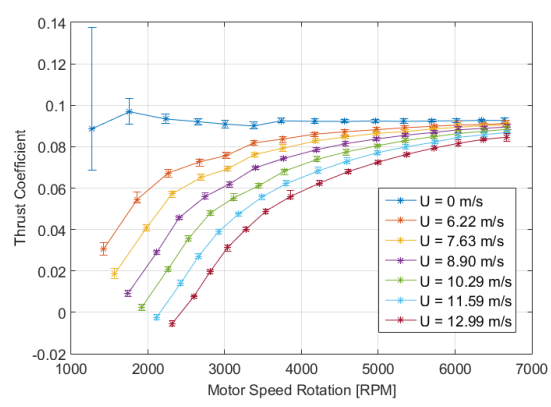
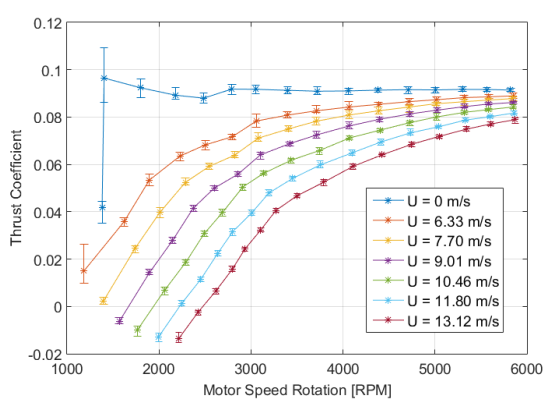
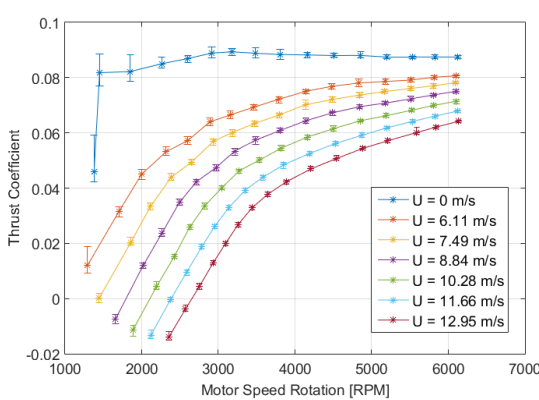
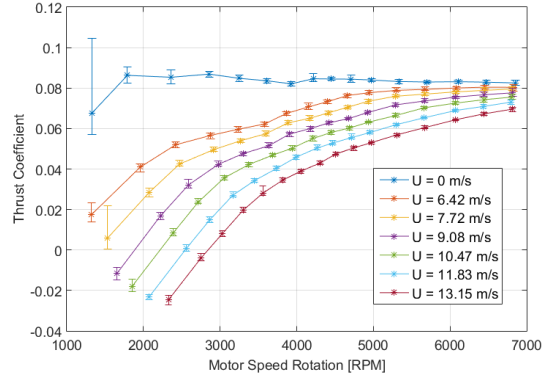
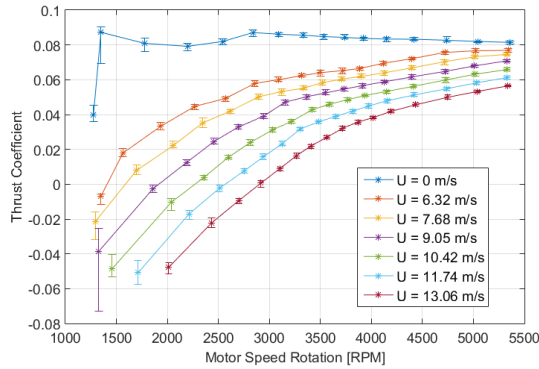


Figure A.6: Variation of thrust coefficient with airspeed and RPM for the different systems tested

A.2.4 Power Coefficient

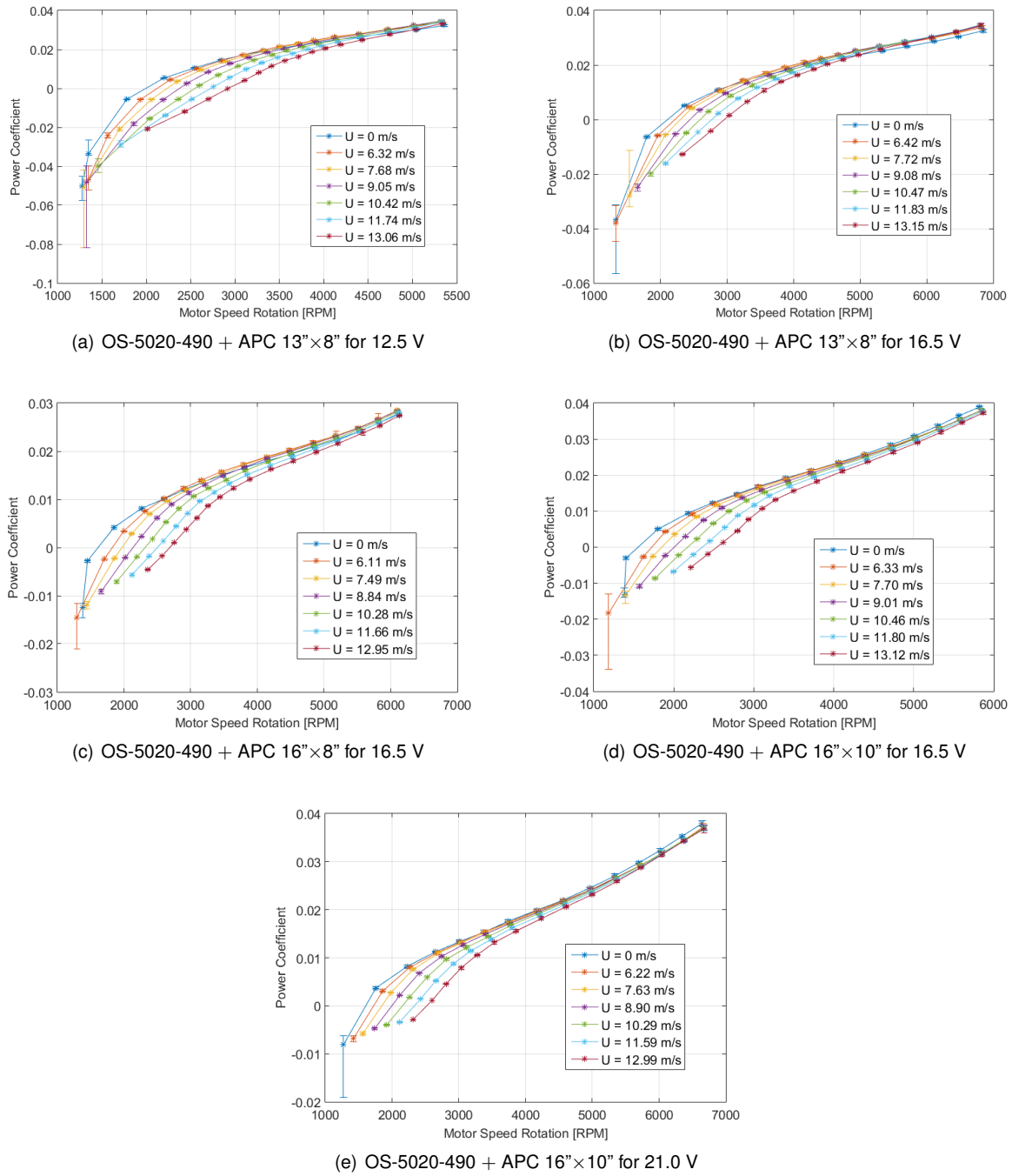
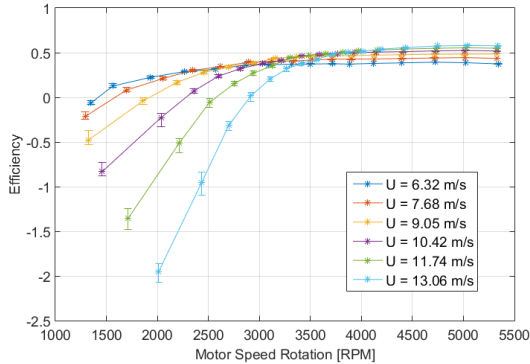
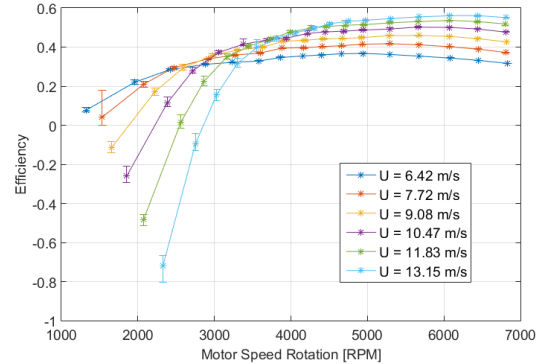


Figure A.7: Variation of power coefficient with airspeed and RPM for the different systems tested

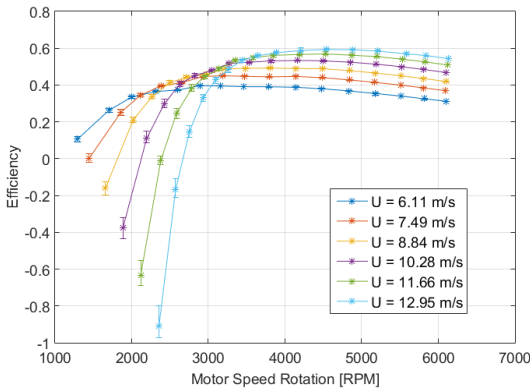
A.2.5 Efficiency



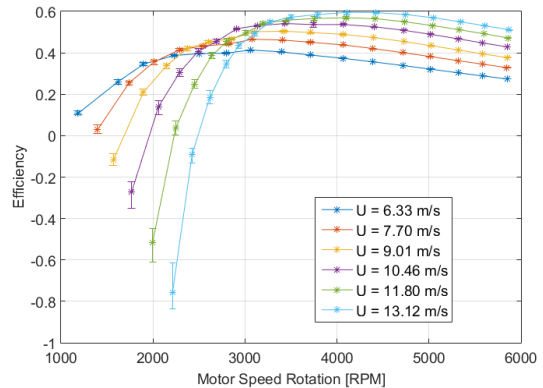
(a) OS-5020-490 + APC 13"×8" for 12.5 V



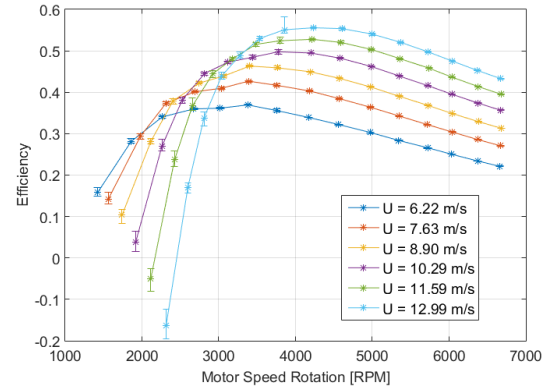
(b) OS-5020-490 + APC 13"×8" for 16.5 V



(c) OS-5020-490 + APC 16"×8" for 16.5 V



(d) OS-5020-490 + APC 16"×10" for 16.5 V

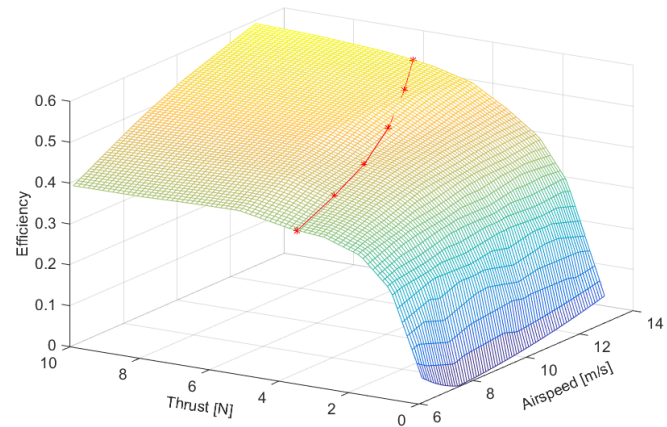


(e) OS-5020-490 + APC 16"×10" for 21.0 V

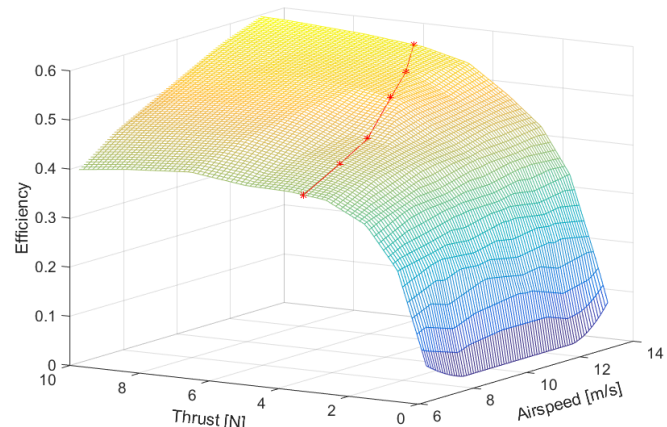
Figure A.8: Variation of efficiency with airspeed and RPM for the different systems tested

A.3 LEEUAV Case Study

A.3.1 Propeller Pitch



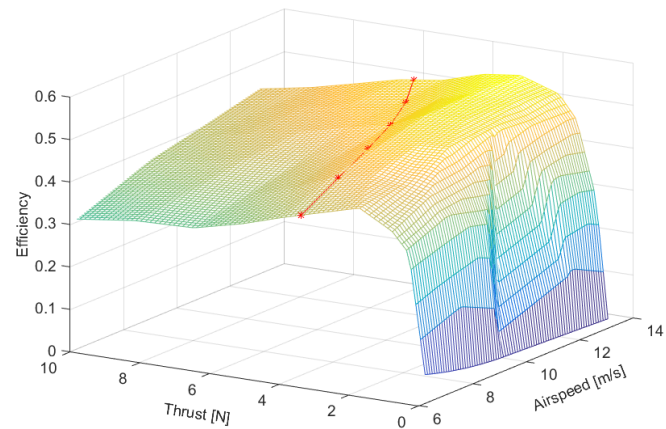
(a) OS-5020-490 + APC 16"×8" for 16.5 V



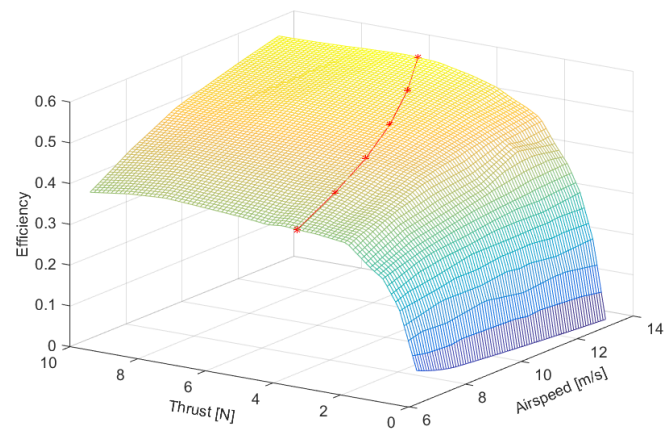
(b) OS-5020-490 + APC 16"×10" for 16.5 V

Figure A.9: Efficiency variation with propeller pitch

A.3.2 Electrical Motor



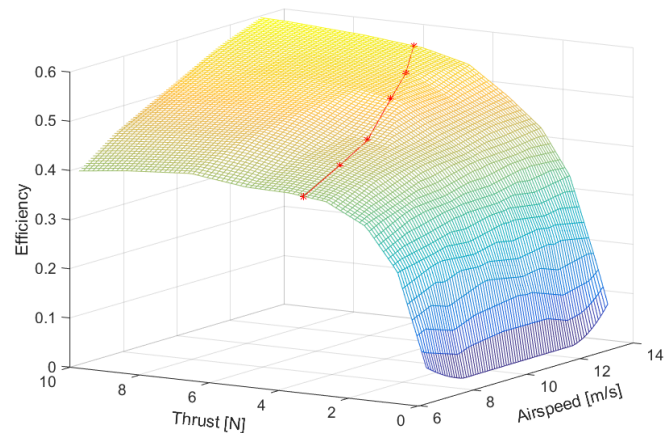
(a) OS-3810-1050 + APC 13"×8" for 12.5 V



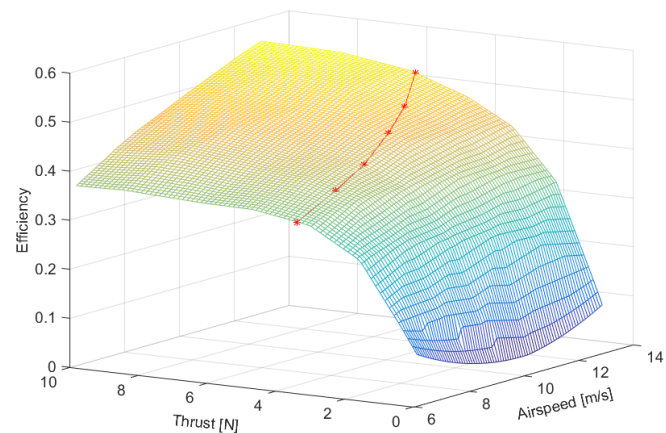
(b) OS-5020-490 + APC 13"×8" for 12.5 V

Figure A.10: Efficiency variation with electrical motor

A.3.3 Input Voltage



(a) OS-5020-490 + APC 16"×10" for 16.5 V



(b) OS-5020-490 + APC 16"×10" for 21.0 V

Figure A.11: Efficiency variation with input voltage

A.4 Validation

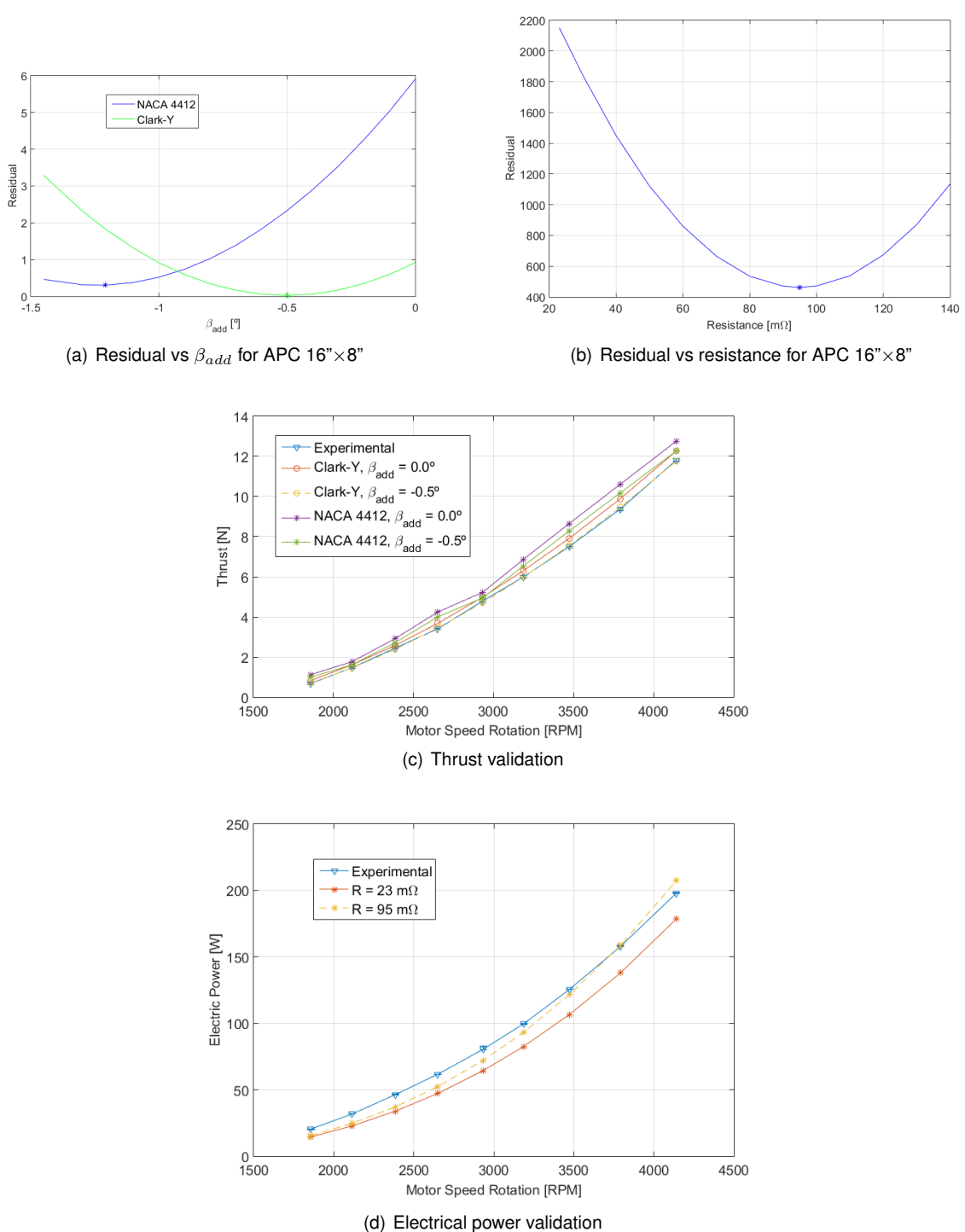


Figure A.12: Validation parameters for the system OS-5020-490 + 16"×8"

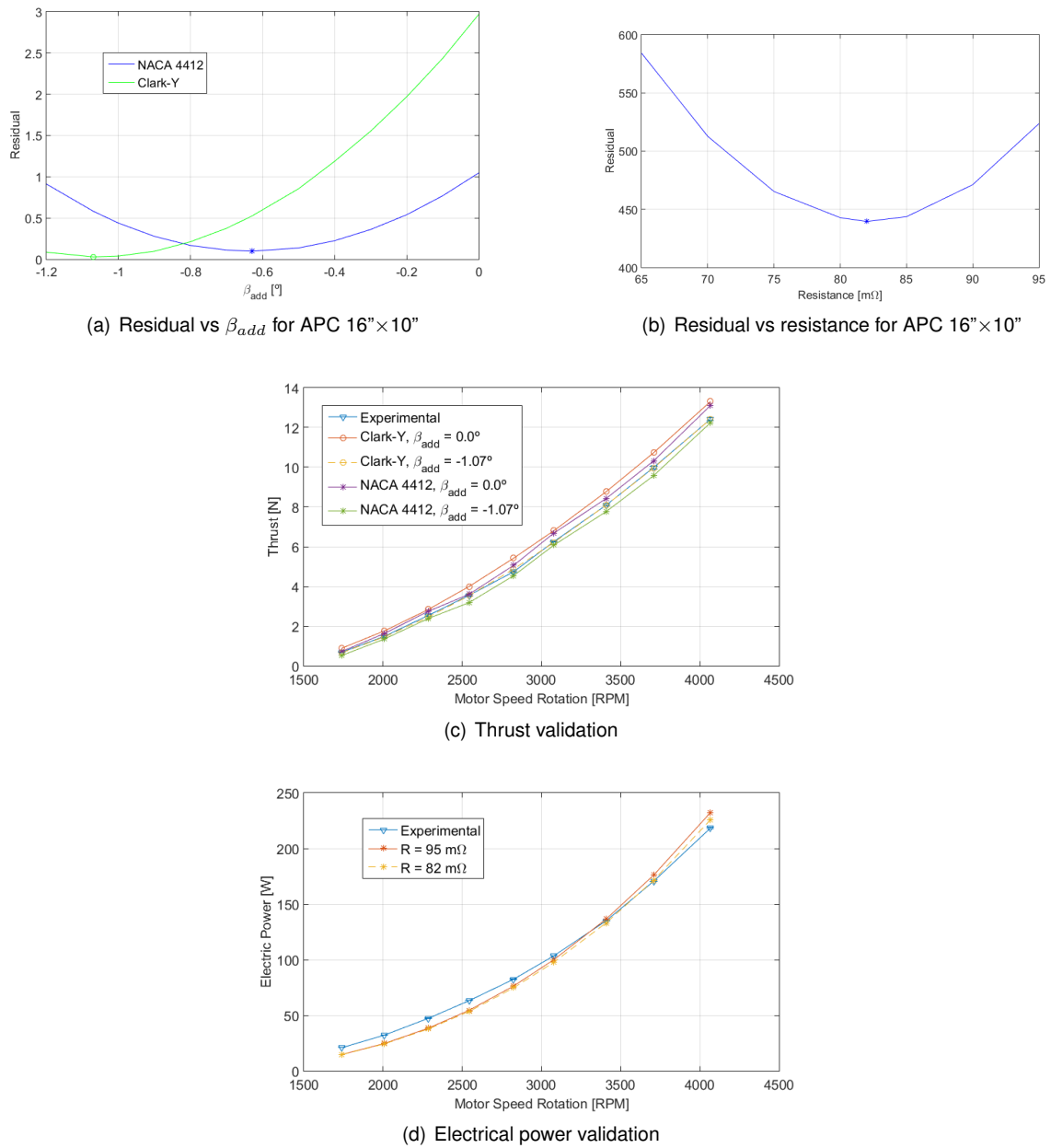


Figure A.13: Validation parameters for the system OS-5020-490 + 16"×10"

A.5 Validated System Files

APC 13x8 NACA_4412

```

2           ! Nblades

0.4455  6.76  ! CL0      CL_a
-0.35   1.37  ! CLmin   CLmax

0.0174  0.012  0.023  0.5651  ! CDO     CD2u  CD21    CLCD0
100000  -0.5          ! REref  REexp

0.001  0.001  1.0  ! Rfac  Cfac  Bfac
0.025  0.0      0.58 ! Radd  Cadd  Badd

# r      chord  beta
0.0      11.50  90.00
0.56     13.50  51.06
17.12    17.80  44.16
25.68    19.40  37.46
34.24    20.40  35.07
42.80    21.10  30.47
51.36    21.20  28.14
59.92    21.30  24.55
68.48    21.05  23.22
77.04    20.50  20.26
85.60    19.75  19.22
94.16    19.20  16.80
102.72   18.25  16.06
111.28   16.57  15.76
119.84   14.50  15.40
128.40   12.00  12.02
136.96   7.95   9.41
145.00   1.10   0.00

```

(a) APC 13"×8" NACA 4412 airfoil

OS-3810-1050 (12.5V)

```

1           ! motor type (brushless DC)

0.0759  ! Rmotor (Ohms)
1.100   ! Io      (Amps)
1050.0  ! Kv      (rpm/Volt)

```

(b) Motor OS – 3810 – 1050

Figure A.14: Validated files for the system OS-3810-1050 + 13"×8"

APC 16x8 Clark_Y

OS-5020-490

```

2           ! Nblades

0.366  6.67  ! CL0      CL_a
-0.48   1.324 ! CLmin   CLmax

0.0172  0.038  0.0058  0.7926  ! CDO     CD2u  CD21    CLCD0
100000  -0.5          ! REref  REexp

0.001  0.001  1.0  ! Rfac  Cfac  Bfac
0.028  0.0      -0.5 ! Radd  Cadd  Badd

# r      chord  beta
0.0      11.55  90.00
11.40    17.20  48.84
22.80    21.60  41.16
34.20    24.05  33.15
45.60    25.30  30.79
57.00    26.20  27.19
68.40    26.45  23.86
79.80    26.60  19.82
91.20    26.35  17.79
102.60   25.60  17.62
114.00   24.40  15.82
125.40   23.05  15.73
136.80   21.35  15.35
148.20   18.85  12.87
159.60   15.22  9.15
171.00   11.32  7.87
183.00   1.12   0.00

```

(a) APC 16"×8" Clark-Y airfoil

(b) Motor OS – 5020 – 490

Figure A.15: Validated files for the system OS-5020-490 + 16"×8"

OS-5020-490

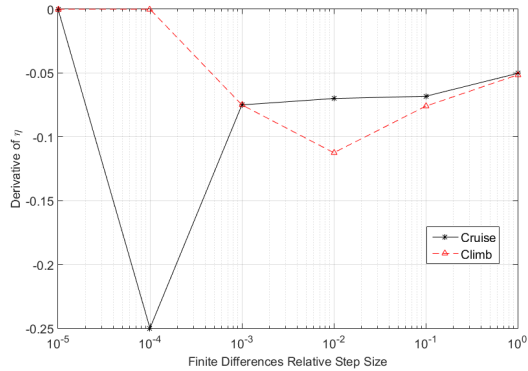
```
APC 16x10 Clark_Y  
2           ! Nblades  
0.366 6.67  ! CL0     CL_a  
-0.48 1.324 ! CLmin   CLmax  
0.0172 0.038 0.0058 0.7926 ! CD0    CD2u  CD21   CLCD0  
100000 -0.5          ! REref  REexp  
0.001 0.001 1.0 ! Rfac   Cfac   Bfac  
0.028 0.0  -1.07 ! Radd   Cadd   Badd  
  
# r      chord  beta  
0.0    9.35   90.00  
11.40  21.35  50.64  
22.80  25.00  42.35  
34.20  26.60  36.33  
45.60  27.20  32.62  
57.00  27.50  29.99  
68.40  27.60  27.24  
79.80  27.55  24.74  
91.20  27.25  22.25  
102.60 26.25  21.36  
114.00 25.00  19.06  
125.40 23.20  18.27  
136.80 21.05  15.56  
148.20 18.25  12.70  
159.60 15.00  10.09  
171.00 10.25  7.16  
180.20 1.20   0.00
```

(a) APC 16"×10" Clark-Y Airfoil airfoil

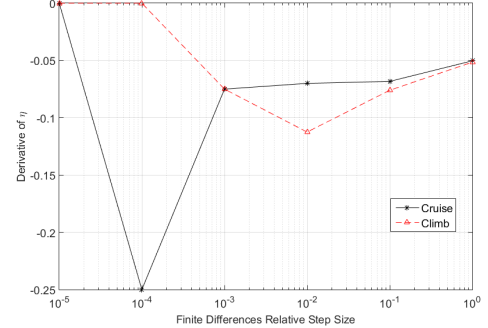
(b) Motor OS – 5020 – 490

Figure A.16: Validated files for the system OS-5020-490 + 16"×10"

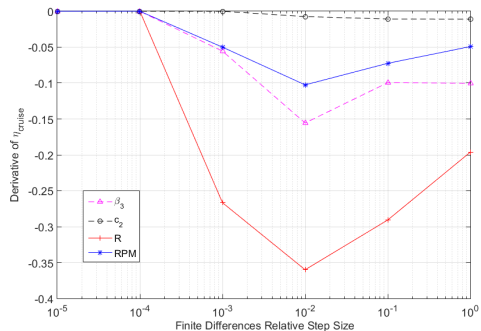
A.6 Optimization Files



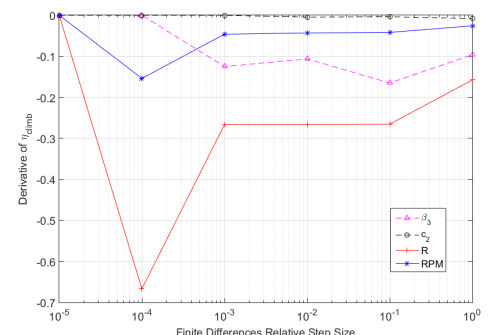
(a) Cruise and Climb - Unconstrained operation variables optimization



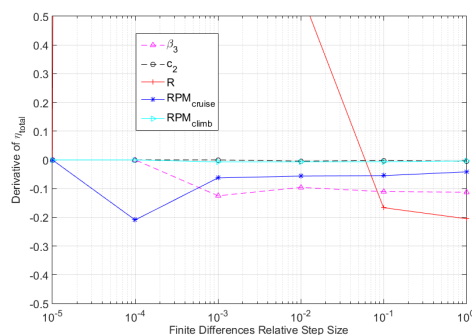
(b) Cruise and Climb - Thrust constrained operation variables optimization



(c) Cruise - Geometric variables optimization

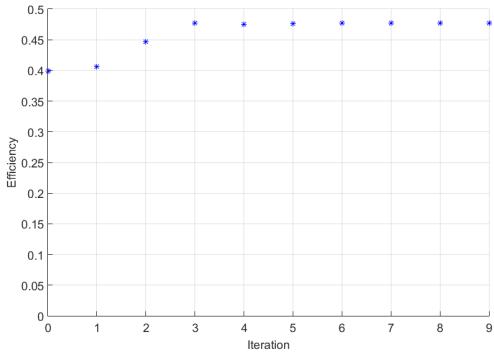


(d) Climb - Geometric variables optimization

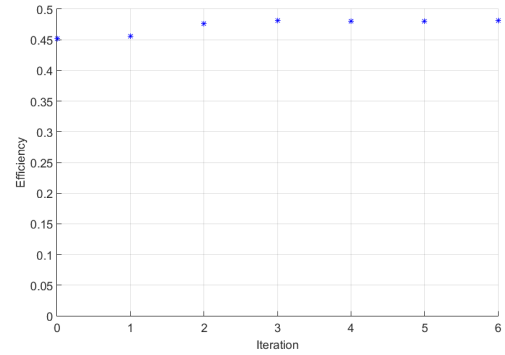


(e) Final geometric variables optimization

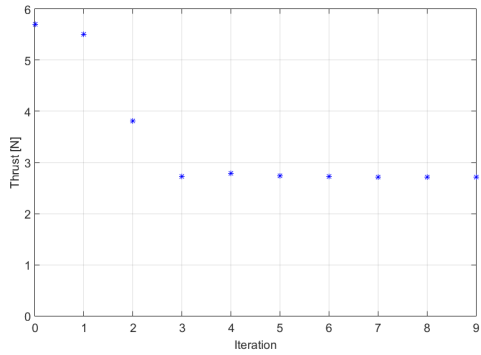
Figure A.17: First derivative variation in order to the respective design variables for different values of different step size



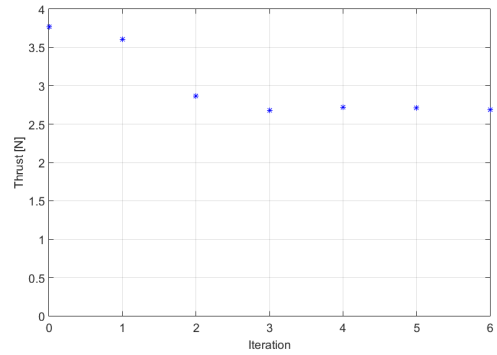
(a) Efficiency - Cruise



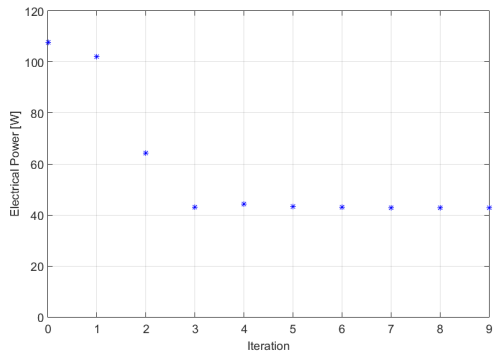
(b) Efficiency - Climb



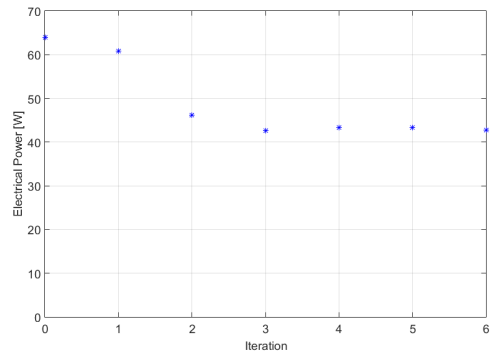
(c) Thrust - Cruise



(d) Thrust - Climb

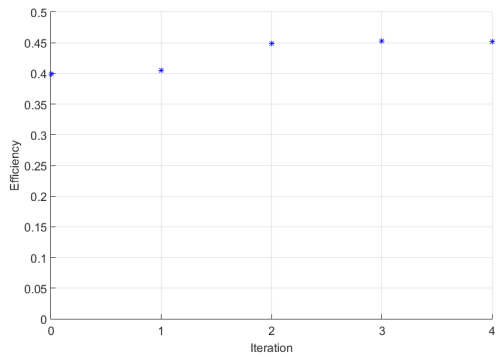


(e) Electrical Power - Cruise

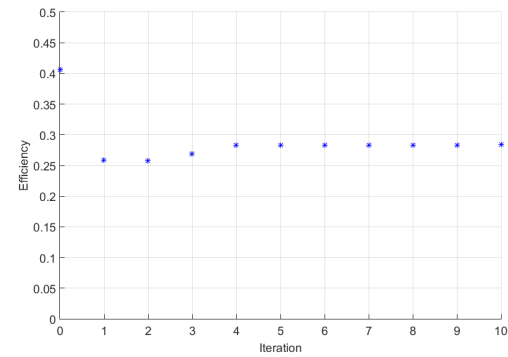


(f) Electrical Power - Climb

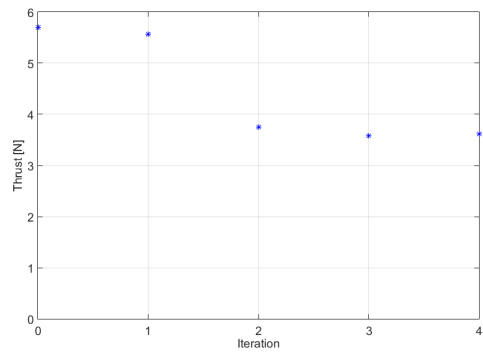
Figure A.18: Parameters evolution along the operation variables unconstrained optimization process, at each iteration



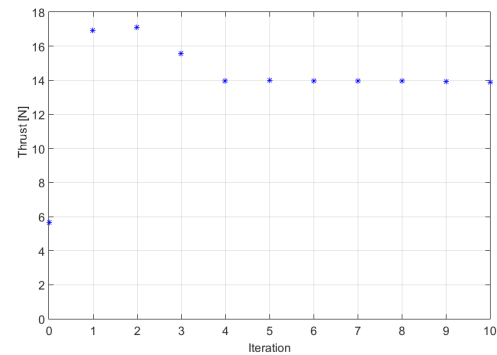
(a) Efficiency - Cruise



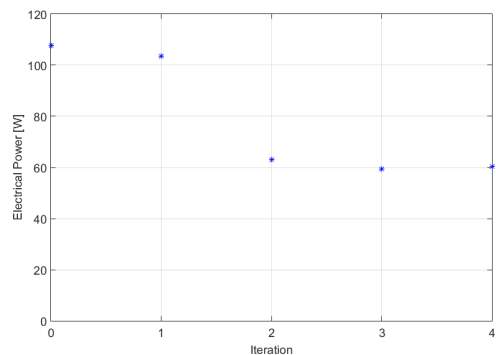
(b) Efficiency - Climb



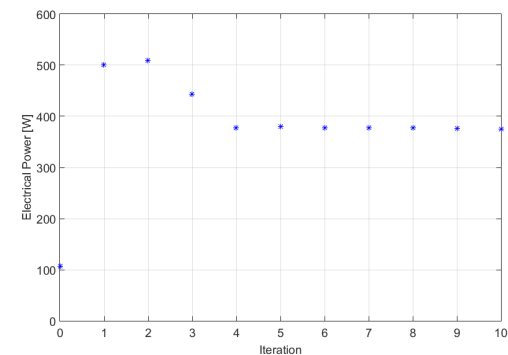
(c) Thrust - Cruise



(d) Thrust - Climb



(e) Electrical Power - Cruise



(f) Electrical Power - Climb

Figure A.19: Parameters evolution along the operation variables optimization process with constrained thrust, at each iteration

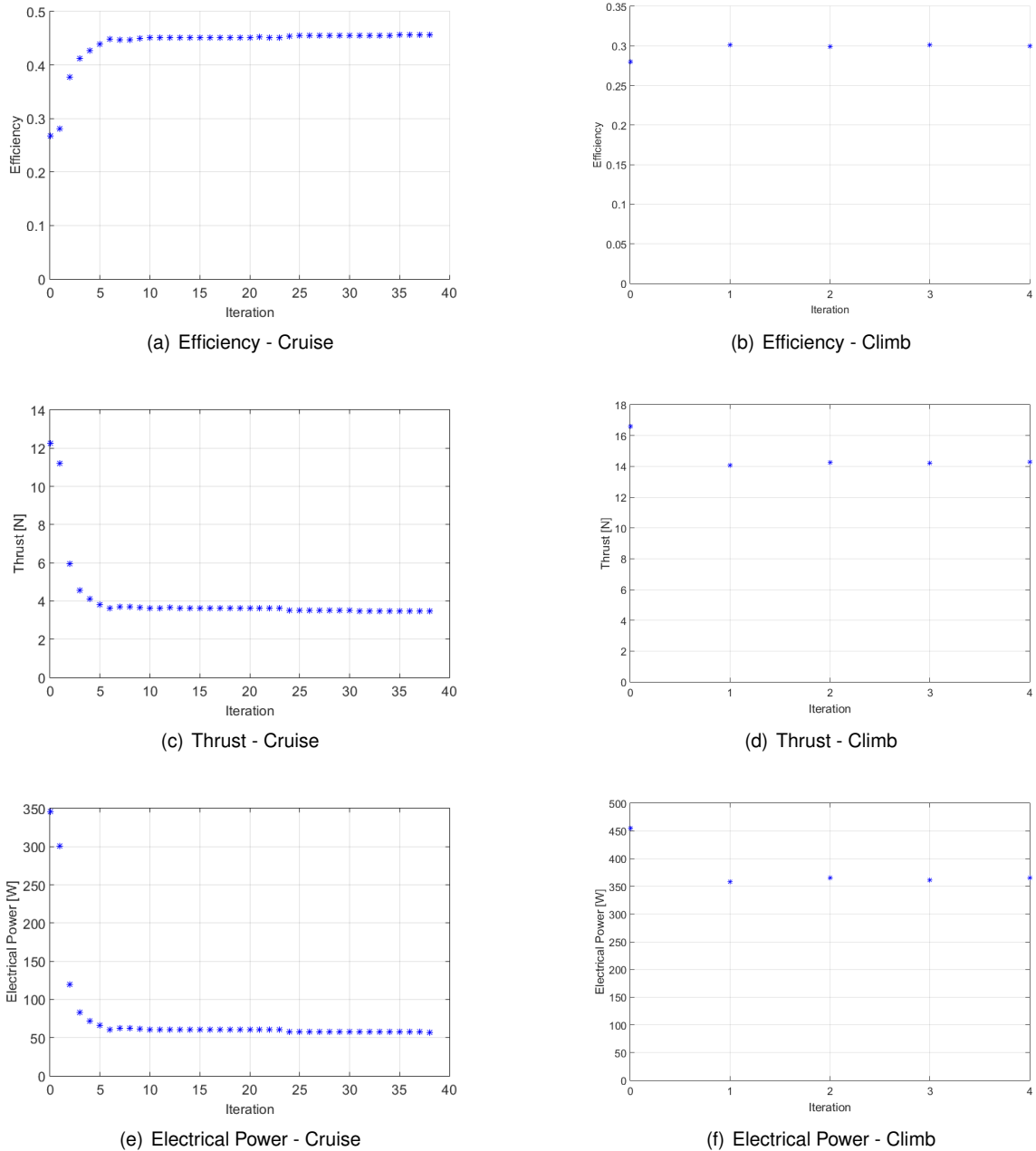


Figure A.20: Parameters evolution along the geometric variables optimization process with constrained thrust and electrical power, at each iteration

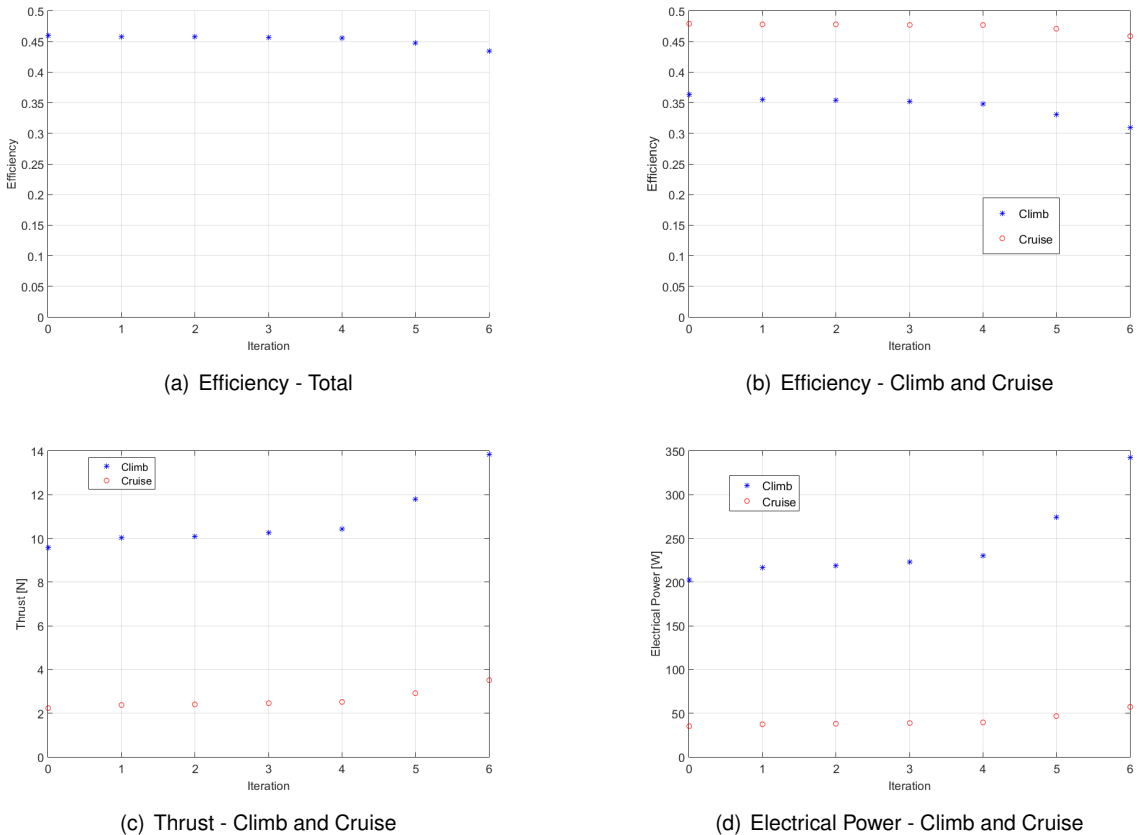


Figure A.21: Parameters evolution along the final geometric variables optimization process, at each iteration

